

Modeling and Design of Photoconductive and Superconductive Terahertz Photomixer Sources

by

Daryoosh Saeedkia

A thesis

presented to the University of Waterloo

in fulfilment of the

thesis requirement for the degree of

Doctor of Philosophy

in

Electrical and Computer Engineering

Waterloo, Ontario, Canada, 2005

© Daryoosh Saeedkia 2005

I hereby declare that I am the sole author of this thesis. This is a true copy of the thesis, including any required final revisions, as accepted by my examiners. I understand that my thesis may be made electronically available to the public.

Abstract

Terahertz technology is a fast growing field with variety of applications in biology and medicine, medical imaging, material spectroscopy and sensing, monitoring and spectroscopy in pharmaceutical industry, security, and high-data-rate short-range communications. Among different terahertz sources, photomixers are potentially compact, low power consuming, coherent, low-cost, and tunable continuous-wave sources. A terahertz photomixer is a heterodyne scheme, in which two laser beams with their frequency difference falling in the terahertz range mix in a nonlinear medium, such as a photoconductor or a superconductor, and generate a signal, whose frequency is equal to the frequency difference of the two lasers. The frequency of the generated terahertz signal can be tuned by tuning the central frequency of one of the lasers.

In this dissertation, the photomixing in superconductors and photoconductors is studied, and comprehensive analytical models for the interaction of two interfering laser beams with these materials are developed. Integrated photomixer-antenna elements as efficient terahertz sources are introduced and arrays of these elements as high power terahertz sources are designed. Also, an array of photoconductive photomixer-antenna elements with integrated excitation scheme is proposed.

In a photo-excited superconductor, the fundamental equations for the motion of the carriers inside the superconductor material are used in connection with the two-temperature model to find an analytic expression for the generated terahertz photocurrent inside the film. In a photo-excited photoconductor, the continuity equations for the electron and hole densities are solved in their general form along with the appropriate boundary conditions to find photocurrent distribution inside the photoconductor film. It is shown that in a continuous-wave (CW) terahertz photomixing scheme, the resulting photocurrent contains a dc component and a

terahertz traveling-wave component. The dependency of the amplitude and the phase of the generated photocurrent on the physical parameters of the photomixer, the parameters of the lasers, the applied dc bias, and the configuration of the device is explored in detail for a photoconductive photomixer made of low-temperature grown (LTG) GaAs and for a high-temperature superconductive photomixer made of $\text{YBa}_2\text{Cu}_3\text{O}_{7-\delta}$.

The developed models for the photoconductive and the superconductive terahertz photomixers are used to design new integrated photomixer-antenna devices. In these devices, the photomixing film simultaneously acts as an efficient radiator at the terahertz frequencies. Integrating the photomixing medium with the antenna not only eliminates any source to antenna coupling problem, but also makes the proposed device attractive for array configurations.

To increase the generated terahertz power, arrays of the photoconductive and the superconductive photomixer-antenna elements are proposed as CW terahertz sources. It is shown that a sub-milliwatt terahertz power is achievable from a typical superconductive photomixer-antenna array structure. The beam steering capability of the proposed devices is also investigated.

A photoconductive photomixer-antenna array with integrated excitation scheme is proposed, in which the laser beams are guided inside the substrate and excite the photomixer elements. In this way the laser power is only being consumed by the photomixer elements, and the photomixer-antenna elements can be integrated with other optical components on a single substrate. The whole structure is robust and less sensitive to vibration and other environmental parameters.

Acknowledgments

I would like to express my sincere thanks to Professor Safieddin Safavi-Naeini and Professor Raafat R. Mansour for their supervision and support during my Ph.D. program. During this journey, I learned many things that I would not be able to learn without their help and I am greatly thankful to them for giving me this opportunity.

I would like to thank to my thesis defense committee members, Professor Frank Hegmann from Department of Physics, University of Alberta, Edmonton, Canada, Professor James Martin from Department of Physics, University of Waterloo, Professor Sujeet Chaudhuri from Department of Electrical and Computer Engineering, University of Waterloo, and Professor Amir keyvan Khandani from Department of Electrical and Computer Engineering, University of Waterloo, for reading my thesis, for their invaluable comments and suggestions, and for accepting my thesis as a Ph.D. dissertation.

During these years, my darling wife Nadia was the one who was always there for me. She carried out all the responsibilities of our common life and gave me the chance to concentrate on my work. I could not have done this without her support. Words cannot express my appreciation for what she has done to me.

I would like to thank to Wendy Boles, Graduate Studies Coordinator, and Wendy Gauthier, former Graduate Office Admissions Secretary, at the Department of Electrical and Computer Engineering, for their help and guidance all these years.

It was a great opportunity for me to pursue my Ph.D. program at one of the best universities in Canada. With its warm and friendly atmosphere, the University of Waterloo is a great place for international students to continue their education. I will never forget all the good things that happened to me in this university during the last three years.

To my darling wife Nadia and my parents

Contents

1	Introduction	1
1.1	Motivation and Summary of Work	1
1.2	Organization of Thesis	4
2	Continuous-Wave Terahertz Sources: A Technology Overview	6
2.1	Electron Beam Sources	6
2.2	Optically Pumped Far-Infrared Gas Lasers	8
2.3	Solid-State Sources	8
2.4	Frequency Multipliers	10
2.5	Terahertz Semiconductor Lasers	11
2.6	Terahertz Parametric Oscillators	12
2.7	Terahertz Photomixers	15
3	Photomixing in Superconductors	21
3.1	Introduction	21
3.2	Modeling of Superconductive Photomixers	22

3.3	Simulation Results for an YBCO Photomixer	33
4	Photomixing in Photoconductors	49
4.1	Introduction	49
4.2	Modeling of Photoconductive Photomixers	51
4.3	Simulation Results for a Photomixer made of LTG-GaAs	62
5	Integrated Photomixer-Antenna Elements	76
5.1	Introduction	76
5.2	Longitudinal and Transversal Photomixer- Antenna Elements	77
5.2.1	Radiation from Photomixer-Antenna Elements	79
5.2.2	Simulation Results for an LTG-GaAs Photomixer-Antenna Element	81
6	Photomixer-Antenna Array	88
6.1	Photoconductive Photomixer-Antenna Array	88
6.1.1	Array Design Procedure	93
6.1.2	Simulation Results for an LTG-GaAs Photomixer-Antenna Array	95
6.2	Superconductive Photomixer-Antenna Array	106
6.2.1	Array Design Procedure	109
6.2.2	Simulation Results for an YBCO Photomixer-Antenna Array	110

7	Photomixer-Antenna Array with Integrated Excitation Scheme	118
7.1	Array Design I	119
7.2	Simulation Results	125
7.3	Array Design II	129
7.4	Simulation Results	132
8	Concluding Remarks	134
8.1	Summary and Contributions	134
8.2	Future Work	136
A	Calculation of the Carrier Densities N_0 and P_0	138

List of Figures

2.1	(a) Schematic of a terahertz parametric oscillator (TPO)(b) Injection-seeded terahertz parametric generator (IS-TPG).	13
2.2	(a) Top view of interdigitated-electrode vertically-driven photomixer coupled to a planar dipole antenna (b) Cross-sectional view of photomixer showing bottom-side coupling of THz radiation through a dielectric lens to free space.	16
2.3	Equivalent circuit diagram for the photomixer and antenna. Current drawn from the bias source is modulated at angular frequency ω by the photoconductor, with resistance $R(\omega, t)$. The capacitance C represents the effects of the charge accumulating at the electrodes. Power is dissipated in the antenna, $R_A(\omega)$, of which the component oscillating with angular frequency ω is coupled out as terahertz radiation.	17
2.4	(a) Velocity-match of laser interference fringes to the THz wave on the coplanar stripline is obtained by a tuning-angle between the two laser beams (b) Scanning electron microscope picture of a traveling-wave metal-semiconductor-metal (TW-MSM) structure with inner part of bow-tie antenna (c) A section of TW-MSM.	18

2.5	Output power of different continuous-wave terahertz sources versus frequency.	20
3.1	A typical superconductive photomixer scheme.	23
3.2	Critical optical power versus distance from the surface of the superconductor film at different bath temperatures. The critical temperature is $T_c = 87$ K.	35
3.3	Amplitude of the time-varying components of the electron and phonon temperatures. The dc current bias is 23.8 mA.	38
3.4	Amplitude of the time-varying component of the electron temperature versus bath temperature at different beat frequencies.	39
3.5	Drift and diffusion components of photocurrent given at the right hand side of Eq. (3.41) for two different bath temperatures. The critical temperature is $T_c = 87$ K.	40
3.6	Total photocurrent at the surface of the YBCO film versus beat frequency for $\theta = 10^\circ$ and at different bath temperatures. The critical temperature is $T_c = 87$ K.	41
3.7	Total photocurrent at the surface of the YBCO film versus beat frequency for $\theta = 0$ and at different bath temperatures. The critical temperature is $T_c = 87$ K.	42
3.8	Total photocurrent at the surface of the YBCO film versus bath temperature for $\theta = 10^\circ$ and at different beat frequencies.	43
3.9	Total photocurrent along the thickness of the YBCO film at $T_0 = 77$ K.	45
3.10	Total photocurrent along the thickness of the YBCO film at $T_0 = 82$ K.	46

3.11	Phase of photocurrent versus angle between the two laser beams. . .	47
3.12	Generated terahertz power inside the YBCO film versus total incident optical power at two different bath temperatures. The applied dc bias is 23.8 mA	48
4.1	A typical photoconductive photomixer scheme.	52
4.2	Electron lifetime versus applied electric field in LTG-GaAs. The low-field electron lifetime is $\tau_{n0} = 0.1$ ps.	64
4.3	Amplitude of electron density inside the LTG-GaAs film versus electron lifetime at different beat frequencies. The total applied optical power density is $I_0 = 0.4$ mW/ μm^2	65
4.4	Amplitude of electron density inside the LTG-GaAs film versus applied electric field at different beat frequencies. The total applied optical power density is $I_0 = 0.4$ mW/ μm^2	67
4.5	Amplitude of electron density versus beat frequency for different electron lifetimes in an LTG-GaAs photomixer. The total applied optical power density is $I_0 = 0.4$ mW/ μm^2	68
4.6	Amplitude of terahertz equivalent surface photocurrent in LTG-GaAs photomixer versus applied electric field at different beat frequencies and for two different low-field electron lifetimes. The total applied optical power density is $I_0 = 0.4$ mW/ μm^2	69
4.7	Amplitude of dc photocurrent in LTG-GaAs photomixer versus applied electric field at different low-field electron lifetimes. The total applied optical power density is $I_0 = 0.4$ mW/ μm^2	71

4.8	Amplitude of terahertz equivalent surface photocurrent in LTG-GaAs photomixer versus beat frequency at different low-field electron lifetimes. The total applied optical power density is $I_0 = 0.4 \text{ mW}/\mu\text{m}^2$.	72
4.9	Amplitude of terahertz equivalent surface photocurrent versus thickness of the LTG-GaAs film for different absorption coefficients. . . .	74
4.10	Longitudinal component of grating vector, K_x , and phase of terahertz photocurrent, ϕ , versus angle between the two laser beams. . .	75
5.1	Longitudinal photoconductive photomixer scheme.	77
5.2	Transversal photoconductive photomixer scheme.	78
5.3	Amplitude of equivalent surface photocurrent in LTG-GaAs longitudinal and transversal photomixers. The total optical power density of the two lasers is $0.4 \text{ mW}/\mu\text{m}^2$. The applied dc bias to each element is $4 \text{ V}/\mu\text{m}$	82
5.4	Radiation power of LTG-GaAs longitudinal and transversal photomixers. The total power density of the two lasers is $0.4 \text{ mW}/\mu\text{m}^2$. For the longitudinal case, the length of the film is $l = 5.6 \mu\text{m}$, while the width of the film is $w = 50 \mu\text{m}$. For the transversal case, the length and the width of the film are $l = 50 \mu\text{m}$ and $w = 5.6 \mu\text{m}$, respectively. The thickness of the film for both cases is $d = 2 \mu\text{m}$. The thickness of the substrate is changed according to the beat frequency to have maximum radiation at each frequency. The applied dc bias to each element is $4 \text{ V}/\mu\text{m}$	84
5.5	Configuration factor, ξ , for longitudinal and transversal photomixer-antenna devices.	85

5.6	Radiation power of LTG-GaAs longitudinal photomixer designed for 2 THz beat frequency. The length of the film is $l = 5.6 \mu\text{m}$ and the width of the film is $w = 50 \mu\text{m}$. The thickness of the substrate is fixed at $h = 10.917 \mu\text{m}$ to have maximum radiation at 2 THz. The applied dc bias to each element is $4 \text{ V}/\mu\text{m}$	87
6.1	(a) Photoconductive photomixer-antenna array configuration (b) Optical excitation scheme.	89
6.2	Array arrangement in $(x - y)$ plane.	91
6.3	Total terahertz radiation power of an 1×31 photoconductive photomixer-antenna array made of LTG-GaAs versus beat frequency. The thickness of the substrate is fixed at $21.8 \mu\text{m}$ to have maximum radiation at 1 THz. The total optical power density of the two lasers is $0.12 \text{ mW}/\mu\text{m}^2$. The lengths of the array elements and their separation distances are calculated from Eqs. (6.17) to (6.19), and are around $7.46 \mu\text{m}$. The width of the array elements is $120 \mu\text{m}$. The elements are biased to a dc voltage of 7.5 V	96
6.4	Total terahertz radiation power of an 1×31 photoconductive photomixer-antenna array made of LTG-GaAs versus applied electric field at different beat frequencies. The thickness of the substrate is changed according to the beat frequency to have maximum radiation at each frequency. The total power density of the two lasers is $0.12 \text{ mW}/\mu\text{m}^2$	97

6.5	Total terahertz radiation power of an 1×31 photoconductive photomixer-antenna array made of LTG-GaAs versus beat frequency. The thickness of the substrate changes according to the beat frequency to have maximum radiation at each frequency. The total optical power density of the two lasers is $0.12 \text{ mW}/\mu\text{m}^2$	99
6.6	Radiation pattern at $\phi = 0$ plane for different number of array elements and at the beat frequency of 1 THz; (a) 1×31 array (FWHM= 6.59°), (b) 1×51 array (FWHM= 4°), (c) 1×71 array (FWHM= 2.88°), (d) 1×91 array (FWHM= 2.3°).	100
6.7	Radiation pattern at $\phi = 0$ and $\phi = \pi/2$ planes for an 1×31 array at the beat frequency of 1 THz and $\theta_1 = 3.02^\circ$	102
6.8	Terahertz radiation power versus angle between the two lasers at the beat frequency of 1 THz.	103
6.9	Terahertz radiation power versus number of array elements at the beat frequency of 1 THz and for a constant optical power density of $0.12 \text{ mW}/\mu\text{m}^2$	104
6.10	Terahertz radiation power versus total optical power density at the beat frequency of 1 THz.	105
6.11	Superconductive photomixer-antenna array configuration.	106
6.12	Lengths of the array elements and their separation distances.	112
6.13	Terahertz radiation power versus angle between the two lasers.	113

6.14	Terahertz radiation power versus beat frequency for an YBCO array with 61 elements designed to operate at 3 THz. The thickness of the substrate is $5.21 \mu\text{m}$. The thickness and the width of the array elements are 130 nm and $40 \mu\text{m}$, respectively. The bath temperature is $T_0 = 85 \text{ K}$. Each laser radiates 114 mW optical power. The applied dc bias is 23.8 mA.	115
6.15	Total terahertz radiation power for an YBCO array with 61 elements versus beat frequency at two bath temperatures. The critical temperature is $T_c = 87 \text{ K}$. The thickness of the substrate changes according to the beat frequency to have maximum radiation at each frequency. The applied dc bias is 23.8 mA.	116
6.16	Radiation pattern of the array at $\phi = 0$ plane for different angles between the two lasers.	117
7.1	(a) A photomixer-antenna array with integrated excitation scheme. The laser beams are guided inside the core layer made of $\text{Al}_{0.1}\text{Ga}_{0.9}\text{As}$ with refractive index of $n_f = 3.55$ and excite the photomixer-antenna elements made of LTG-GaAs. (b) Electric field distribution around i -th element.	119

7.2	Terahertz radiation power versus beat frequency for different values of the thickness of the photomixer-antenna elements. The number of array elements is 19. The thickness of the core layer is $h_f = 0.573 \mu\text{m}$. The thickness of the substrate at the frequency of 1 THz is , $h_s = 22.4 \mu\text{m}$. The length of the array elements at the frequency of 1 THz is 55.6 nm. The width of the array elements is 100 μm . The dc bias voltage over each element is 0.139 V. The optical power coupled to the waveguide from each of the lasers is 100 mW.	127
7.3	Absorbed optical power in each element.	128
7.4	A photomixer-antenna array with integrated excitation scheme: two laser beams are lunched from one side of the optical waveguide. . .	129
7.5	Power flow diagram along the array structure.	132
7.6	Terahertz radiation power versus beat frequency for an array with 5 elements. The thickness of the core layer is $h_f = 0.573 \mu\text{m}$. The thickness of the substrate at the frequency of 1 THz is , $h_s = 22.4 \mu\text{m}$. The optical power of each laser is 100 mW. The lengths of the array elements are 220 nm, 282 nm, 395 nm, 663 nm, and 2.814 μm . The thickness and the width of the array elements are 0.573 μm and 200 μm , respectively. The absorbed optical in each element is 39.5 mW. The applied electric field over each element is 2.5 V/ μm	133

List of Tables

2.1	Power and frequency range of some two-terminal solid-state devices	9
2.2	Performance of planar Schottky diode multipliers	10
2.3	Characteristics of state-of-the-art continuous-wave quantum cascade lasers	12
2.4	Characteristics of state-of-the-art terahertz parametric oscillators .	14
3.1	Physical parameters of a photomixer made of $\text{YBa}_2\text{Cu}_3\text{O}_{7-\delta}$	34
4.1	Physical parameters of a photomixer made of LTG-GaAs	63

Chapter 1

Introduction

1.1 Motivation and Summary of Work

The terahertz spectrum, or far-infrared, refers to the frequency range from 100 GHz up to a few 10 THz. Terahertz technology is a fast growing field with its variety of new applications, including biology and medicine [1]- [6], imaging [7]- [9], material spectroscopy and sensing [10]- [16], monitoring and spectroscopy in pharmaceutical industry [17], [18], security [19]- [22], and high-data-rate communications [23]- [26]. Many chemical and biological matters have their own signatures in the terahertz spectrum, which makes it possible to identify and analyze them based on the way that they interact with terahertz waves.

Unlike X-rays, terahertz radiation is non-ionizing and can be safely used in medical imaging systems [27], [28]. Terahertz medical imaging presents unique solutions for a variety of health related problems such as tissue identification through its water content [29], disease diagnostics such as skin and liver cancer detection [30]- [33], and identification of dental caries [34], [35].

Terahertz waves can penetrate many non-metallic enclosures and can be used for screening and detecting hidden objects such as weapons containing a small amount of metal, ceramic weapons, explosive materials, and chemical and biological threats [19]- [21].

By increasing the number of users and services in wireless communication industry, moving to higher carrier frequencies to have more bandwidth for communication and data transferral is inevitable. Although the high atmospheric attenuation at terahertz frequencies makes it difficult to have a long-range mobile communication, however a high-bandwidth, short-range, and line of sight wireless link is completely realizable. The atmospheric attenuation is an advantage to reduce the coverage range of the signal in military applications to avoid communication being overheard, or in frequency re-use applications to avoid signal interfering.

Among different continuous-wave terahertz sources, photomixers are one of the most promising ones as potentially compact, low power consuming, low-cost, coherent, and tunable terahertz sources [36]- [65]. A terahertz photomixer is a heterodyne scheme, in which outputs of two single-mode lasers or output modes of a dual-mode laser with their frequency difference falling in the terahertz range mix in a nonlinear medium, such as a photoconductor or a superconductor, and generate a signal, whose frequency is equal to the frequency difference of the two lasers or two modes of the dual-mode laser. The frequency of the generated terahertz signal can be tuned by tuning the central frequency of the lasers. In fact, photomixers take advantage of both microwave and photonic techniques to generate signals in the terahertz frequency range.

Narrow spectral bandwidth and frequency control of the photomixers make them suitable for the applications such as biological and material spectroscopy [66]- [69], medical imaging [70], [71], and security [72], which need a tunable source over the

terahertz spectrum. Photomixers also can be used as local oscillators in heterodyne receivers for radio astronomy and communication applications [53].

The main drawback of terahertz photomixers is their low output terahertz power coming from their low optical-to-electrical conversion efficiency [73]. Much research has been conducted to increase the available power from these sources [74]- [78].

As a fundamental research work on the terahertz photomixers, we have developed analytical models for the interaction between laser beams and photoconductors and superconductors in typical photomixing schemes [79], [80].

Based on these models, we have proposed integrated photomixer-antenna elements made of low-temperature-grown (LTG) GaAs or $\text{YBa}_2\text{Cu}_3\text{O}_{7-\delta}$ high-temperature superconductor [81], [82]. Unlike conventional photomixers, in which a generated terahertz signal in an active region is coupled to an antenna for radiation, in a photomixer-antenna element the generated terahertz signal inside the photomixing film radiates simultaneously by designing the film as an efficient radiator. Using a photomixing medium as an antenna element not only eliminates any source-to-antenna coupling problem, but also distributes the optical power over a bigger area and hence increases optical power handling capability of the device.

We have designed arrays of the photomixer-antenna elements that generate more terahertz power and have beam-steering capability [83]- [85]. We have also proposed an array structure with an integrated optical excitation scheme. In this structure the photomixer elements are located above a dielectric substrate, which at the same time is a waveguide for the exciting laser beams. The laser beams excite the photomixer elements while they travel along the waveguide. In this way the laser power is only being consumed by photomixer elements, and hence the efficiency of the source increases.

1.2 Organization of Thesis

Chapter 2 reviews the state-of-the-art technologies of continuous-wave terahertz sources. Different CW terahertz source technologies are compared against each other from their maximum available terahertz power point of view.

Photomixing in superconductors is discussed in Chapter 3. For a photo-excited superconductor film the fundamental equations for the carriers motion inside the superconductor material have been used in connection with the two-temperature model to find an analytic expression for the generated terahertz photocurrent inside the film. The dependency of the resulting photocurrent on the material and laser parameters, temperature, and photomixer configuration for a photomixer made of $\text{YBa}_2\text{Cu}_3\text{O}_{7-\delta}$ high-temperature superconductor is studied.

Photomixing in photoconductors is discussed in Chapter 4. For a dc biased photoconductor excited by two laser beams the continuity equations for the electron and hole densities are solved in their general form along with the appropriate boundary conditions to find generated terahertz photocurrent distribution. The dependency of the photocurrent on the applied bias, parameters of the lasers, and photomixer configuration is explored for photomixers made of low-temperature-grown GaAs.

In Chapter 5, the integrated photomixer-antenna element is introduced. In this element the generated terahertz photocurrent radiates simultaneously by designing the photomixing film as an efficient radiator. The radiation characteristics for a photoconductive photomixer-antenna element over a grounded dielectric substrate are studied.

In Chapter 6, photoconductive and superconductive photomixer-antenna arrays are introduced. In these configurations, arrays of the photomixer-antenna elements are designed properly to radiate maximum power. The beam steering capability of

these configurations are also investigated.

The photoconductive photomixer-antenna array with integrated optical excitation scheme is introduced in Chapter 7. In this structure, the laser beams are guided inside the substrate and excite the photomixer elements while they travel along the length of the waveguide. Two different array structures are designed, for which the design procedures and the radiation characteristics are discussed in detail.

Chapter 8 contains some concluding remarks and provides suggestions for future works based on what is done in this dissertation.

Chapter 2

Continuous-Wave Terahertz Sources: A Technology Overview

Continuous-wave terahertz sources can be divided into seven categories, including electron beam sources, optically pumped far-infrared gas lasers, solid-state sources, frequency multipliers, terahertz semiconductor lasers, terahertz parametric oscillators, and photomixers. In the following, we review the existing technologies for these sources.

2.1 Electron Beam Sources

Gyrotrons [86], free electron lasers (FEL) [87], [88], and backward wave oscillators (BWO) [89] are electron beam sources that generate relatively high power signals at the terahertz frequency range. All of these devices work based on the interaction of a high-energy electron beam with a strong magnetic field inside resonant cavities or waveguides. Due to this interaction, energy transfer occurs from the electron

beam to an electromagnetic wave.

In gyrotrons cavities and waveguides are operated in high-order modes to increase the cross-sectional dimensions at high-frequency operations. Gyrotrons with 100 KW power operating in CW regime at 100 GHz [90] and with 1 MW power at 140 GHz [91] have been successfully developed. It has been shown that a gyrotron with 2 MW power at 170 GHz is feasible [92]. Free electron lasers are basically gyrotrons with very high operating frequencies obtained by deriving the electron beam with a high energy electron accelerator, and employing an optical cavity [93]. They also have greater tunability compared with gyrotrons. FELs are capable of operation over virtually the entire electromagnetic spectrum. They have been built at wavelengths from microwaves through the ultraviolet [94]- [97] and can be extended to X-rays [98]. A free electron laser at the University of California, Santa Barbara works at far-infrared region and generates 1 KW quasi-continuous-wave signal at 300 GHz.

In BWOs the phase and group velocity of the electromagnetic wave have opposite directions. BWOs are tunable sources with the possibility to tune their frequency electrically over a bandwidth of more than 50% and can generate up to 50 mW of power at 300 GHz going down to a few mW at 1 THz [99]. The commercially available systems provided by a Russian company (ISTOK) cover frequency range from 177 GHz to 1100 GHz with 1-10 mW output power. Complete systems are heavy and large and need high bias voltage and water cooling system [100], although they are much more smaller than FELs and gyrotrons. Microfabrication techniques are promising to reduce the size of these devices to make them suitable for terahertz applications [101].

Electron beam devices are bulky and need extremely high fields as well as high current densities, which are main disadvantages of these devices.

2.2 Optically Pumped Far-Infrared Gas Lasers

These terahertz sources consist a CO₂ pump laser injected into a cavity filled with a gas that lases to produce the terahertz signals [102], [103]. The lasing frequency is fixed dictated by the filling gas. Tunable sources have been developed based on mixing a tunable microwave source with these gas lasers [104], [105]. Power levels of 1-20 mW are common for 20-100 W laser pump power depending on the chosen line, with one of the strongest being that of methanol at 2522.78 GHz. A miniaturized gas laser has been reported with $75 \times 30 \times 10$ cm dimensions and 20 kg weight, which generates 30 mW power at 2.5 THz [106].

2.3 Solid-State Sources

Solid-state sources can be divided to two-terminal and three-terminal devices [107]-[109]. Two-terminal devices include resonant tunneling diodes (RTDs) [110], Gunn or transferred electron devices (TEDs) [111]- [113], and transit time devices such as impact avalanche transit time (IMPATT) diodes and tunnel injection transit time (TUNNETT) diodes. All of these devices exhibit a negative differential resistance property, although with different mechanisms.

The oscillation frequency of 578 GHz with GaInAs/AlAs RTD with 0.2 μ W output power [114] and 712 GHz with InAs/AlSb RTD with 0.3 μ W output power [115] have been obtained, which the latter is the highest fundamental frequency achieved so far from a solid-state source. Recently a carbon nanotube RTD device has been proposed as a CW terahertz source, which predicts 2.5 μ W terahertz power at 16 THz [116]. The state-of-the-art Gunn devices generate 0.2 to 5 μ W power at 400-560 GHz frequency range [117]. Presently, the maximum operation frequency for a

Table 2.1: Power and frequency range of some two-terminal solid-state devices

Device	Power	Frequency
RTD (InAs/AlSb) [115]	0.3 μ W	712 GHz
RTD (InGaAs/AlAs) [114], [118]	0.2 μ W	578 GHz
	50 μ W	205 GHz
	200 μ W	100 GHz
Gunn (InP) [108], [111], [117], [119]	5 μ W	416 GHz
	2 mW	315 GHz
	25 mW	162 GHz
	80 mW	152 GHz
	130 mW	132 GHz
IMPATT (Si) [120], [121]	0.2 mW	361 GHz
	7.5 mW	285 GHz
	300 mW	140 GHz
TUNNETT (GaAs) [119], [122]	0.14 mW	355 GHz
	4 mW	235 GHz
	9 mW	210 GHz
	10 mW	202 GHz

TUNNETT diode is 355 GHz with 140 μ W output power [122]. Table 2.1 shows the available two-terminal solid-state devices with their frequency and power ranges. Among three terminal solid-state devices, field effect transistors are suitable for high frequency operations because of their submicrometer gate lengths. A high electron mobility transistor (HEMT) with 30 nm gate length and 547 GHz cutoff frequency has been developed, which is the highest cutoff frequency yet reported for any transistor [123]. An InP HEMT monolithic millimeter-wave integrated circuit (MMIC) amplifier has been designed, which generates 20 mW power at 150 GHz [124]. Three terminal devices have advantage over two terminal devices

Table 2.2: Performance of planar Schottky diode multipliers

Multiplier chain	Temperature	Output power	Frequency
$\times 2(\times 3)^2$ [127]	120 K	$2.6 \mu\text{W}$	1.9 THz
$\times 2(\times 3)^2$ [128]	273 K	$3 \mu\text{W}$	1.74 THz
$\times 2(\times 3)^2$ [128]	120 K	$15 \mu\text{W}$	1.74 THz
$(\times 2)^4$ [129]	273 K	$15 \mu\text{W}$	1.5 THz
$(\times 2)^4$ [129]	120 K	$40 \mu\text{W}$	1.5 THz
$(\times 2)^2 \times 3$ [130]	273 K	$75 \mu\text{W}$	1.2 THz
$(\times 2)^2 \times 3$ [130]	80 K	$250 \mu\text{W}$	1.2 THz

in low-noise preamplifier applications. A 220 GHz HEMT low-noise amplifier has been developed with 10 dB gain over the bandwidth from 180 to 225 GHz [125].

2.4 Frequency Multipliers

In terahertz frequency multipliers, the frequency of a drive source is multiplied in a nonlinear device to generate higher order harmonic frequencies. Schottky varactor diodes are predominantly used as nonlinear devices in multipliers. Planar Schottky varactor diodes are commonly used in frequency multipliers, taking the advantage of GaAs substrateless technology to reduce substrate loss. The drive sources can be BWOs as well as solid-state sources such as Gunn and IMPATT oscillators, with relatively high output power in the range of 50 GHz to 150 GHz. Microwave frequency synthesizers in combination with high-gain power amplifiers fabricated by the monolithic microwave integrated circuit (MMIC) technology can provide a high power source above 100 GHz [126]. The most efficient terahertz frequency multipliers are realized by series chains of frequency doublers and frequency triplers [131]. The performances of the state-of-the-art planar Schottky diode multipliers

are given in Table 2.2. To date, the maximum achievable frequency from the frequency multipliers has been limited to 2 THz [132], [133].

2.5 Terahertz Semiconductor Lasers

In the terahertz semiconductor lasers, the inversion of population takes place between discrete energy levels, which generates terahertz stimulated emission. The first terahertz semiconductor laser working at 4 to 5 K was a single crystal of p-doped Ge placed between two mirrors [134]. The terahertz frequency can be tuned in the range of 1-4 THz.

The most promising terahertz semiconductor lasers are quantum cascade lasers [135]- [139]. The idea of quantum cascade laser was introduced in 1971 [135], while the first realization became possible in 1994 [136]. A quantum cascade laser is a unipolar laser, in which the conduction band or the valence band is divided to few intersubbands. The carrier transition occurs between these discrete energy levels within the same band. The discrete energy levels are created in a semiconductor heterostructure containing several coupled quantum wells. The first terahertz quantum cascade laser working at 50 K and generating 2 mW power at 4.4 THz contained 728 quantum wells, where each quantum well contained two 1-4 nm thick AlGaAs barriers and one 10-20 nm thick GaAs well [140]. A quantum cascade laser working in pulse regime with 3.5 W peak power at 33 THz operating at 300 K has been reported [141].

The first continuous-wave quantum cascade laser generated 25 μ W at 4.4 THz working at 52 K [142]. Given in Table 2.3 are the characteristics of the state-of-the-art continuous-wave quantum cascade lasers. As it can be seen from Table 2.3, the room temperature operation has not been achieved for frequencies below 10 THz.

Table 2.3: Characteristics of state-of-the-art continuous-wave quantum cascade lasers

Output power	Temperature	Frequency
1.34 W [143]	80 K	70 THz
26 mW [143]	313 K	70 THz
1.1 W [144]	200 K	50 THz
640 mW [144]	295 K	50 THz
162 mW [144]	298 K	47.6 THz
446 mW [145]	293 K	50 THz
30 mW [145]	333 K	50 THz
17 mW [146]	292 K	33 THz
3 mW [146]	312 K	33 THz
4 mW [147]	48 K	4.4 THz
1.8 mW [148]	10 K	3.2 THz
0.4 mW [148]	78 K	3.2 THz

To date, the highest reported temperature for a terahertz quantum cascade laser working at 3.2 THz is 93 K [148].

2.6 Terahertz Parametric Oscillators

The terahertz wave generation via the resonance of lattice and molecular vibration in the nonlinear optical crystals was predicted by Nishizawa in 1963 [149], [150]. In a terahertz parametric oscillator, the near infrared input (pump) photon stimulates a Stokes photon (idler) at a different frequency between the pump photon and the vibrational mode. The pump and idler photons interact inside the nonlinear optical crystal and generate a terahertz wave (signal), whose frequency is equal to the frequency difference of the pump and idler. In this process, the momentum is conserved, which indicates that the terahertz frequency can be tuned by controlling

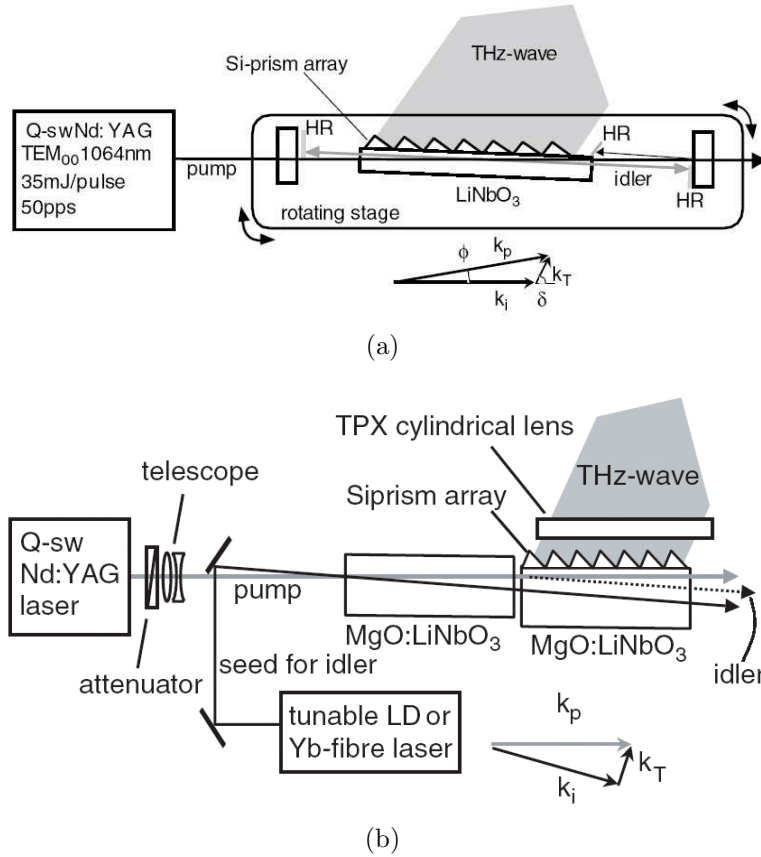


Figure 2.1: (a) Schematic of a terahertz parametric oscillator (TPO)(b) Injection-seeded terahertz parametric generator (IS-TPG).

the propagation direction. Different nonlinear optical crystals have been used for parametric terahertz wave generation, including LiNbO₃ [151], MgO : LiNbO₃ [152], GaSe [153], [154], ZnGeP₂ [153], GaP [155], [156], and DAST [157]- [159]. It has been shown that GaSe is one of the best nonlinear optical crystals, which has the lowest absorption coefficient in the terahertz domain and has large nonlinear coefficient [153].

Fig. 2.1(a) shows the schematic of a typical terahertz parametric oscillator (TPO) [151]. The pump laser is a bulky near infrared Q-switched Nd:YAG pulse laser with a pulse duration of 5-25 ns and a repetition rate of 10-50 Hz. The generated

Table 2.4: Characteristics of state-of-the-art terahertz parametric oscillators

Nonlinear optical crystal	peak power	Average power	Frequency
GaSe [161]	2364 W	118.2 μ W	51 THz
GaSe [161]	209 W	10.45 μ W	1.53 THz
DAST [158]	1-13.4 W	0.2-2.7 μ W	2-20 THz
DAST [159]	2.8 W	0.45 μ W	2.5 THz
GaP [162]	15.6 W	0.78 μ W	1.73 THz
GaP [156]	0.66 W	0.1 μ W	1.9 THz
GaP [156]	0.62 W	94 nW	2.6 THz
MgO : LiNbO ₃ [151]	100 mW	45 nW	1.58 THz
GaP [163]	100 mW	6 nW	2.5-5.6 THz

terahertz signal is a pulse with a duration of 5-10 ns, which can be consider as a continuous-wave signal in the terahertz frequency range. A TPO is continuously tunable in the 1-3 THz range with spectral linewidth of tens of GHz. It can emit peak powers of up to several tenths of a mW at room temperature.

Fig. 2.1(b) shows the schematic of an injection-seeded terahertz parametric generator (IS-TPG) [151], [160]. The pump is a single longitudinal mode Q-switched Nd:YAG laser working at 1064 nm. A CW Yb-fiber laser (1070 nm) or a tunable laser (1066-1074 nm) is used for seeding the idler. By introducing injection seeding to the idler, the spectrum linewidth of the generated terahertz signal can be narrowed to the Fourier transform limlit of the pulse width (less than 200 MHz) and the output power can be increased to several hundreds higher than that of TPOs [151]. A terahertz frequency tuning from 0.7 THz to 2.4 THz is possible using an external cavity laser diode as a tunable seeder.

The characteristics of the state-of-the-art terahertz parametric oscillators are given in Table 2.4.

2.7 Terahertz Photomixers

A terahertz photomixer is an optical heterodyne scheme, in which outputs of two CW single-mode lasers or output modes of a dual-mode laser with their frequency difference falling in the terahertz range mix in a nonlinear medium, such as a photoconductor or a superconductor, and generate a signal, whose frequency is equal to the frequency difference of the two lasers or two modes of the dual-mode laser. The generated signal can be coupled either to a transmission line for circuit applications or to an antenna to radiate the terahertz energy to the free space. The frequency of the generated terahertz signal can be tuned by tuning the central frequency of the lasers. Photomixers have the greatest tuning range among all the coherent sources in terahertz region.

The successfully developed terahertz photomixers to date are the antenna coupled photomixers, in which two CW laser beams are focused onto an area made of an appropriate dc biased ultra-fast photoconductor to generate carriers between closely spaced interdigitated electrodes connected to an antenna. Fig. 2.2 shows a typical interdigitated-electrode photomixer coupled to a dipole antenna [62]. For wideband applications bow-tie antenna or self-complementary log-spiral antenna have been used [42], [45], however, the maximum radiated power from these antennas is less than that of the resonant antennas. Low-temperature grown (LTG) GaAs has been widely used as the ultra-fast photoconductor in terahertz photomixers owing to its sub-picosecond carrier lifetime, high electric breakdown field ($> 50 \text{ V}/\mu\text{m}$), and relatively high carrier mobility ($> 100 \text{ cm}^2/\text{Vs}$). ErAs:GaAs also shows promising characteristics for terahertz photomixer applications [56], [63].

Shown in Fig. 2.3 is the equivalent circuit model for an antenna coupled photomixer device [65]. The terahertz power coupled to the antenna can be simply modeled

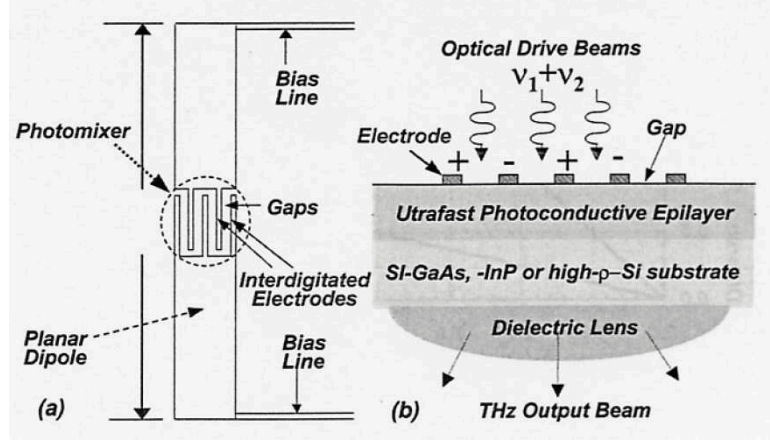


Figure 2.2: (a) Top view of interdigitated-electrode vertically-driven photomixer coupled to a planar dipole antenna (b) Cross-sectional view of photomixer showing bottom-side coupling of THz radiation through a dielectric lens to free space.

as [39], [65]

$$P_{THz}(\omega) = \frac{2R_A V_B^2 m P_1 P_2}{A} \left[\frac{\eta \mu e}{r h \nu} \right]^2 \frac{\tau^2}{1 + (\omega \tau)^2} \frac{1}{1 + (\omega R_A C)^2} \quad (2.1)$$

where R_A is the antenna's driving-point resistance, V_B is the DC bias, m is the modulation contrast, P_1 and P_2 are the power of the two lasers, A is the active area, η is the external quantum efficiency, μ is the carrier mobility, e is the charge of electron, r is the width of the photoconductive gap, $h\nu$ is the mean photon energy of the laser beam, ω is the beat frequency, τ is the carrier recombination lifetime, and C is the electrode capacitance.

As it can be seen from Eq. 2.1, at high frequencies the terahertz power decreases with frequency as $1/\omega^4$. The carrier lifetime roll-off term, $\frac{\tau^2}{1 + (\omega \tau)^2}$, is inevitable, but the other roll-off term due to the RC time constant can be avoided by operating the resonant antenna slightly away from its resonant frequency to cancel out the capacitive reactance of the photomixer by the antenna inductance [59]. It has

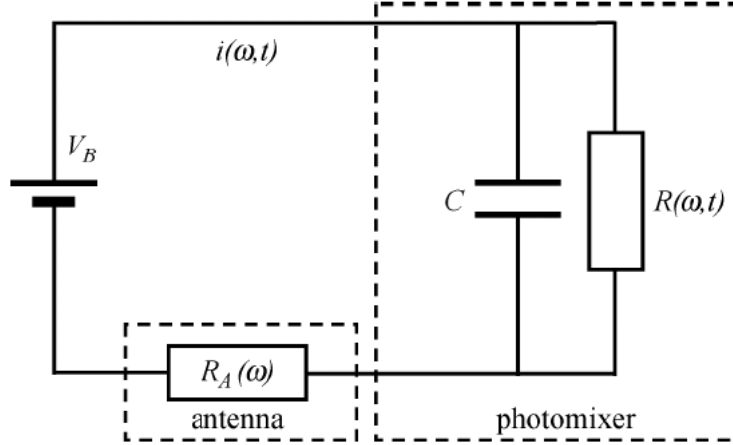


Figure 2.3: Equivalent circuit diagram for the photomixer and antenna. Current drawn from the bias source is modulated at angular frequency ω by the photoconductor, with resistance $R(\omega, t)$. The capacitance C represents the effects of the charge accumulating at the electrodes. Power is dissipated in the antenna, $R_A(\omega)$, of which the component oscillating with angular frequency ω is coupled out as terahertz radiation.

been shown that the RC time constant can also be bypassed in a traveling-wave photomixer structure [74] (see Fig. 2.4). In this structure, the generated terahertz signal couples to a transmission line structure if the propagation velocity of the line is matched to that of the terahertz signal.

The main drawback of the photomixers is their low output power at frequencies above 1 THz. Typical optical-to-electrical conversion efficiencies are below 10^{-5} for a single device and output power falls from $\approx 2 \mu\text{W}$ at 1 THz to below $0.1 \mu\text{W}$ at 3 THz [59], [63]. The maximum available terahertz power from a single photomixer device is limited by its maximum sustainable optical power and dc bias before device failure [78]. The total optical power that a photomixer made of LTG-GaAs can withstand at room temperature when biased at 30 V is about $0.9 \text{ mW}/\mu\text{m}^2$ [46]. The maximum sustainable optical power can be increased by growing the LTG-GaAs film on a higher-thermal-conductivity substrate such as

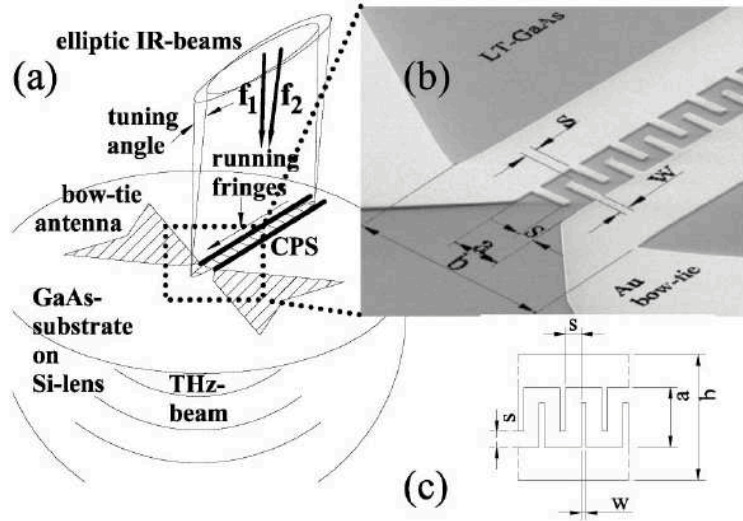


Figure 2.4: (a) Velocity-match of laser interference fringes to the THz wave on the coplanar stripline is obtained by a tuning-angle between the two laser beams (b) Scanning electron microscope picture of a traveling-wave metal-semiconductor-metal (TW-MSM) structure with inner part of bow-tie antenna (c) A section of TW-MSM.

silicon or diamond or by growing a heat spreader epilayer such as AlAs beneath the LTG-GaAs film [78]. To increase the laser-power-handling capability of the device, a traveling-wave photomixer has been proposed, in which the optical excitation is distributed over a bigger area [49], [74]. The other method for increasing the available terahertz power from the photomixers is confining the exciting laser beams close to the surface of the active layer by backing it up with a dielectric mirror to form an optical cavity between the top semiconductor/air interface and the dielectric mirror [73]. One can also increase the available terahertz power by making an array of photomixer elements [62].

Although most of the proposed terahertz photomixers use lasers with wavelengths between 750 and 850 nm, however, new materials that enable operation in the optical fiber communications band (1.3-1.55 μm) have been proposed [164]- [169]. The

two most promising materials are InGaAs containing ErAs particles [166], [167] and GaSb containing ErSb nanoparticles [165].

To date, the design optimization of the photomixers has been done based on a simplified model represented by Eq. (2.1). Although this simple model gives a good insight on the physics of the photoconductive photomixers and represents the main aspects of these devices, however, it does not predict all the behaviors of these devices that have been observed in experiments. In this dissertation, we develop a more comprehensive model for the photoconductive photomixers to facilitate the device design and optimization processes from material point of view. We also develop a comprehensive model for the superconductive photomixers, which are shown that are promising high-power terahertz sources. We also propose the integrated photomixer-antenna element, for which there is no RC time constant roll-off term and can be easily used in an array structure to increase the available terahertz power.

Fig. 2.5 wraps up this chapter by comparing the output power of different continuous-wave terahertz sources versus frequency.

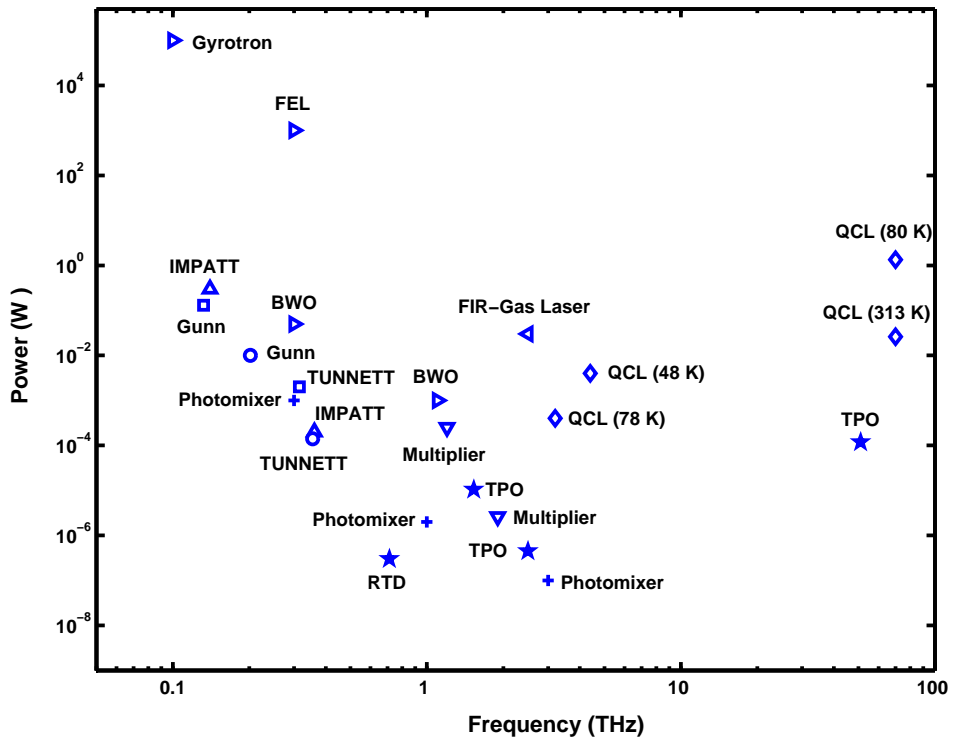


Figure 2.5: Output power of different continuous-wave terahertz sources versus frequency.

Chapter 3

Photomixing in Superconductors

3.1 Introduction

Exciting a superconductor material with a pair of interfering laser beams, whose frequency difference is in the terahertz range and have high energy photons (higher than binding energy of the Cooper pairs), modulates the density of quasiparticles and Cooper pairs in time and space via Cooper pair breaking effect. In the presence of a dc bias current, the modulated carrier densities generate a modulated photocurrent inside the superconductor material, which has a frequency harmonic in the terahertz range in its spectrum. The generated photocurrent can be either guided down to a transmission line for circuit applications or it can be radiated out by coupling to an antenna or by proper designing of the superconductor film to act as an efficient radiator.

3.2 Modeling of Superconductive Photomixers

Fig. 3.1 shows a typical photomixing scheme, in which two linearly polarized laser beams are applied to a dc current biased superconductor film located above a dielectric substrate. The laser beams are considered to be local plane-waves at the superconductor surface and are assumed to shine the entire surface of the superconductor film. The bath temperature, dc current, and current density are assumed to be below their critical values for the superconductor material. The associated electric fields for the two laser beams can be written as

$$E_{1(2)} = |E_{1(2)}| e^{j(\omega_{1(2)}t - \mathbf{k}_{1(2)} \cdot \mathbf{r})} \quad (3.1)$$

where $\omega_{1(2)}$ and $\mathbf{k}_{1(2)}$ are the lasers' angular frequencies and phase constants, respectively, and \mathbf{r} is the position vector. The incident optical power is proportional to the square of the total incident electric field

$$P_{inc}(\mathbf{r}, t) \propto |E_1|^2 + |E_2|^2 + 2|E_1||E_2| \cos(\Omega t - \mathbf{K} \cdot \mathbf{r}) \quad (3.2)$$

where $\Omega = \omega_1 - \omega_2$ is the angular beat frequency and $\mathbf{K} = \mathbf{k}_1 - \mathbf{k}_2$ is the grating vector. For the coordinate system in Fig. 3.1 the grating vector, \mathbf{K} , can be written as

$$\mathbf{K} = K_x \hat{x} + K_y \hat{y} + K_z \hat{z} \quad (3.3)$$

$$K_x = k_2 \sin \theta_2 \cos \phi_2 - k_1 \sin \theta_1 \cos \phi_1 \quad (3.4)$$

$$K_y = k_2 \sin \theta_2 \sin \phi_2 - k_1 \sin \theta_1 \sin \phi_1 \quad (3.5)$$

$$K_z = k_2 \cos \theta_2 - k_1 \cos \theta_1 \quad (3.6)$$

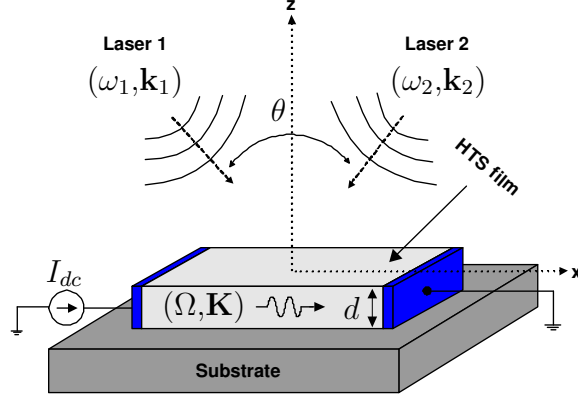


Figure 3.1: A typical superconductive photomixer scheme.

where θ_i and ϕ_i , $i = 1, 2$, are the azimuthal and polar angles of the two beams, respectively. The beat frequency is assumed to be less than the gap frequency of the superconductor material to avoid Cooper pair breaking effect due to the generated signal.

The incident optical power given by Eq. (3.2) is partially reflected from the superconductor-air surface and the rest is transmitted into the superconductor film. For the film thickness in the range of the optical penetration depth, the most part of the transmitted power is being absorbed by the superconductor material and a negligible amount of the power reaches to the superconductor-substrate interface. Hence the optical power inside the superconductor film can be written as

$$P(\mathbf{r}, t) = P_0(1 - R)[1 + \eta \cos(\Omega t - \mathbf{K} \cdot \mathbf{r})]e^{\alpha z} \quad (3.7)$$

where P_0 is the total power of the two lasers, R is the optical reflectivity, $0 < \eta \leq 1$ is the modulation index or grating contrast, and α is the optical absorption coefficient of the superconductor material.

The optical power given by Eq. (3.7) is being absorbed by the electrons via electron-

photon interaction and generates high energy quasiparticles by breaking Cooper pair bounds and also by exciting low energy quasiparticles. The high energy quasiparticles lose their energy via electron-electron and electron-phonon interaction. The energy does not dissipate in these mechanisms. The transferred energy to the phonons can be returned back to the electrons by electron-phonon interaction or it can be dissipated by phonon escape to the substrate. The quasiparticle and phonon energy spectrum upon optical illumination can be well described by Fermi-Dirac distribution function [170], which can be modeled by equivalent electron, T_e , and phonon, T_{ph} , temperatures, respectively. The change in the electron and phonon temperatures can be measured as impedance change in the superconductor film using modulated reflectivity or photoresponse (PR) methods [171].

The above-mentioned nonequilibrium mechanism can be modeled by a pair of coupled partial differential equations based on the two-temperature model [170]- [173]

$$C_e \frac{d}{dt} \hat{T}_e(\mathbf{r}, t) = K_e \nabla^2 \hat{T}_e(\mathbf{r}, t) - \frac{C_e}{\tau_{e-ph}} [\hat{T}_e(\mathbf{r}, t) - \hat{T}_{ph}(\mathbf{r}, t)] + \frac{P(\mathbf{r}, t)}{VT_c} \quad (3.8)$$

$$C_{ph} \frac{d}{dt} \hat{T}_{ph}(\mathbf{r}, t) = K_{ph} \nabla^2 \hat{T}_{ph}(\mathbf{r}, t) + \frac{C_e}{\tau_{e-ph}} [\hat{T}_e(\mathbf{r}, t) - \hat{T}_{ph}(\mathbf{r}, t)] - \frac{C_{ph}}{\tau_{es}} [\hat{T}_{ph}(\mathbf{r}, t) - \hat{T}_0] \quad (3.9)$$

where $\hat{T}_e(\mathbf{r}, t)$ and $\hat{T}_{ph}(\mathbf{r}, t)$ are the reduced electron and phonon temperatures, C_e and C_{ph} are the electron and phonon heat capacities, K_e and K_{ph} are the electron and phonon thermal conductivities, τ_{e-ph} is the electron-phonon relaxation time, τ_{es} is the phonon escape time to the substrate, \hat{T}_0 is the reduced bath temperature, T_c is the critical temperature, and V is the volume of the superconductor film. The terms at the left hand sides of Eqs. (3.8) and (3.9) are the rate of the energy storage in electron and phonon subsystems, respectively. The first terms at the right hand sides of Eqs. (3.8) and (3.9) represent the thermal diffusion mechanism and the

second terms represent the interaction of electron and phonon subsystems. The absorbed optical power comes into the equation for the electron subsystem, since the optical power is being absorbed by the electrons. The last term at the right hand side of Eq. (3.9) represents the phonon scape to the substrate.

In writing the Eqs. (3.8) and (3.9), we assume that the establishment of the electron temperature occurs during a time smaller than τ_{e-ph} and that within this time almost no energy is transferred from electrons to phonons. Although this assumption may not be valid for YBCO film, however, the two-temperature model provides a good description of the experimental results on nonequilibrium photoresponse of high-temperature superconductors [172].

Since the absorbed optical power contains a time-invariant as well as a time-varying component in its expression, the electron and phonon temperatures will also have time-invariant and time-varying components in their general expressions. Solving the coupled differential equations (3.8) and (3.9) with the absorbed optical power given by Eq. (3.7) results in the reduced electron and phonon temperatures as

$$\hat{T}_e(\mathbf{r}, t) = \hat{T}_{dc}^e + \hat{T}_{ac}^e \cos(\Omega t - \mathbf{K} \cdot \mathbf{r} - \phi_e) \quad (3.10)$$

$$\hat{T}_{ph}(\mathbf{r}, t) = \hat{T}_{dc}^{ph} + \hat{T}_{ac}^{ph} \cos(\Omega t - \mathbf{K} \cdot \mathbf{r} - \phi_{ph}) \quad (3.11)$$

Where

$$\hat{T}_{dc}^e = \hat{T}_0 + \frac{P_0(1-R)}{VT_c} \left(\frac{1}{G_{ph}} + \frac{1}{G_{e-ph}} \right) e^{\alpha z} \quad (3.12)$$

$$\hat{T}_{ac}^e = \frac{\eta P_0(1-R)}{VT_c} \left(\frac{\alpha_{ph}^2 + \beta_{ph}^2}{a^2 + b^2} \right)^{\frac{1}{2}} e^{\alpha z} \quad (3.13)$$

$$\hat{T}_{dc}^{ph} = \hat{T}_0 + \frac{P_0(1-R)}{VT_c} \frac{1}{G_{ph}} e^{\alpha z} \quad (3.14)$$

$$\hat{T}_{ac}^{ph} = \frac{\eta P_0(1-R)}{VT_c} \frac{G_{e-ph}}{\sqrt{a^2 + b^2}} e^{\alpha z} \quad (3.15)$$

in which

$$\alpha_{ph} = K_{ph}(|\mathbf{K}|^2 - \alpha^2) + G_{e-ph} + G_{ph} \approx G_{e-ph} \quad (3.16)$$

$$\alpha_e = K_e(|\mathbf{K}|^2 - \alpha^2) + G_{e-ph} \approx G_{e-ph} \quad (3.17)$$

$$\beta_{ph} = \Omega C_{ph} + 2\alpha K_z K_{ph} \approx \Omega C_{ph} \quad (3.18)$$

$$\beta_e = \Omega C_e + 2\alpha K_z K_e \approx \Omega C_e \quad (3.19)$$

$$a = \alpha_e \alpha_{ph} - \beta_e \beta_{ph} - G_{e-ph}^2 \approx -\Omega^2 C_e C_{ph} \quad (3.20)$$

$$b = \beta_{ph} \alpha_e + \beta_e \alpha_{ph} \approx \Omega G_{e-ph} (C_e + C_{ph}) \quad (3.21)$$

$$\phi_{ph} = \tan^{-1} \left(\frac{b}{a} \right) \quad (3.22)$$

$$\phi_e = \phi_{ph} + \tan^{-1} \left(\frac{\beta_{ph}}{\alpha_{ph}} \right) \quad (3.23)$$

where $G_{ph} = C_{ph}/\tau_{es}$ is the phonon mismatch coefficient and $G_{e-ph} = C_e/\tau_{e-ph}$ is the electron-phonon coupling coefficient. Note that both the electron and the phonon temperatures decrease along the thickness of the superconductor film, because less optical power absorption takes place at the points farther from the surface of the superconductor film.

Before applying the optical excitation, the electrons are in equilibrium with the phonons and with the substrate at the bath temperature, T_0 . Upon absorption of the optical power by the electrons, the electron and phonon temperatures increase above the bath temperature. The time-invariant component of the absorbed power causes an equal temperature increase for both the electron and the phonon subsystems. Knowing that $G_{e-ph} \gg G_{ph}$, it can be seen from Eqs. (3.12) and (3.14) that \hat{T}_{dc}^e is almost equal to \hat{T}_{dc}^{ph} , and both are proportional to the phonon escape time, τ_{es} . This is reasonable, since under the influence of a time-invariant optical power the electrons and phonons come into equilibrium in a time scale much shorter than

the time that the phonons need to escape to the substrate. The shorter the phonon escape time, the smaller the excess temperature of the electrons and phonons.

The time-varying components of the electron and phonon temperatures are not equal. The amplitude of the time-varying component of the electron temperature, \hat{T}_{ac}^e , is higher than that of the phonon temperature, \hat{T}_{ac}^{ph} , because of the higher heat capacity of the phonons. An approximate expression for \hat{T}_{ac}^e and \hat{T}_{ac}^{ph} from Eqs. (3.13) and (3.15) can be written as

$$\hat{T}_{ac}^{ph} \approx \frac{\eta P_0(1-R)}{VT_c} \frac{1}{\Omega C_{ph}} \frac{1}{[1 + \Omega^2 \tau_{e-ph}^2]^{\frac{1}{2}}} e^{\alpha z} \quad (3.24)$$

$$\begin{aligned} \hat{T}_{ac}^e &\approx \frac{\eta P_0(1-R)}{VT_c} \frac{1}{\Omega C_e} \left[\frac{C_e^2/C_{ph}^2 + \Omega^2 \tau_{e-ph}^2}{1 + \Omega^2 \tau_{e-ph}^2} \right]^{\frac{1}{2}} e^{\alpha z} \\ &\approx \frac{\eta P_0(1-R)}{VT_c C_{ph}} e^{\alpha z} \begin{cases} \frac{1}{\Omega}, & \Omega \tau_{e-ph} \ll 1 \\ \tau_{e-ph}, & C_e/C_{ph} < \Omega \tau_{e-ph} < 1 \\ \frac{C_{ph}}{C_e} \frac{1}{\Omega}, & \Omega \tau_{e-ph} \gg 1 \end{cases} \end{aligned} \quad (3.25)$$

Comparing Eqs. (3.24) and (3.25), one can show

$$\hat{T}_{ac}^e \approx \left[1 + \frac{C_{ph}^2}{C_e^2} \Omega^2 \tau_{e-ph}^2 \right]^{\frac{1}{2}} \hat{T}_{ac}^{ph} \quad (3.26)$$

From Eq. (3.26), it can be seen that the higher the value of $\Omega \tau_{e-ph}$ the bigger the difference between \hat{T}_{ac}^e and \hat{T}_{ac}^{ph} . The higher value of $\Omega \tau_{e-ph}$ means that it takes longer time for the electrons to be in equilibrium with the phonons.

The excess time-invariant electron temperature, $(\hat{T}_{ac}^e - \hat{T}_0)$, is much more higher than the amplitude of the time-varying component of the electron temperature.

From Eqs. (3.12) and (3.13) and for $\eta = 1$, one can show

$$\begin{aligned}\hat{T}_{dc}^e - \hat{T}_0 &\approx \left(\Omega \tau_{es} \frac{C_e}{C_{ph}} \right) \left[\frac{1 + \Omega^2 \tau_{e-ph}^2}{C_e^2 / C_{ph}^2 + \Omega^2 \tau_{e-ph}^2} \right]^{\frac{1}{2}} \hat{T}_{ac}^e \\ &\approx \left(\frac{C_e \tau_{es}}{C_{ph} \tau_{e-ph}} \right) \hat{T}_{ac}^e, \quad C_e / C_{ph} < \Omega \tau_{e-ph} < 1\end{aligned}\quad (3.27)$$

The phonon escape time, τ_{es} , is in the order of nanoseconds, while the electron-phonon relaxation time, τ_{e-ph} , is in the order of sub-picosecond, hence $\hat{T}_{dc}^e - \hat{T}_0 \gg \hat{T}_{ac}^e$. This means that the most part of the absorbed optical power is being spent to increase the time-invariant part of the electron temperature.

Generally, the electron-phonon relaxation time is a function of temperature, especially for the temperatures close to the critical temperature of the superconductor material [174], [175]. To have a precise solution to the Eqs. (3.8) and (3.9), one has to include the temperature dependency of the electron-phonon relaxation time in these equations. The resulting nonlinear equations are difficult to solve. A good approximation for the electron and phonon temperatures are the solutions given by Eqs. (3.10) to (3.23), where τ_{e-ph} is calculated from the following empirical formula [175]

$$\tau_{e-ph} = \tau_{e-ph}(T_c) \frac{1 + \beta [(\hat{T}_{dc}^{ph})^{1-\gamma} - \hat{T}_{dc}^{ph}]}{\hat{T}_{dc}^{ph}}, \quad \hat{T}_{dc}^{ph} \leq 1 \quad (3.28)$$

where $\tau_{e-ph}(T_c)$ is the momentum relaxation time at the critical temperature and β is the residual resistance rate. Note that \hat{T}_{dc}^{ph} is independent of τ_{e-ph} and is given by Eq. (3.14).

One can define critical optical power as a power at which the maximum value of the electron temperature becomes equal to the critical temperature, T_c . Using Eq.

(3.10), the critical optical power can be written as

$$\begin{aligned}
P_c &= \frac{V(T_c - T_0)}{1 - R} e^{-\alpha z} \left[\frac{1}{G_{ph}} + \frac{1}{G_{e-ph}} + \eta \left(\frac{\alpha_{ph}^2 + \beta_{ph}^2}{a^2 + b^2} \right)^{\frac{1}{2}} \right]^{-1} \\
&\approx \frac{V(T_c - T_0)}{1 - R} G_{ph} e^{-\alpha z}
\end{aligned} \tag{3.29}$$

In order to stay in the superconducting region, the total lasers power, P_0 , must be less than the critical optical power, P_c .

Based on the two-fluid model [176], one can write the total photocurrent inside the superconductor film as

$$\mathbf{J}(\mathbf{r}, t) = \mathbf{J}_n(\mathbf{r}, t) + \mathbf{J}_s(\mathbf{r}, t) \tag{3.30}$$

where $\mathbf{J}_n(\mathbf{r}, t)$ and $\mathbf{J}_s(\mathbf{r}, t)$ are the densities of the normal-current (flow of the quasi-particles) and super-current (flow of the Cooper pairs), respectively. When there is no optical excitation, the super-current is almost equal to the dc bias current (I_{dc}) and the normal-current is too small. At the presence of the optical excitation, the absorbed optical power breaks some of the Cooper pairs and hence the super-current fraction decreases, while the remaining Cooper pairs only participate in dc current flow mechanism to minimize the ohmic loss. Since the total dc current must be equal to the dc bias current, I_{dc} , the quasiparticles compensate for the decrease in the dc current and also carry the generated terahertz photocurrent. The density of the quasiparticles and the Cooper pairs are assumed to be controlled by the electron temperature.

The Cooper pairs undergo a collision-less motion under the influence of the applied bias current, which can be modeled by London's first equation [176]

$$\mathbf{E}(\mathbf{r}, t) = \mu_0 \frac{\partial}{\partial t} [\lambda^2(\mathbf{r}, t) \mathbf{J}_s(\mathbf{r}, t)] \tag{3.31}$$

where $\mathbf{E}(\mathbf{r}, t)$ is the electric field inside the superconductor film and $\lambda(\mathbf{r}, t)$ is the London penetration depth given by [175]

$$\lambda^2(\mathbf{r}, t) = \frac{\lambda_L^2(0)}{1 - [\hat{T}_e(\mathbf{r}, t)]^\gamma} \quad (3.32)$$

where $\lambda_L(0)$ is the London penetration depth at zero temperature and $\gamma = 1.3$ to 2.1 is an exponent.

The super-electron density according to the above mentioned model is a dc current in the direction of the applied dc bias current

$$\mathbf{J}_s(\mathbf{r}, t) = \mathbf{J}_0 \quad (3.33)$$

The normal current density is the result of the drift and diffusion mechanisms of the quasiparticles

$$\mathbf{J}_n(\mathbf{r}, t) = en_n(\mathbf{r}, t)\mathbf{v}_n(\mathbf{r}, t) + eD_n\nabla n_n(\mathbf{r}, t) \quad (3.34)$$

where e is the electron charge, $n_n(\mathbf{r}, t)$ is the quasiparticle density, $\mathbf{v}_n(\mathbf{r}, t)$ is the velocity of the quasiparticles, and D_n is the quasiparticle diffusion coefficient. The quasiparticle density in terms of the reduced electron temperature is given by [175]

$$n_n(\mathbf{r}, t) = n_0[\hat{T}_e(\mathbf{r}, t)]^\gamma, \quad \hat{T}_e(\mathbf{r}, t) \leq 1 \quad (3.35)$$

where n_0 is the total electron density.

The motion of the quasiparticles under the influence of the electric field, $\mathbf{E}(\mathbf{r}, t)$,

inside the superconductor material can be modeled by [176]

$$\mathbf{E}(\mathbf{r}, t) = \frac{m}{e} \frac{\partial \mathbf{v}_n(\mathbf{r}, t)}{\partial t} + \frac{m}{e\tau_{e-ph}} \mathbf{v}_n(\mathbf{r}, t) \quad (3.36)$$

where m is the mass of an electron. Note that the electric field and the drift velocity vectors are assumed to be in the same direction for convenience.

Note that the London's first equation (Eq. 3.31) has also a nonlinear term in its general form, which comes from the $\mathbf{v}_s \times \mathbf{B}$ term in the Lorentz's law for the super-electron motion equation [176]. Also Eq. (3.36) needs an $\mathbf{v}_n \times \mathbf{B}$ term on its left hand side coming from Lorentz's law. These additional terms are perpendicular to the direction of the applied dc bias current and do not affect the photocurrent element in the direction of the bias current. Hence the equations given by (3.31)-(3.36) are a complete set of equations that must be solved in order to find the dominant photocurrent element inside the superconductor film.

Knowing that $\hat{T}_{ac}^e \ll \hat{T}_{dc}^e$ and the fact that the average of the total current inside the superconductor film is equal to the dc bias current (there is no injection of excess charge into the superconductor film), one can solve Eqs. (3.31) to (3.36) to find the total photocurrent as

$$J(\mathbf{r}, t) = J_{dc} + \Re e\{\tilde{J}e^{j\Omega t}\} \quad (3.37)$$

where

$$J_{dc} = \frac{I_{dc}}{wd} \quad (3.38)$$

$$\tilde{J} = (J_1^2 + J_2^2)^{\frac{1}{2}} e^{-j\phi} e^{-j\mathbf{K}\cdot\mathbf{r}} \quad (3.39)$$

$$J_1 = \frac{\mu_0 \sigma_n \tau_{e-ph} \Omega^2 \lambda_L^2(0) \gamma \hat{T}_{ac}^e (\hat{T}_{dc}^e)^{2\gamma-1}}{1 + \Omega^2 \tau_{e-ph}^2} J_0 \quad (3.40)$$

$$J_2 = -\frac{\mu_0 \sigma_n \Omega \lambda_L^2(0)}{1 + \Omega^2 \tau_{e-ph}^2} \frac{\gamma \hat{T}_{ac}^e (\hat{T}_{dc}^e)^{2\gamma-1}}{[1 - (\hat{T}_{dc}^e)^\gamma]^2} J_0 + en_0 \gamma D_n K_x (\hat{T}_{dc}^e)^{\gamma-1} \hat{T}_{ac}^e \quad (3.41)$$

$$J_0 = J_{dc} \left[1 + \frac{\mu_0 \sigma_n \tau_{e-ph} \Omega^2 \lambda_L^2(0)}{2(1 + \Omega^2 \tau_{e-ph}^2)} \frac{\gamma^2 (\hat{T}_{ac}^e)^2 (\hat{T}_{dc}^e)^{2\gamma}}{[1 - (\hat{T}_{dc}^e)^\gamma]^2} \right]^{-1} \quad (3.42)$$

$$\phi = \phi_e + \tan^{-1} \frac{J_2}{J_1} \quad (3.43)$$

in which $\sigma_n = n_0 e^2 \tau_{e-ph} / m$ is the normal conductivity.

The generated terahertz power inside the superconductor film can be calculated as

$$P_{THz} = \frac{1}{T} \int_0^T \left[\iiint_V E(r, t) J(r, t) dx dy dz \right] dt \quad (3.44)$$

where $T = 2\pi/\Omega$ is the temporal period of the generated terahertz signal. One can calculate the electric field, $E(r, t)$, from Eqs. (3.10) and (3.31) to (3.33) as

$$E(r, t) = \mu_0 \gamma \Omega \lambda_L^2(0) \frac{\hat{T}_{ac}^e (\hat{T}_{dc}^e)^{\gamma-1}}{[1 - (\hat{T}_{dc}^e)^\gamma]^2} \sin(\Omega t - \mathbf{K} \cdot \mathbf{r} - \phi_e) \quad (3.45)$$

Substituting Eqs. (3.37) and (3.45) into Eq. (3.44) and doing the integration results in

$$P_{THz} = \frac{1}{2} l w \mu_0 \gamma \Omega \lambda_L^2(0) \int_{-d}^0 \frac{\hat{T}_{ac}^e (\hat{T}_{dc}^e)^{\gamma-1}}{[1 - (\hat{T}_{dc}^e)^\gamma]^2} J_0(z) J_2(z) dz \quad (3.46)$$

The optical-to-electrical conversion efficiency can be defined as

$$\eta_c = \frac{P_{THz}}{P_0} \quad (3.47)$$

3.3 Simulation Results for an YBCO Photomixer

High-temperature superconductors are more desirable for terahertz photomixer applications because of their higher gap frequencies and higher critical temperatures compare to the low-temperature superconductors. The physical parameters of a superconductive photomixer made of $\text{YBa}_2\text{Cu}_3\text{O}_{7-\delta}$ thin film, which is located above an LaAlO_3 substrate with relative permittivity of $\epsilon_r = 24$ are given in Table 3.1. The two lasers are located in $(x-z)$ plane and are symmetric with respect to z -axis. The central wavelength of one of the lasers is fixed at 532 nm. The other laser is a tunable laser, which its central wavelength can be tuned around 532 nm. The desired terahertz beat frequency is the result of the frequency difference of the two lasers. The angle between the two laser beams is $\theta = 10^\circ$ and the lasers modulation index is $\eta = 1$. At the beat frequency equal to 1 THz, the resulting grating vector components are $K_x = 1.402 \times 10^6$ rad/m, $K_y = -1.825 \times 10^3$ rad/m, and $K_z = -2.086 \times 10^4$ rad/m. The dc current bias is 23.8 mA.

Fig. 3.2 shows critical optical power versus distance from the surface of the superconductor film at different bath temperatures. The critical optical power is minimum at the surface of the film, since most of the optical power is being absorbed at the surface and hence the electron temperature is maximum at this point. It also can be seen that for the higher bath temperatures the critical optical power is smaller. The total power of the lasers must be smaller than the critical optical power at the surface of the superconductor film.

Amplitude of the time-varying components of the electron and phonon temperatures at the surface of the superconductor film ($z = 0$) are shown in Fig. 3.3 versus beat frequency. The total laser power is fixed at 150 mW, which is lower than the minimum of the critical optical power at $T_0 = 82$ K (Fig. 3.2). At low fre-

Table 3.1: Physical parameters of a photomixer made of $\text{YBa}_2\text{Cu}_3\text{O}_{7-\delta}$

Description	Notation	Value
Critical temperature [177]	T_c	87 K
Critical current [177]	I_c	25 mA
Critical current density [177]	J_c	$9.6 \times 10^5 \text{ A/cm}^2$
Exponent [175]	γ	1.68
Residual resistance rate [175]	β	10
London penetration depth [175]	$\lambda_L(0)$	220 nm
Optical penetration depth [177]	δ	90 nm
Optical reflectivity [177]	R	0.1
Optical absorption coefficient [178]	α	$1.1 \times 10^5 \text{ cm}^{-1}$
Electron heat capacity [172]	C_e	$0.022 \text{ Jcm}^{-3}\text{K}^{-1}$
Phonon heat capacity [177]	C_{ph}	$0.85 \text{ Jcm}^{-3}\text{K}^{-1}$
Electron thermal conductivity [179]	K_e	$0.4 \text{ Wm}^{-1}\text{K}^{-1}$
Phonon thermal conductivity [179]	K_{ph}	$0.1 \text{ Wm}^{-1}\text{K}^{-1}$
Phonon escape time [177]	τ_{es}	12 ns
Electron-phonon relaxation time [175]	$\tau_{e-ph}(T_c)$	$3.57 \times 10^{-14} \text{ s}$
Normal state conductivity [175]	$\sigma_n(T_c)$	$1.8 \times 10^6 (\Omega\text{m})^{-1}$
Superconductor film thickness [177]	d	130 nm
Superconductor film length [177]	l	200 μm
Superconductor film width [177]	w	20 μm
Quasiparticle diffusion coefficient [180]	D_n	24 cm^2/s
Total electron density [181]	n_0	$0.4 \times 10^{22} \text{ cm}^{-3}$

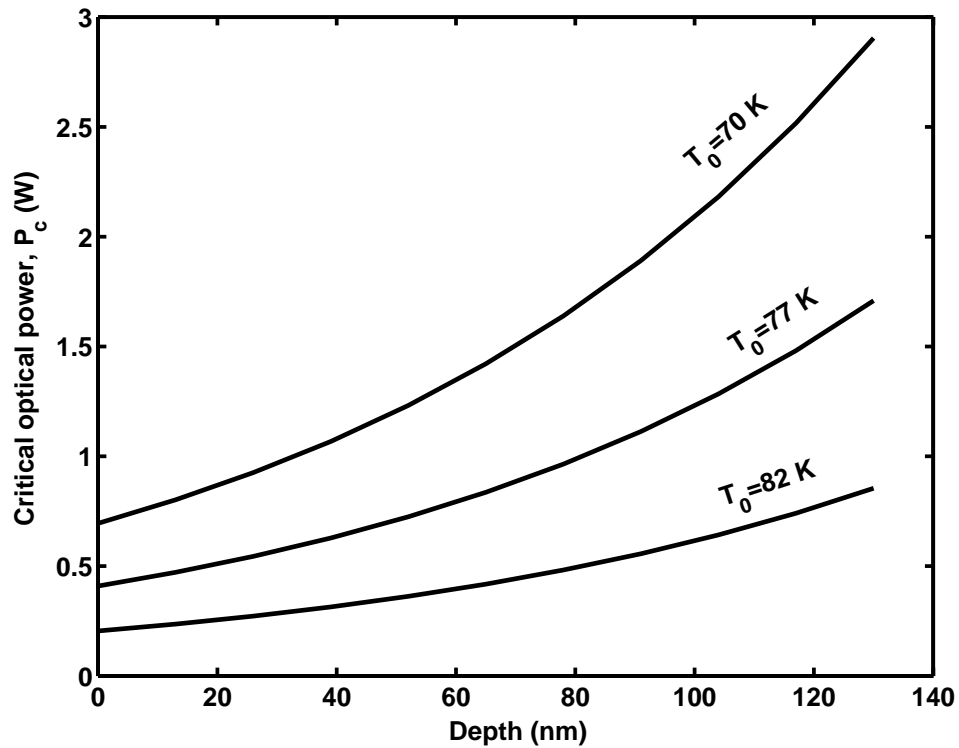


Figure 3.2: Critical optical power versus distance from the surface of the superconductor film at different bath temperatures. The critical temperature is $T_c = 87$ K.

quencies and for smaller electron-phonon relaxation times, the quasiparticles have enough time to lose their excess energy to the phonons and be in equilibrium with the phonons. At higher frequencies the quasiparticles can not deliver their excess energy to the phonons as their temperature changes rapidly with time and hence they are not in equilibrium with the phonons. The difference between the electron and phonon temperatures is bigger at higher frequencies and for higher electron-phonon relaxation times. The phonon temperature decreases by frequency by $1/\Omega$ for $\Omega\tau_{e-ph} \ll 1$ and can turn to the rate of $1/\Omega^2$ if $\Omega\tau_{e-ph} \gg 1$ (see Eq. (3.24)). The electron temperature decreases by frequency by $1/\Omega$ for $\Omega\tau_{e-ph} \ll 1$. As the beat frequency increases the electron temperature becomes almost independent of the frequency when $C_e/C_{ph} < \Omega\tau_{e-ph} < 1$ and then it returns back to the rate of $1/\Omega$ for $\Omega\tau_{e-ph} \gg 1$ (see Eq. (3.25)).

Shown in Fig. 3.4 is amplitude of the time-varying component of the electron temperature versus bath temperature at different beat frequencies. For the most values of the beat frequencies and the bath temperatures, T_{ac}^e decreases when the bath temperature increases. It can be seen from Eq. (3.25) that for $C_e/C_{ph} < \Omega\tau_{e-ph} < 1$ the electron temperature is proportional to the electron-phonon relaxation time, which decreases when the bath temperature approaches to the superconductor critical temperature. There are two extreme ranges for $\Omega\tau_{e-ph}$, for which T_{ac}^e is independent of τ_{e-ph} and hence is independent of the bath temperature.

The drift and diffusion current components given at the right hand side of Eq. (3.41) are depicted versus beat frequency for two different bath temperatures in Fig. 3.5. As it can be seen from Fig. 3.5, for the electron temperatures far below the critical temperature, the diffusion current is dominant (solid curves), while for the electron temperatures close to the critical temperature the drift current becomes dominant (dashed curves). Note that one can push the electron temperature close

to its critical value by either increasing the bath temperature T_0 or by increasing the optical power P_0 .

Fig. 3.6 shows total photocurrent at the surface of the superconductor film versus beat frequency for $\theta = 10^\circ$ and for different bath temperatures. At the low temperatures, the diffusion current is dominant and the total current decreases by frequency. As the bath temperature increases, the drift current starts to dominate the total current mostly at the higher beat frequencies. At the high enough bath temperatures, where the electron temperature is close to its critical value, the drift current dominates the total photocurrent and the current increases with beat frequency. The diffusion current is also a function of the angle between the two laser beams via K_x . At the limit of $\theta = 0$, where there is no spacial change for the quasiparticle density, the diffusion current becomes zero. Fig. 3.7 shows the total photocurrent at the surface of the superconductor film for the case of $\theta = 0$. In this case the photocurrent is only the result of the quasiparticle drift mechanism inside the superconductor film. The maximum obtainable frequency is limited by the gap frequency of the YBCO sample, which can be from 5 THz to 30 THz for different samples.

Shown in Fig. 3.8 is total photocurrent at the surface of the superconductor film versus bath temperature for different values of beat frequency. One can see that the amplitude of the terahertz photocurrent super-linearly increases with the bath temperature for the temperatures close to the critical temperature.

The amplitude of the photocurrent is not uniform along the thickness of the superconductor film. Figs. 3.9 and 3.10 show variation of the amplitude of the photocurrent along the thickness of the superconductor film for different values of beat frequency and at two different bath temperatures. Comparing Figs. 3.9 and 3.10 shows that at the bath temperature $T_0 = 82$ K the amplitude of the pho-

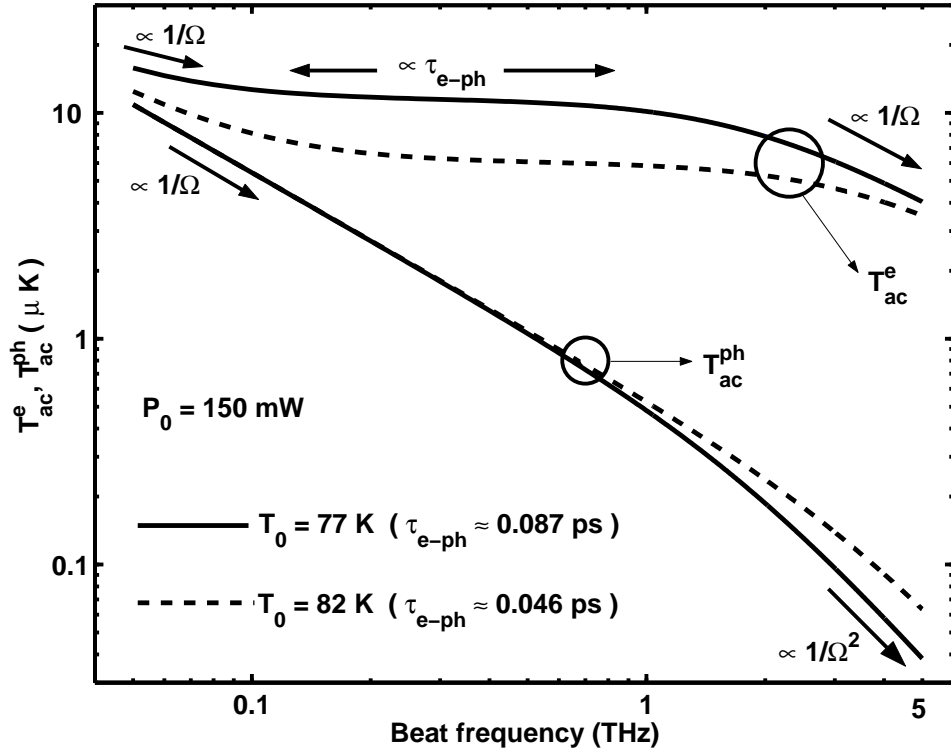


Figure 3.3: Amplitude of the time-varying components of the electron and phonon temperatures. The dc current bias is 23.8 mA.

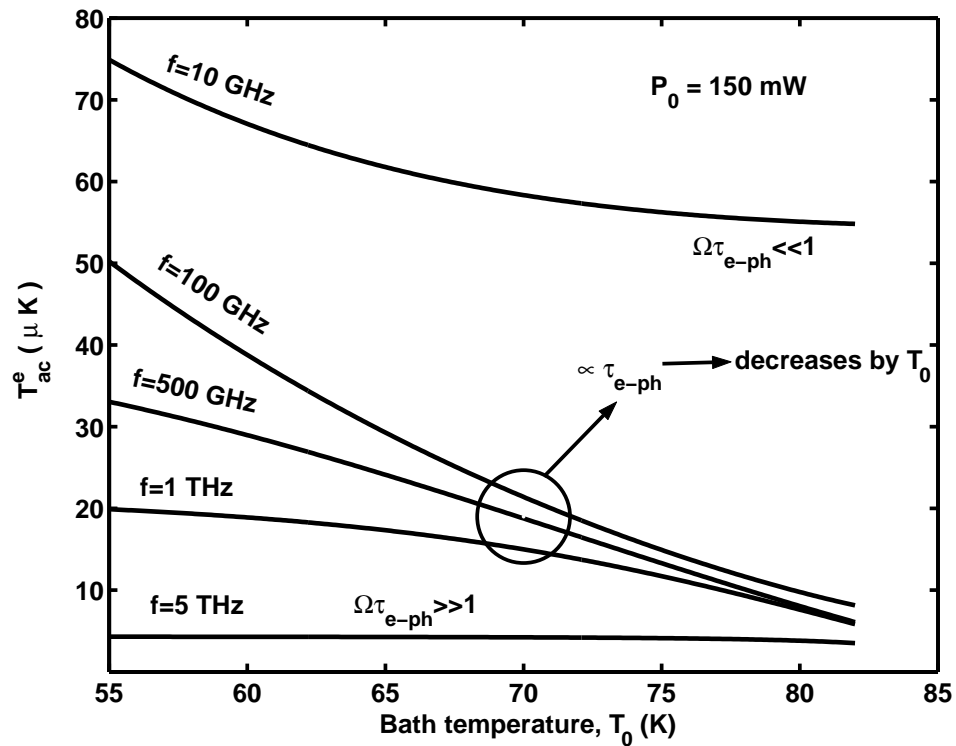


Figure 3.4: Amplitude of the time-varying component of the electron temperature versus bath temperature at different beat frequencies.

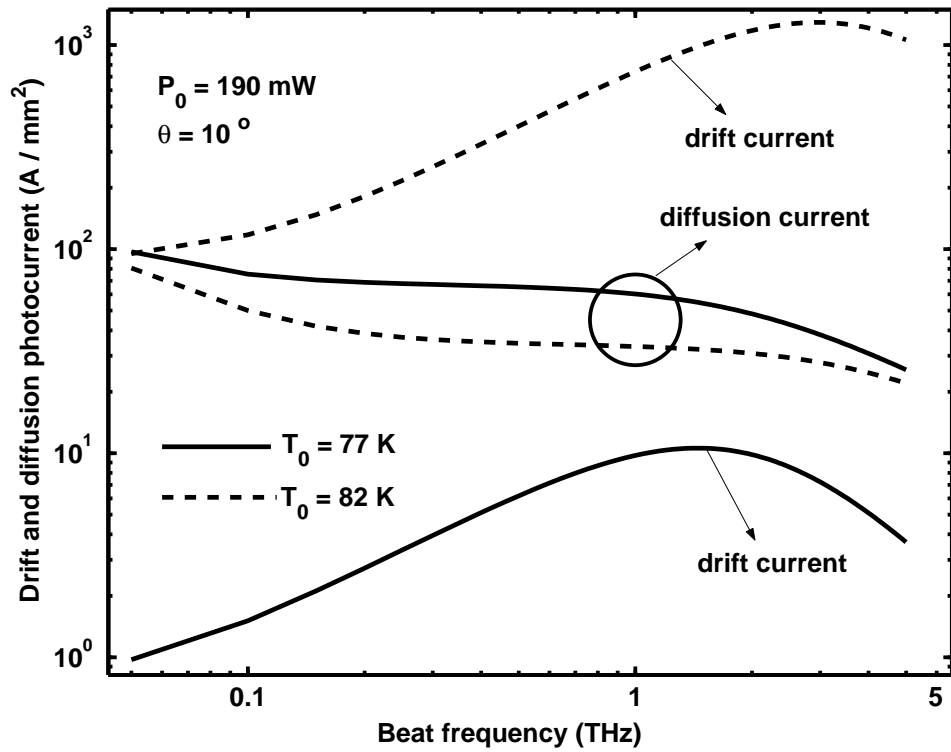


Figure 3.5: Drift and diffusion components of photocurrent given at the right hand side of Eq. (3.41) for two different bath temperatures. The critical temperature is $T_c = 87 \text{ K}$.

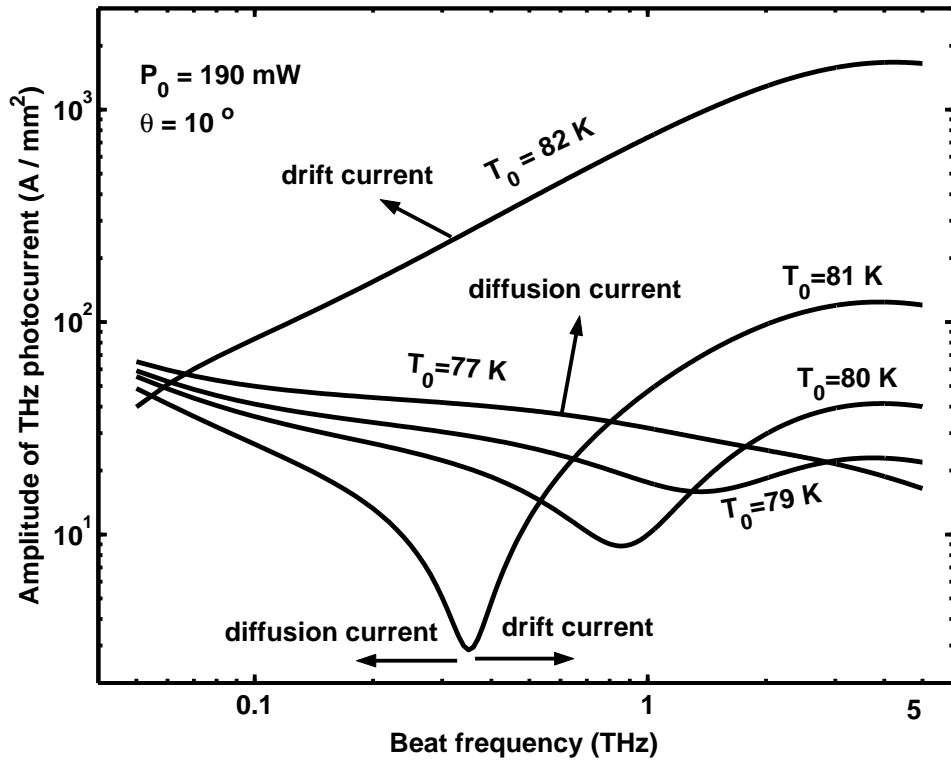


Figure 3.6: Total photocurrent at the surface of the YBCO film versus beat frequency for $\theta = 10^\circ$ and at different bath temperatures. The critical temperature is $T_c = 87 \text{ K}$.

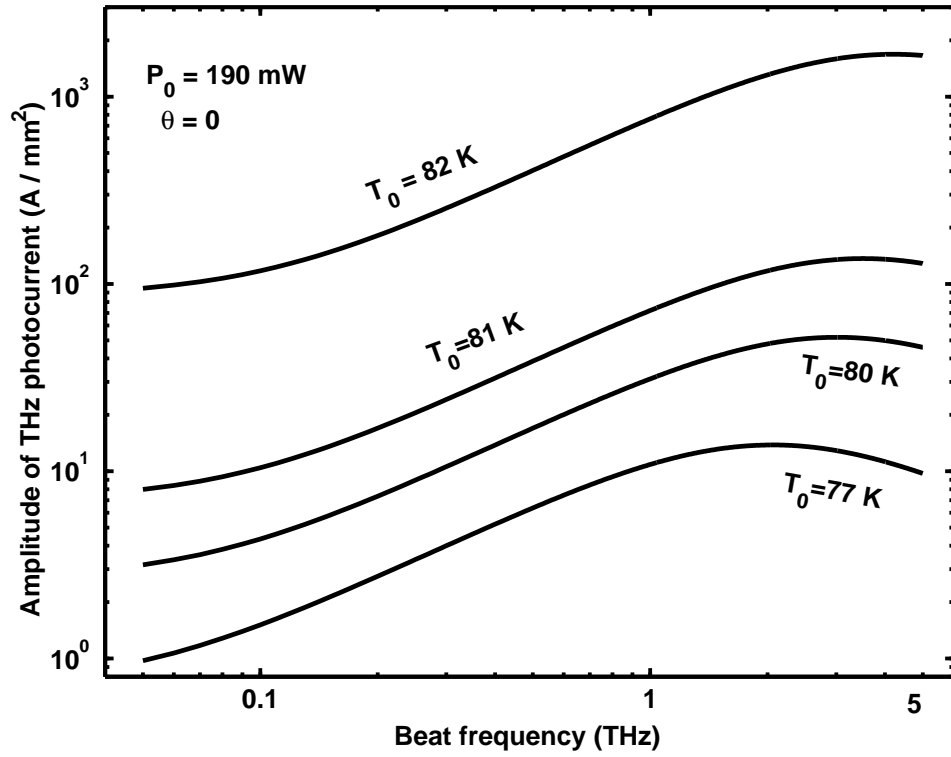


Figure 3.7: Total photocurrent at the surface of the YBCO film versus beat frequency for $\theta = 0$ and at different bath temperatures. The critical temperature is $T_c = 87 \text{ K}$.

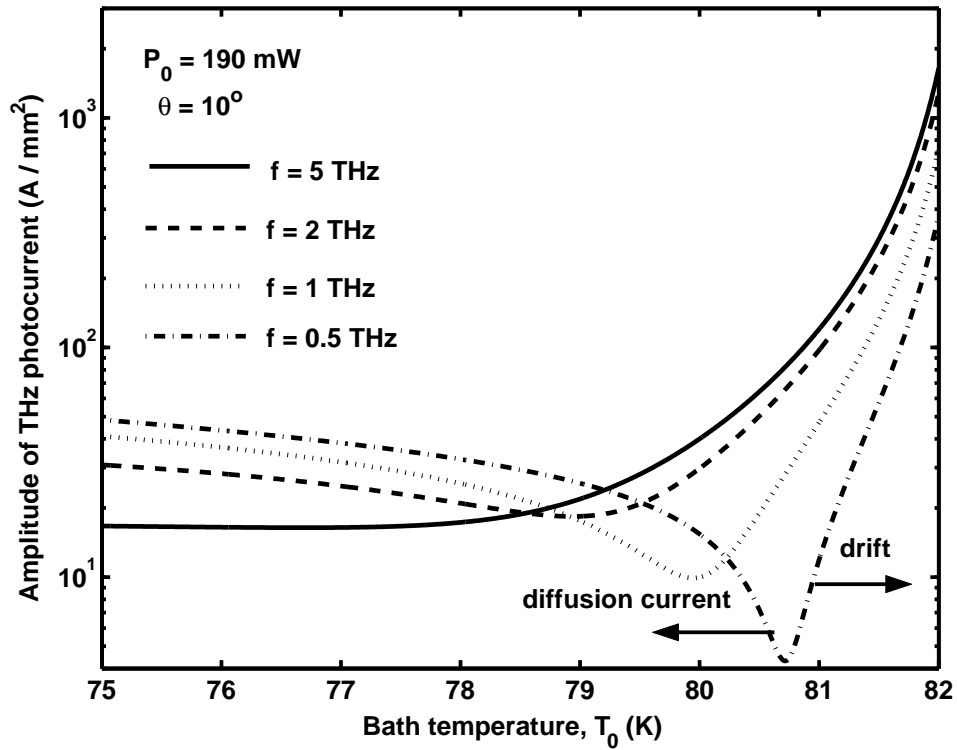


Figure 3.8: Total photocurrent at the surface of the YBCO film versus bath temperature for $\theta = 10^\circ$ and at different beat frequencies.

tocurrent decreases rapidly along the thickness of the superconductor film, while at $T_0 = 77$ K the amplitude of the photocurrent decreases slowly along the thickness. Concentration of the photocurrent near the surface of the superconductor film will increase the terahertz radiation power if the film is designed to act as an efficient radiator.

According to Eq. (3.39), the generated terahertz photocurrent inside the superconductor film is a traveling-wave signal associated with $e^{-j\mathbf{K}\cdot\mathbf{r}}$ term and also has a constant phase term $e^{-j\phi}$. Fig. 3.11 shows variation of the phase ϕ with angle between the two laser beam at different bath temperatures. At lower temperatures, the diffusion current, which is proportional to the grating vector component K_x , is dominant and hence ϕ strongly depends on θ . As the bath temperature increases, the drift current dominates and the phase ϕ becomes independent of θ . Also the components of the grating vector, \mathbf{K} , are functions of θ . In chapter 7 we will show how one can use this property to steer the radiation beam of an array made of superconductive photomixers.

Generated terahertz power inside the superconductor film is shown in Fig. 3.12 versus total power of the lasers for different bath temperatures. At the high bath temperature drift current dominates and hence terahertz power increases super-linearly by temperature. The optical-to-electrical conversion efficiency at $T_0 = 82$ K and for $P_0 = 190$ mW is %0.003.

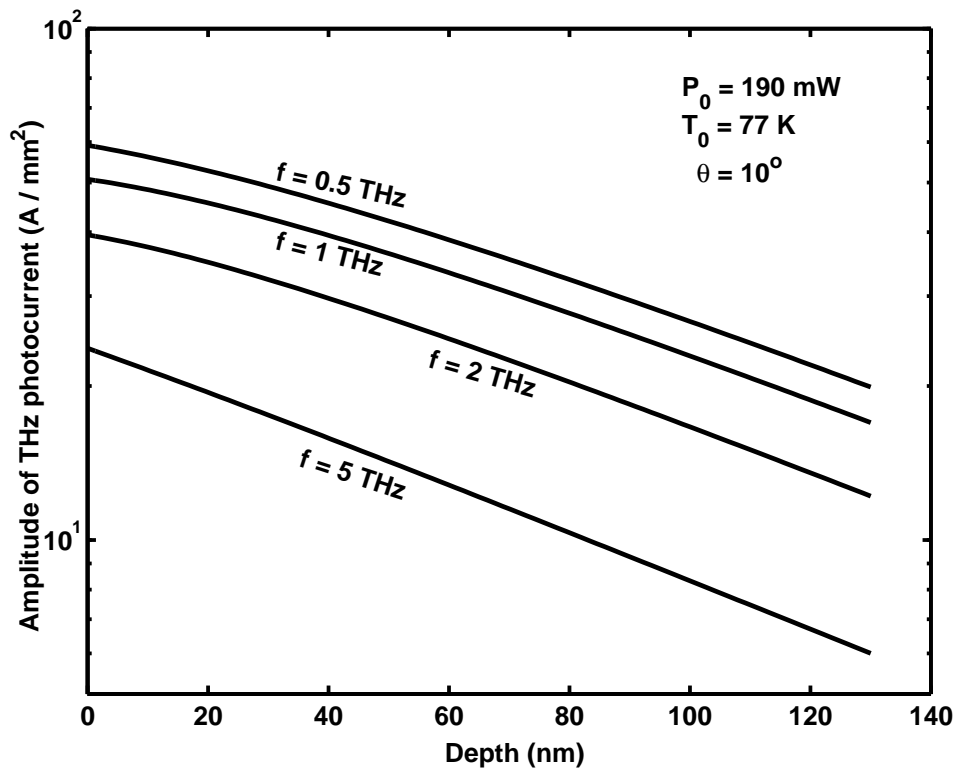


Figure 3.9: Total photocurrent along the thickness of the YBCO film at $T_0 = 77\text{K}$.

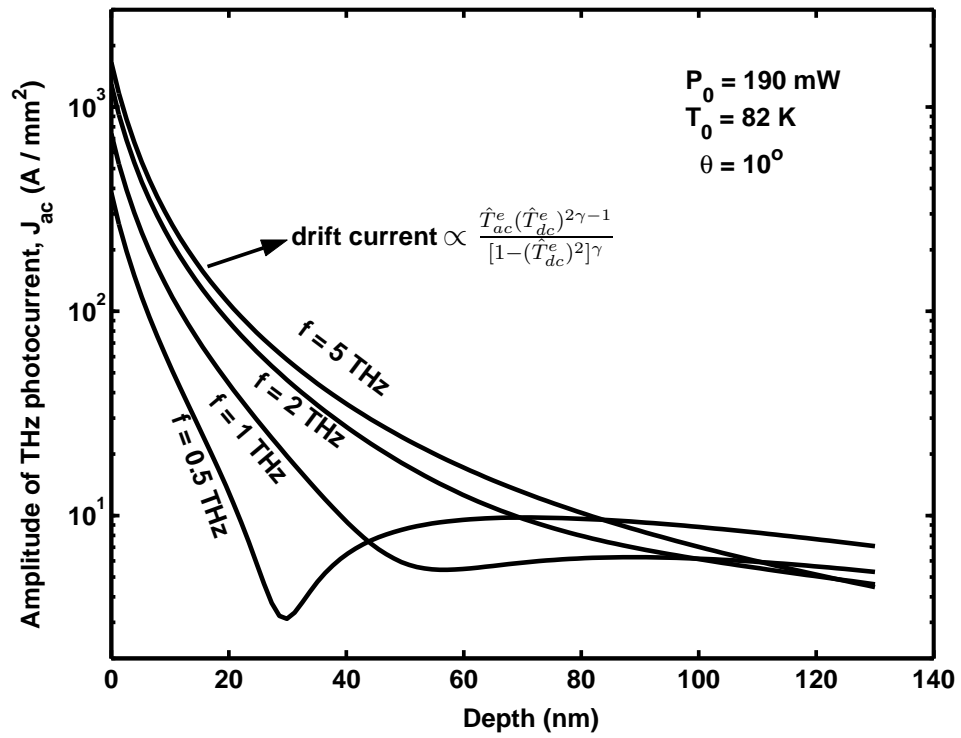


Figure 3.10: Total photocurrent along the thickness of the YBCO film at $T_0 = 82$ K.

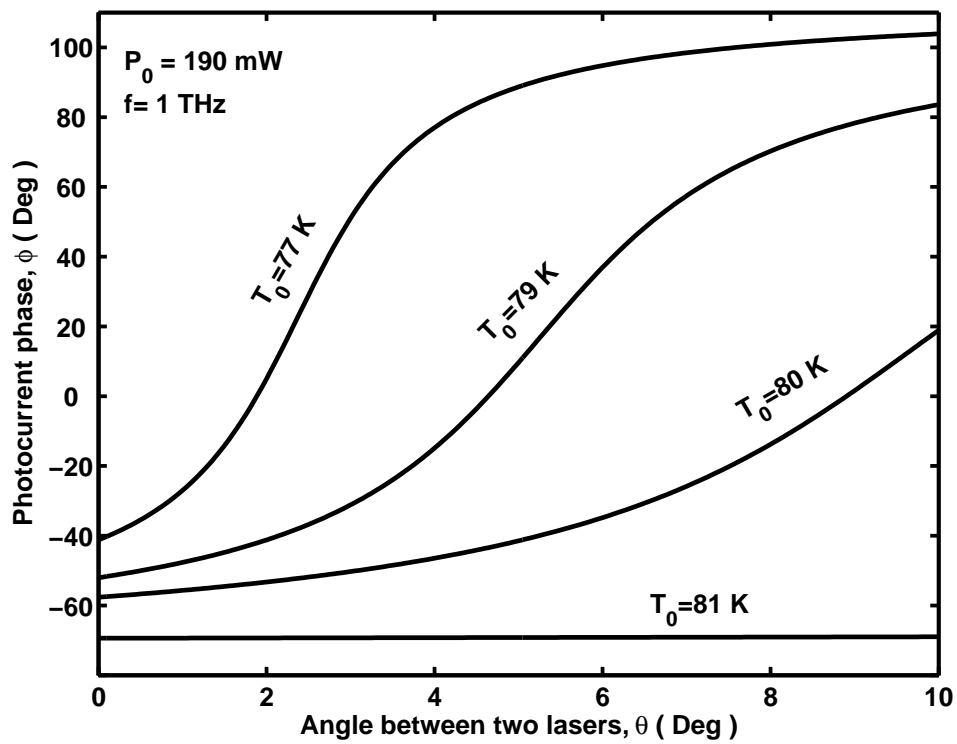


Figure 3.11: Phase of photocurrent versus angle between the two laser beams.

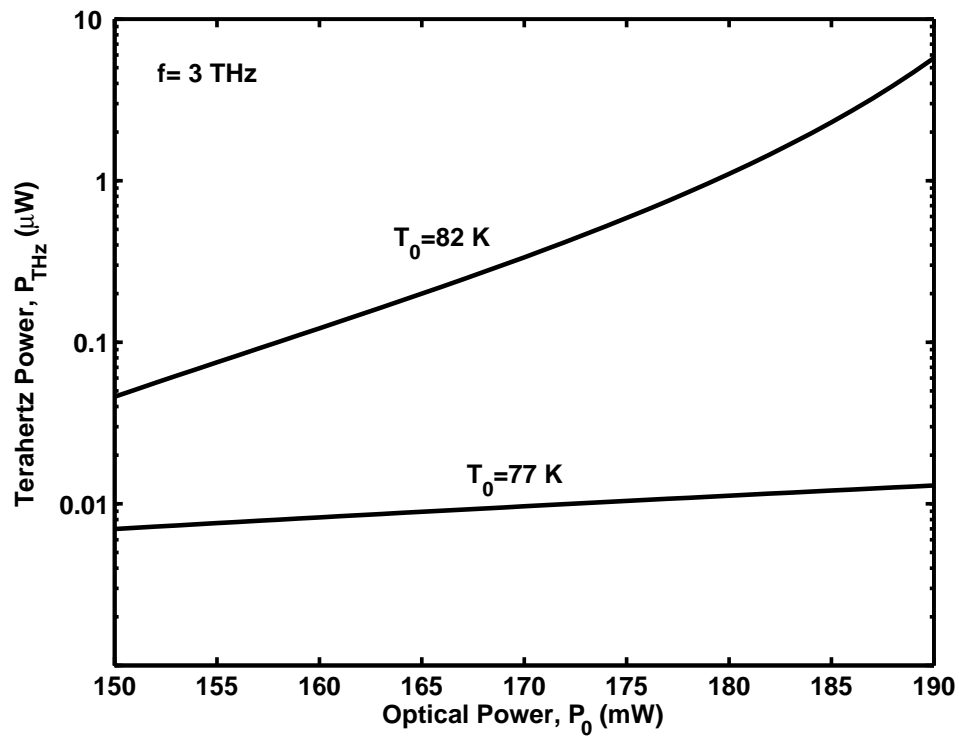


Figure 3.12: Generated terahertz power inside the YBCO film versus total incident optical power at two different bath temperatures. The applied dc bias is 23.8 mA

Chapter 4

Photomixing in Photoconductors

4.1 Introduction

In a photoconductive continuous-wave terahertz photomixer, the incident optical power density from two interfering laser beams excites the electrons from valence band to conduction band and generates spatiotemporal electron and hole concentration gratings. In the presence of a dc voltage bias, the electron and hole densities generate a current that contains a beat frequency harmonic in its spectrum. One can solve the continuity equations for the electron and hole densities along with the appropriate boundary conditions to find the resulting photocurrent.

Low-temperature grown (LTG) GaAs has been predominantly used in terahertz photoconductive photomixers. LTG-GaAs was discovered at Lincoln Lab by A. R. Cawala in the mid 1980's and has been used in variety of electronic and optoelectronic devices and systems since then. LTG GaAs is deposited by molecular beam epitaxy (MBE) at low substrate temperature ~ 200 °C in an As-rich environment and then is annealed under an As overpressure at higher temperature

~ 600 °C for about 10 minutes. A typical run includes a growth rate of $1 \mu\text{m/h}$ on a (001)-oriented GaAs substrate with an As_4/Ga beam equivalent pressure ratio of 10 [182]. In LTG-GaAs growing process, because of the low substrate temperature and the As-rich growth conditions, about 1% excess As is incorporated into the LTG-GaAs lattice. The excess As atoms result in formation of different types of point defects such as As antisites (As_{Ga} : Ga atom located on an As site in the crystal lattice, or As atom located on a Ga site), As interstitials, and Ga-related vacancies (V_{Ga}) [182]. Unannealed LTG-GaAs is relatively conducting material ($\rho \sim 10 \Omega \text{ cm}$), while annealed LTG-GaAs is a semi-insulating material ($\rho \sim 10^7 \Omega \text{ cm}$); a property which along with its relatively high carrier mobility ($\mu_n \sim 200 \text{ cm}^2/\text{Vs}$) and sub-picosecond carrier lifetime characteristics make it an ideal material for high speed photoconductive switching applications.

When LTG-GaAs is annealed, the concentration of point defects reduces and As precipitates in the form of As clusters appear [183]. The large excess As concentration in LTG-GaAs results in a large trap density, that consequently results in a high resistivity, large breakdown field ($\sim 50 \text{ V}/\mu\text{m}$), and extremely short carrier lifetime ($\sim 0.2 \text{ ps}$). The carrier lifetime of the LTG-GaAs can be controlled by the annealing and growth conditions [184]- [189]. Because of its unique properties, LTG-GaAs has been used as terahertz sources and detectors, ultra-fast and high-voltage photoconductive switches, buffer layer that eliminates sidegating and backgating in GaAs integrated circuits, and high-responsivity, wide-bandwidth photodetectors.

In this chapter, a dc biased photoconducting film excited by two CW laser beams is considered as a typical photomixing scheme. The analytical expression for the photocurrent in all directions inside the photoconductor is derived, and its dependency on the applied electric field, material and laser parameters, and photomixer configuration is explored. The saturation behavior of the photocurrent along with

its super-linear variation with the applied electric field is studied in detail. It is shown that the amplitude and the phase of the photocurrent change with the angle between the two laser beams, which can be used to develop a photomixer based phased array antenna.

4.2 Modeling of Photoconductive Photomixers

Fig. 4.1 shows a typical heterodyne photomixing scheme, in which two linearly polarized laser beams with a difference in their central frequencies falling in the terahertz spectrum are applied to a dc biased photoconductor film.

The optical power density inside the photoconductor film can be written as

$$I(\mathbf{r}, t) = I_0 T(\theta) [1 + \eta \cos(\Omega t - \mathbf{K} \cdot \mathbf{r})] e^{\alpha z} \quad (4.1)$$

where I_0 is the total optical power density of the two lasers, $T(\theta)$ is the optical power density transmission coefficient at the photoconductor-air interface, θ is the angle between the two incident laser beams, α is the absorption coefficient, and $0 < \eta \leq 1$ is the modulation index or grating contrast. As it can be seen from Eq. (4.1), the absorbed optical power density has a spatiotemporal distribution inside the photoconductor film, and hence generates a spatiotemporal electron-hole concentration inside the film.

The continuity equations for the electron and hole densities, $N(\mathbf{r}, t)$ and $P(\mathbf{r}, t)$, are [190]

$$\frac{\partial N(\mathbf{r}, t)}{\partial t} = \frac{1}{e} \nabla \cdot \mathbf{J}_n(\mathbf{r}, t) + G(\mathbf{r}, t) - R_n(\mathbf{r}, t) \quad (4.2)$$

$$\frac{\partial P(\mathbf{r}, t)}{\partial t} = -\frac{1}{e} \nabla \cdot \mathbf{J}_p(\mathbf{r}, t) + G(\mathbf{r}, t) - R_p(\mathbf{r}, t) \quad (4.3)$$

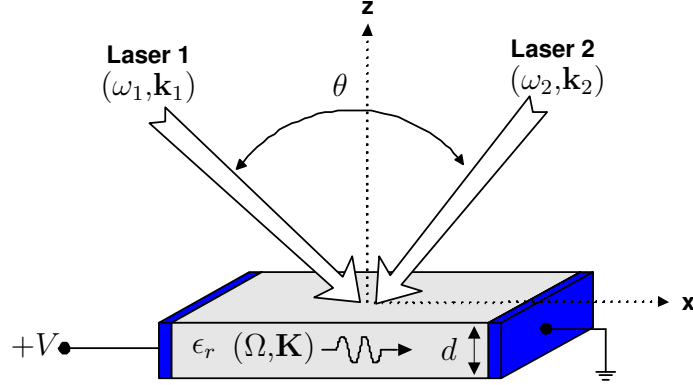


Figure 4.1: A typical photoconductive photomixer scheme.

where e is the electron charge, $G(\mathbf{r}, t)$ is the carrier generation rate, $\mathbf{J}_n(\mathbf{r}, t)$ and $\mathbf{J}_p(\mathbf{r}, t)$ are the electron and hole current densities, and $R_n(\mathbf{r}, t)$ and $R_p(\mathbf{r}, t)$ are the electron and hole recombination rates, respectively. The generation rate can be written in terms of the absorbed intensity $I(\mathbf{r}, t)$ as

$$G(\mathbf{r}, t) = \frac{\alpha}{\hbar\omega} I(\mathbf{r}, t) = G_0 [1 + \eta \cos(\Omega t - \mathbf{K} \cdot \mathbf{r})] e^{\alpha z} \quad (4.4)$$

where \hbar is the reduced Planck constant, ω is the average of the angular frequencies of the two laser beams, and $G_0 = \alpha T I_0 / \hbar\omega$. For the laser excitation with the intensity around $1 \text{ mW}/\mu\text{m}^2$, the dominant recombination mechanism is the trap assisted recombination process [191]. Therefore, the recombination rates can be approximated by [192]

$$R_n(\mathbf{r}, t) = \frac{1}{\tau_n} N(\mathbf{r}, t) \quad (4.5)$$

$$R_p(\mathbf{r}, t) = \frac{1}{\tau_p} P(\mathbf{r}, t) \quad (4.6)$$

where τ_n and τ_p are the electron and hole recombination lifetimes, respectively.

The carrier current densities $\mathbf{J}_n(\mathbf{r}, t)$ and $\mathbf{J}_p(\mathbf{r}, t)$ are the sum of the drift and diffusion currents

$$\mathbf{J}_n(\mathbf{r}, t) = eN(\mathbf{r}, t)\mathbf{v}_n(\mathbf{r}, t) + eD_n\nabla N(\mathbf{r}, t) \quad (4.7)$$

$$\mathbf{J}_p(\mathbf{r}, t) = eP(\mathbf{r}, t)\mathbf{v}_p(\mathbf{r}, t) - eD_p\nabla P(\mathbf{r}, t) \quad (4.8)$$

where \mathbf{v}_n and \mathbf{v}_p are the electron and hole drift velocities, and D_n and D_p are the electron and hole diffusion coefficients, respectively.

Generally, the carrier drift velocity and the carrier lifetime are functions of applied electric field [193]- [197]. Although our analysis is general, the simulation results are concentrated on LTG-GaAs based photomixers. An analytic expression for the carrier drift velocity in GaAs in terms of the electric field can be written as [198]

$$\mathbf{v}_n = \frac{\mu_{n0} + v_{sn}(E_0^3/E_c^4)}{1 + (E_0/E_c)^4}\mathbf{E}(\mathbf{r}, t) = \mu_n(E_0)\mathbf{E}(\mathbf{r}, t) \quad (4.9)$$

$$\mathbf{v}_p = \frac{\mu_{p0} + v_{sp}(E_0^3/E_c^4)}{1 + (E_0/E_c)^4}\mathbf{E}(\mathbf{r}, t) = \mu_p(E_0)\mathbf{E}(\mathbf{r}, t) \quad (4.10)$$

where $\mathbf{E}(\mathbf{r}, t) = \mathbf{E}_0 + \mathcal{E}(\mathbf{r}, t)$ is the total electric field inside the photoconductor, $E_c = 1.7 \text{ V}/\mu\text{m}$ is a fitting parameter to fit Eq. (4.9) to the experimental results given by Sun *et al.* for carrier velocity in LTG-GaAs [199], v_{sn} and v_{sp} are the electron and hole saturation velocities, μ_{n0} and μ_{p0} are the low field electron and hole mobilities, and $\mu_n(E_0)$ and $\mu_p(E_0)$ are the field dependent electron and hole mobilities, respectively. In Eqs. (4.9) and (4.10) we assume that the amplitude of the induced electric field, $\mathcal{E}(\mathbf{r}, t)$, is much smaller than the amplitude of the applied electric field E_0 . This is a reasonable assumption, since the induced electric field is the result of the electron and hole local separation mechanism, which is a weak

phenomena. The applied electric field is a constant vector along the direction of the applied dc bias, and its amplitude can be calculated by dividing the amplitude of the applied voltage to the length of the photoconducting film. We also use $\mu_n(E_0)$ and $\mu_p(E_0)$ from Eqs. (4.9) and (4.10) to calculate carrier diffusion coefficients, D_n and D_p , from Einstein relationship [190].

The expression for the carrier lifetime in LTG-GaAs in terms of the applied electric field can be written as [200]

$$\tau(E_0) = \tau(E_0 = 0) \times (T_e/T)^{1.5} \times \left[r(E_0 = 0)/r(E_0) \right]^3 \quad (4.11)$$

where T is the lattice temperature, T_e is the electron temperature, and r is the radius of the well in the direction of the applied field.

The total electric field, $\mathbf{E}(\mathbf{r}, t)$, is related to the electron and hole densities by Poisson's equation

$$\nabla \cdot \mathbf{E}(\mathbf{r}, t) = \frac{e}{\epsilon} [P(\mathbf{r}, t) - N(\mathbf{r}, t)] \quad (4.12)$$

where ϵ is the permittivity of the photoconductor.

From Eqs. (4.2) to (4.12), one can extract a set of nonlinear coupled partial differential equations given by Eqs. (4.13) and (4.14). Two nonlinear terms are the first and the second terms in the right hand sides of the two equations.

$$\begin{aligned} \frac{\partial N(\mathbf{r}, t)}{\partial t} &= \mu_n(E_0) \mathbf{E}(\mathbf{r}, t) \cdot \nabla N(\mathbf{r}, t) + \mu_n(E_0) \frac{e}{\epsilon} N(\mathbf{r}, t) [P(\mathbf{r}, t) - N(\mathbf{r}, t)] \\ &\quad + D_n \nabla^2 N(\mathbf{r}, t) - \frac{1}{\tau_n} N(\mathbf{r}, t) + G(\mathbf{r}, t) \end{aligned} \quad (4.13)$$

$$\begin{aligned} \frac{\partial P(\mathbf{r}, t)}{\partial t} &= -\mu_p(E_0) \mathbf{E}(\mathbf{r}, t) \cdot \nabla P(\mathbf{r}, t) - \mu_p(E_0) \frac{e}{\epsilon} P(\mathbf{r}, t) [P(\mathbf{r}, t) - N(\mathbf{r}, t)] \\ &\quad + D_p \nabla^2 P(\mathbf{r}, t) - \frac{1}{\tau_p} P(\mathbf{r}, t) + G(\mathbf{r}, t) \end{aligned} \quad (4.14)$$

One can linearize Eqs. (4.13) and (4.14) by replacing the total electric field, $\mathbf{E}(\mathbf{r}, t)$, with the applied electric field \mathbf{E}_0 and also replacing the electron and hole densities, $N(\mathbf{r}, t)$ and $P(\mathbf{r}, t)$, in the first part of the second terms in the right hand sides of the equations (4.13) and (4.14) with their average values over the thickness of the photoconducting film.

Note that we do not replace the total electric field by the applied electric field from the beginning. We have taken into account the effect of the local electron and hole separation mechanism by incorporating Eq. (4.12).

Applying the above mentioned simplifying assumptions to Eqs. (4.13) and (4.14) results in a set of linear coupled partial differential equations for the electron and hole densities as

$$\frac{\partial N}{\partial t} = \mu_n \mathbf{E}_0 \cdot \nabla N + \mu_n \frac{e}{\epsilon} \bar{N}_0 [P - N] + D_n \nabla^2 N - \frac{N}{\tau_n} + G \quad (4.15)$$

$$\frac{\partial P}{\partial t} = -\mu_p \mathbf{E}_0 \cdot \nabla P - \mu_p \frac{e}{\epsilon} \bar{P}_0 [P - N] + D_p \nabla^2 P - \frac{P}{\tau_p} + G \quad (4.16)$$

where

$$\bar{N}_0[\bar{P}_0] = \frac{1}{\alpha d} (1 - e^{-\alpha d}) N_0[P_0] \quad (4.17)$$

in which N_0 and P_0 are the solutions to Eqs. (4.15) and (4.16) associated with the time independent term of the generation rate function given by Eq. (4.4).

Equations (4.15) and (4.16) are two coupled non-homogeneous parabolic partial differential equations, which are difficult to solve for a complete set of solutions. Since we are interested in the solution at the steady state, we use the non-homogeneous ordinary differential equation method to find the solution to these equations [201].

One can rewrite Eq. (4.4) as

$$G(\mathbf{r}, t) = G_0 e^{\alpha z} + \delta G(\mathbf{r}, t) e^{\alpha z} \quad (4.18)$$

where

$$\delta G(\mathbf{r}, t) = \Re e\{\eta G_0 e^{j(\Omega t - \mathbf{K} \cdot \mathbf{r})}\} \quad (4.19)$$

Hence the particular solution for Eqs. (4.15) and (4.16) can be written as

$$N^p(\mathbf{r}, t) = N_0 e^{\alpha z} + \delta N(\mathbf{r}, t) e^{\alpha z} \quad (4.20)$$

$$P^p(\mathbf{r}, t) = P_0 e^{\alpha z} + \delta P(\mathbf{r}, t) e^{\alpha z} \quad (4.21)$$

where

$$\delta N(\mathbf{r}, t) = \Re e\{\delta \hat{N} e^{j(\Omega t - \mathbf{K} \cdot \mathbf{r})}\} \quad (4.22)$$

$$\delta P(\mathbf{r}, t) = \Re e\{\delta \hat{P} e^{j(\Omega t - \mathbf{K} \cdot \mathbf{r})}\} \quad (4.23)$$

Substituting Eqs. (4.18) to (4.23) into Eqs. (4.15) and (4.16) results in the following equations for N_0 and P_0

$$\mu_n \frac{e}{\epsilon} \bar{N}_0 [P_0 - N_0] + \alpha^2 D_n N_0 - \frac{N_0}{\tau_n} + G_0 = 0 \quad (4.24)$$

$$-\mu_p \frac{e}{\epsilon} \bar{P}_0 [P_0 - N_0] + \alpha^2 D_p P_0 - \frac{P_0}{\tau_p} + G_0 = 0 \quad (4.25)$$

A solution for Eqs. (4.24) and (4.25) is given in Appendix A.

The resulting equations for $\delta \hat{N}$ and $\delta \hat{P}$ are

$$\begin{aligned} & \left[D_n (|\mathbf{K}|^2 - \alpha^2) + \frac{e}{\epsilon} \mu_n \bar{N}_0 + \tau_n^{-1} + j \mu_n (\mathbf{E}_0 \cdot \mathbf{K}) + 2j \alpha D_n K_z + j \Omega \right] \delta \hat{N} \\ & - \left[\frac{e}{\epsilon} \mu_n \bar{N}_0 \right] \delta \hat{P} = \eta G_0 \end{aligned} \quad (4.26)$$

$$\begin{aligned} & \left[D_p (|\mathbf{K}|^2 - \alpha^2) + \frac{e}{\epsilon} \mu_p \bar{P}_0 + \tau_p^{-1} - j \mu_p (\mathbf{E}_0 \cdot \mathbf{K}) + 2j \alpha D_p K_z + j \Omega \right] \delta \hat{P} \\ & - \left[\frac{e}{\epsilon} \mu_p \bar{P}_0 \right] \delta \hat{N} = \eta G_0 \end{aligned} \quad (4.27)$$

One can solve Eqs. (4.26) and (4.27) to find $\delta\hat{N}$ and $\delta\hat{P}$ as

$$\delta\hat{N} = |\delta\hat{N}|e^{j\phi_n} = \frac{a_n + jb_n}{a + jb}\eta G_0 \approx \frac{\tau_n}{1 + j\Omega\tau_n}\eta G_0 \quad (4.28)$$

$$\delta\hat{P} = |\delta\hat{P}|e^{j\phi_p} = \frac{a_p + jb_p}{a + jb}\eta G_0 \approx \frac{\tau_p}{1 + j\Omega\tau_p}\eta G_0 \quad (4.29)$$

where

$$a_n = \tau_p^{-1} + D_p(|\mathbf{K}|^2 - \alpha^2) + \frac{e}{\epsilon}(\mu_n\bar{N}_0 + \mu_p\bar{P}_0) \approx \frac{1}{\tau_n} \quad (4.30)$$

$$a_p = \tau_n^{-1} + D_n(|\mathbf{K}|^2 - \alpha^2) + \frac{e}{\epsilon}(\mu_n\bar{N}_0 + \mu_p\bar{P}_0) \approx \frac{1}{\tau_p} \quad (4.31)$$

$$b_n = \Omega - \mu_p(\mathbf{E}_0 \cdot \mathbf{K}) + 2\alpha D_p K_z \approx \Omega \quad (4.32)$$

$$b_p = \Omega + \mu_n(\mathbf{E}_0 \cdot \mathbf{K}) + 2\alpha D_n K_z \approx \Omega \quad (4.33)$$

$$a = a_n a_p - b_n b_p - \frac{e}{\epsilon}[\mu_p a_n \bar{P}_0 + \mu_n a_p \bar{N}_0] \approx \frac{1}{\tau_n \tau_p} - \Omega^2 \quad (4.34)$$

$$b = a_p b_n + a_n b_p - \frac{e}{\epsilon}[\mu_p b_n \bar{P}_0 + \mu_n b_p \bar{N}_0] \approx \Omega\left(\frac{1}{\tau_n} + \frac{1}{\tau_p}\right) \quad (4.35)$$

The homogeneous solution to Eqs. (4.15) and (4.16) at the steady state is the solution to the following coupled homogenous partial differential equations

$$\mu_n \mathbf{E}_0 \cdot \nabla N^h + \mu_n \frac{e}{\epsilon} \bar{N}_0 [P^h - N^h] + D_n \nabla^2 N^h - \frac{N^h}{\tau_n} = 0 \quad (4.36)$$

$$-\mu_p \mathbf{E}_0 \cdot \nabla P^h - \mu_p \frac{e}{\epsilon} \bar{P}_0 [P^h - N^h] + D_p \nabla^2 P^h - \frac{P^h}{\tau_p} = 0 \quad (4.37)$$

Eqs. (4.36) and (4.37) can be combined into a single partial differential equation as

$$\mu_n \mu_p \mathbf{E}_0 \cdot [P^h \nabla N^h - N^h \nabla P^h] + [\mu_p D_n P^h \nabla^2 N^h + \mu_n D_p N^h \nabla^2 P^h] - \left(\frac{\mu_p}{\tau_n} + \frac{\mu_n}{\tau_p}\right) N^h P^h = 0 \quad (4.38)$$

One can consider a solution set for Eq. (4.38) as

$$N^h(z) = N_1 e^{L^{-1}z} \quad (4.39)$$

$$P^h(z) = P_1 e^{L^{-1}z} \quad (4.40)$$

where N_1 and P_1 are two constants that can be determined by applying the appropriate surface recombination boundary conditions. The parameter L in Eqs. (4.39) and (4.40) is the effective diffusion length that can be found by substituting Eqs. (4.39) and (4.40) into Eq. (4.38)

$$L = \sqrt{D\tau} \quad (4.41)$$

$$D = \frac{\mu_p D_n + \mu_n D_p}{\mu_n + \mu_p} \quad (4.42)$$

$$\tau = \frac{\mu_n + \mu_p}{\frac{\mu_p}{\tau_n} + \frac{\mu_n}{\tau_p}} \quad (4.43)$$

Knowing the particular and the general solutions to Eqs. (4.15) and (4.16), one can write the complete solution as

$$N(\mathbf{r}, t) = N^p(\mathbf{r}, t) + N^h(z) = [N_0 + \delta N(\mathbf{r}, t)] e^{\alpha z} + N_1 e^{L^{-1}z} \quad (4.44)$$

$$P(\mathbf{r}, t) = P^p(\mathbf{r}, t) + P^h(z) = [P_0 + \delta P(\mathbf{r}, t)] e^{\alpha z} + P_1 e^{L^{-1}z} \quad (4.45)$$

The surface recombination boundary condition can be written as [190], [191]

$$D_n \frac{\partial N}{\partial z} \Big|_{z=0} = -s_n N \Big|_{z=0} \quad (4.46)$$

$$D_p \frac{\partial P}{\partial z} \Big|_{z=0} = -s_p P \Big|_{z=0} \quad (4.47)$$

where s_n and s_p are the electron and hole surface recombination velocities, respectively. Applying Eqs. (4.46) and (4.47) to Eqs. (4.44) and (4.45) yields

$$N_1 = -\frac{s_n + \alpha D_n}{s_n + L^{-1}D_n} N_0 \quad (4.48)$$

$$P_1 = -\frac{s_p + \alpha D_p}{s_p + L^{-1}D_p} P_0 \quad (4.49)$$

The total electron and hole densities can be written as

$$N(\mathbf{r}, t) = N_0 \left[e^{\alpha z} - \frac{s_n + \alpha D_n}{s_n + L^{-1}D_n} e^{L^{-1}z} \right] + |\delta \hat{N}| \cos(\Omega t - \mathbf{K} \cdot \mathbf{r} + \phi_n) e^{\alpha z} \quad (4.50)$$

$$P(\mathbf{r}, t) = P_0 \left[e^{\alpha z} - \frac{s_p + \alpha D_p}{s_p + L^{-1}D_p} e^{L^{-1}z} \right] + |\delta \hat{P}| \cos(\Omega t - \mathbf{K} \cdot \mathbf{r} + \phi_p) e^{\alpha z} \quad (4.51)$$

Using Eqs. (4.7) to (4.10) along with the electron and hole densities given by Eqs. (4.50) and (4.51) results in the expression for the photocurrent inside the photoconductor as

$$J_x(\mathbf{r}, t) = J_{x0} + J_{x1} \cos(\Omega t - \mathbf{K} \cdot \mathbf{r}) + J_{x2} \sin(\Omega t - \mathbf{K} \cdot \mathbf{r}) \quad (4.52)$$

$$J_y(\mathbf{r}, t) = J_{y1} \cos(\Omega t - \mathbf{K} \cdot \mathbf{r}) + J_{y2} \sin(\Omega t - \mathbf{K} \cdot \mathbf{r}) \quad (4.53)$$

$$J_z(\mathbf{r}, t) = J_{z0} + J_{z1} \cos(\Omega t - \mathbf{K} \cdot \mathbf{r}) + J_{z2} \sin(\Omega t - \mathbf{K} \cdot \mathbf{r}) \quad (4.54)$$

where J_x , J_y , and J_z are the photocurrent components in the x , y , and z directions, respectively, and

$$J_{x0} = e(v_n N_0 + v_p P_0) e^{\alpha z} + e(v_n N_1 + v_p P_1) e^{L^{-1}z} \quad (4.55)$$

$$J_{x1} = e \left[v_n |\delta \hat{N}| \cos \phi_n + v_p |\delta \hat{P}| \cos \phi_p + D_n K_x |\delta \hat{N}| \sin \phi_n - D_p K_x |\delta \hat{P}| \sin \phi_p \right] e^{\alpha z} \quad (4.56)$$

$$J_{x2} = e \left[-v_n |\delta \hat{N}| \sin \phi_n - v_p |\delta \hat{P}| \sin \phi_p + D_n K_x |\delta \hat{N}| \cos \phi_n - D_p K_x |\delta \hat{P}| \cos \phi_p \right] e^{\alpha z} \quad (4.57)$$

$$J_{y1} = e K_y \left[D_n |\delta \hat{N}| \sin \phi_n - D_p |\delta \hat{P}| \sin \phi_p \right] e^{\alpha z} \quad (4.58)$$

$$J_{y2} = e K_y \left[D_n |\delta \hat{N}| \cos \phi_n - D_p |\delta \hat{P}| \cos \phi_p \right] e^{\alpha z} \quad (4.59)$$

$$J_{z0} = e \alpha (D_n N_0 - D_p P_0) e^{\alpha z} + e L^{-1} (D_n N_1 - D_p P_1) e^{L^{-1} z} \quad (4.60)$$

$$J_{z1} = e \left[\alpha D_n |\delta \hat{N}| \cos \phi_n - \alpha D_p |\delta \hat{P}| \cos \phi_p + K_z D_n |\delta \hat{N}| \sin \phi_n - K_z D_p |\delta \hat{P}| \sin \phi_p \right] e^{\alpha z} \quad (4.61)$$

$$J_{z2} = e \left[-\alpha D_n |\delta \hat{N}| \sin \phi_n + \alpha D_p |\delta \hat{P}| \sin \phi_p + K_z D_n |\delta \hat{N}| \cos \phi_n - K_z D_p |\delta \hat{P}| \cos \phi_p \right] e^{\alpha z} \quad (4.62)$$

where $v_n = \mu_n E_0$ and $v_p = \mu_p E_0$ are the electron and hole drift velocities, respectively, and $\mathbf{E}_0 = E_0 \hat{x}$. As it can be seen from Eqs. (4.55) to (4.62), the photocurrent components in the lateral and transversal directions are only diffusion currents, while the longitudinal photocurrent contains both diffusion and drift components. Hence, the longitudinal component is much greater than the two other components.

For the case where the two laser beams are normally incident the photoconductor surface and for $\tau_n \approx \tau_p$, the longitudinal component of the photocurrent given by Eq. (4.52) can be approximately written as

$$J_x(z, t) \approx T \alpha I_0 \frac{e}{\hbar \omega} \left[(\tau_n v_n + \tau_p v_p) + \left(\frac{\tau_n v_n}{[1 + (\Omega \tau_n)^2]^{1/2}} + \frac{\tau_p v_p}{[1 + (\Omega \tau_p)^2]^{1/2}} \right) \eta \cos(\Omega t - K_z z - \phi) \right] e^{\alpha z} \quad (4.63)$$

which has the same form as the photocurrent expression given by E. R. Brown [62]. The equivalent surface current density can be calculated by integrating the volume current density over the thickness of the photoconducting film. The longitudinal component of the surface current density is a traveling-wave current given by

$$J_s(\boldsymbol{\rho}, t) = J_{dc}^s + \Re e\{\tilde{J}_s e^{j\Omega t}\} \quad (4.64)$$

where

$$J_{dc}^s = ed[v_n(\bar{N}_0 + \bar{N}_1) + v_p(\bar{P}_0 + \bar{P}_1)] \quad (4.65)$$

$$\tilde{J}_s = [J_{s1}^2 + J_{s2}^2]^{1/2} e^{-j\phi} e^{-j\mathbf{K}\cdot\boldsymbol{\rho}} \quad (4.66)$$

$$J_{s1} = \frac{e}{\alpha^2 + K_z^2} \left[(\alpha_1^n v_n - D_n \alpha_2^n K_x) |\delta \hat{N}| + (\alpha_1^p v_p + D_p \alpha_2^p K_x) |\delta \hat{P}| \right] \quad (4.67)$$

$$J_{s2} = \frac{e}{\alpha^2 + K_z^2} \left[(\alpha_2^n v_n + D_n \alpha_1^n K_x) |\delta \hat{N}| + (\alpha_2^p v_p - D_p \alpha_1^p K_x) |\delta \hat{P}| \right] \quad (4.68)$$

$$\phi = \tan^{-1} \frac{J_{s2}}{J_{s1}} \quad (4.69)$$

in which

$$\bar{N}_1[\bar{P}_1] = \frac{1}{L^{-1}d} (1 - e^{-L^{-1}d}) N_1[P_1] \quad (4.70)$$

$$\alpha_1^{n[p]} = \alpha_1 \cos \phi_{n[p]} + \alpha_2 \sin \phi_{n[p]} \quad (4.71)$$

$$\alpha_2^{n[p]} = \alpha_2 \cos \phi_{n[p]} - \alpha_1 \sin \phi_{n[p]} \quad (4.72)$$

$$\alpha_1 = \alpha + K_z e^{-\alpha d} \sin K_z d - \alpha e^{-\alpha d} \cos K_z d \quad (4.73)$$

$$\alpha_2 = -K_z + K_z e^{-\alpha d} \cos K_z d + \alpha e^{-\alpha d} \sin K_z d \quad (4.74)$$

In Eq. (4.66), $\boldsymbol{\rho}$ is the position vector in the $x - y$ plane.

The amplitude of the terahertz photocurrent given by Eq. (4.64) is related to the

photoconductor's physical parameters as well as to the photomixer's structure by Eqs. (4.28) to (4.35) and Eqs. (4.67) to (4.74). It can be seen that the amplitude of the terahertz photocurrent is not only related to the carrier lifetime and the beat frequency, but also is a function of the other parameters of the photoconductor material and the photomixer structure.

In the next section, the effects of the different physical parameters as well as the configuration of the photomixer on the generated photocurrent are studied. In this analysis we neglect the electric field screening effect inside the photoconductor film.

4.3 Simulation Results for a Photomixer made of LTG-GaAs

The physical parameters of a typical photomixer made of LTG-GaAs are given in Table 4.1. The total photocurrent given by Eq. (4.64) contains two components; the dc component, J_{dc}^s , and the terahertz component, \tilde{J}_s . The dc component of the photocurrent, which is given by Eq. (4.65), is proportional to the carrier drift velocities, v_n and v_p , and the carrier lifetimes, τ_n and τ_p , and has no contribution in terahertz signal generation process. The dc component of the photocurrent limits the maximum sustainable dc bias and optical power before device failure, and hence limits the available terahertz signal.

The amplitude of the terahertz photocurrent, which is given by Eqs. (4.66) to (4.68), is proportional to the carrier drift velocities and the carrier densities, and also is a function of the geometry of the photomixer and the other physical parameters of the photoconductor. Note that the terahertz photocurrent is related to the applied electric field via carrier drift velocities and carrier lifetimes.

Table 4.1: Physical parameters of a photomixer made of LTG-GaAs

Description	Notation	Value
Work temperature	T_0	300 K
Absorption coefficient at $\lambda = 780$ nm [190]	α	10000 cm^{-1}
Photoconductor thickness	d	$2 \text{ }\mu\text{m}$
Photoconductor length	l	$10 \text{ }\mu\text{m}$
Angle between the two laser beams	θ	10°
Laser central wavelength	λ	780 nm
Laser intensity	I_0	$0.4 \text{ mW}/\mu\text{m}^2$
Electron saturation velocity [73]	v_{sn}	$4 \times 10^4 \text{ m/s}$
Hole saturation velocity [73]	v_{sp}	$1 \times 10^4 \text{ m/s}$
Low field electron lifetime [73]	τ_{n0}	0.1 ps
Low field hole lifetime [73]	τ_{p0}	0.4 ps
Low field electron mobility [41]	μ_{n0}	$400 \text{ cm}^2/\text{Vs}$
Low field hole mobility [41]	μ_{p0}	$100 \text{ cm}^2/\text{Vs}$
Surface recombination velocity [202]	$s_{n,p}$	5000 m/s
Relative permittivity [44]	ϵ_r	12.8

Fig. 4.2 shows variation of the electron lifetime with applied electric field in LTG-GaAs material. The graph is generated using the method given in [200]. The effective radius of the ionized donor's Colombic potential, r , is found as $r(E_0 = 0) = 1.1632 \text{ nm}$. As it is expected, the electron lifetime is almost independent of the applied electric field for the low field regime, while it increases exponentially with the rate of $\tau_n \propto E_0^{1.8}$ for high values of the applied electric field. Shown in Fig. 4.3 is amplitude of the electron density, $|\delta\hat{N}|$, versus electron lifetime for different beat frequencies. It can be seen that the electron density is proportional to the electron lifetime for small values of τ_n and becomes independent of τ_n when τ_n increases above a certain value. The linear region is bigger for the smaller values of the beat frequencies and becomes smaller at the higher beat frequencies. The electron density is related to the applied electric field via carrier lifetime. Since the electron density is independent of the carrier lifetime for high values of τ_n (see

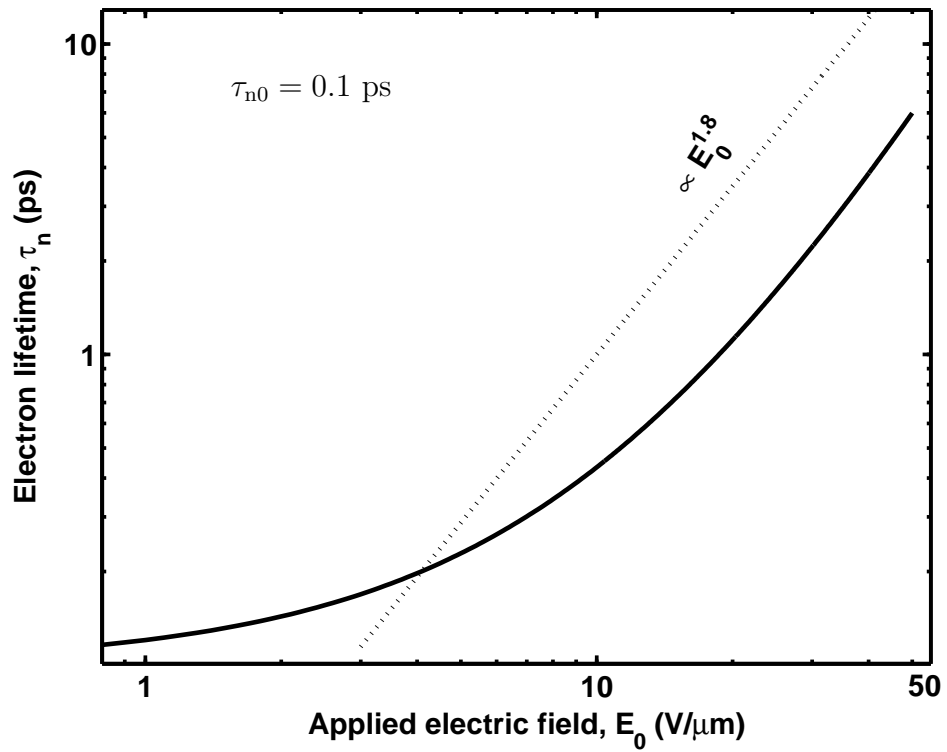


Figure 4.2: Electron lifetime versus applied electric field in LTG-GaAs. The low-field electron lifetime is $\tau_{n0} = 0.1$ ps.

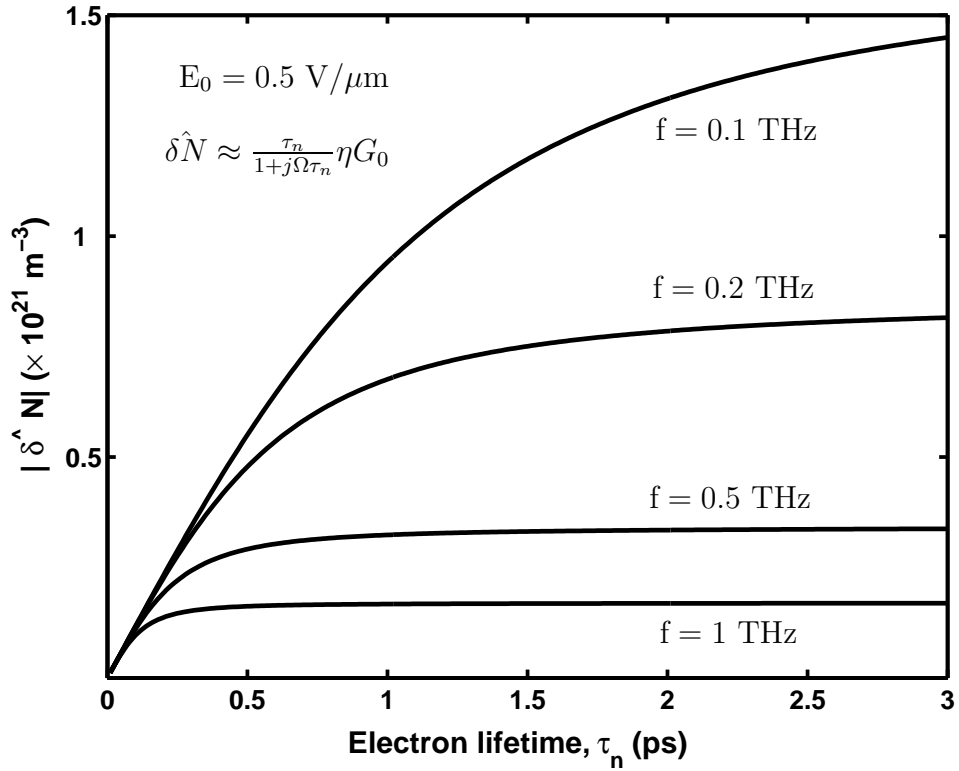


Figure 4.3: Amplitude of electron density inside the LTG-GaAs film versus electron lifetime at different beat frequencies. The total applied optical power density is $I_0 = 0.4 \text{ mW}/\mu\text{m}^2$.

Fig. 4.3), it is also independent of the applied electric field for high values of E_0 as shown in Fig. 4.4. It may worth to note that there is a small range for the applied electric field before the saturation region, for which the amplitude of the electron density increases super-linearly with E_0 , specially at low frequencies. For sufficiently high values of the applied electric field, the amplitude of the electron density is no longer proportional to the carrier life time (see Fig. 4.3) and becomes independent of it, where the saturation occurs.

Fig. 4.5 shows the dependency of the amplitude of the electron density on the frequency and electron lifetime. A small value has been chosen for the applied electric field to keep the low field electron lifetime unchanged. It can be seen from Fig. 4.5 that the amplitude of the electron density remains between the two upper and lower bounds depicted by dotted and dashed curves, respectively. For small values of τ_{n0} the electron density approaches to its lower bound, which represents $\frac{\tau_n}{[1 + (\Omega\tau_n)^2]^{1/2}}$ functionality with the electron life time and the beat frequency, while for bigger values of τ_{n0} it approaches to its upper bound, which is G_0/Ω . At high frequencies, the two upper and lower bounds merge together and the electron density becomes independent of the electron lifetime. The same scenario happens for the hole parameters.

Amplitude of the terahertz photocurrent in a typical photomixer made of LTG-GaAs is shown in Fig. 4.6. As it can be seen from Fig. 4.6, amplitude of the terahertz photocurrent saturates when the applied electric field increases above a certain value. This photocurrent saturation behavior is the direct result of the carrier drift velocity saturation phenomena in photoconductors. Recently, the form of behavior shown in Fig. 4.6 has been experimentally confirmed by Michael *et al.* for the terahertz power generated by an LTG-GaAs based photomixer [74].

According to Eqs. (4.67) and (4.68) the terahertz photocurrent can be simply mod-

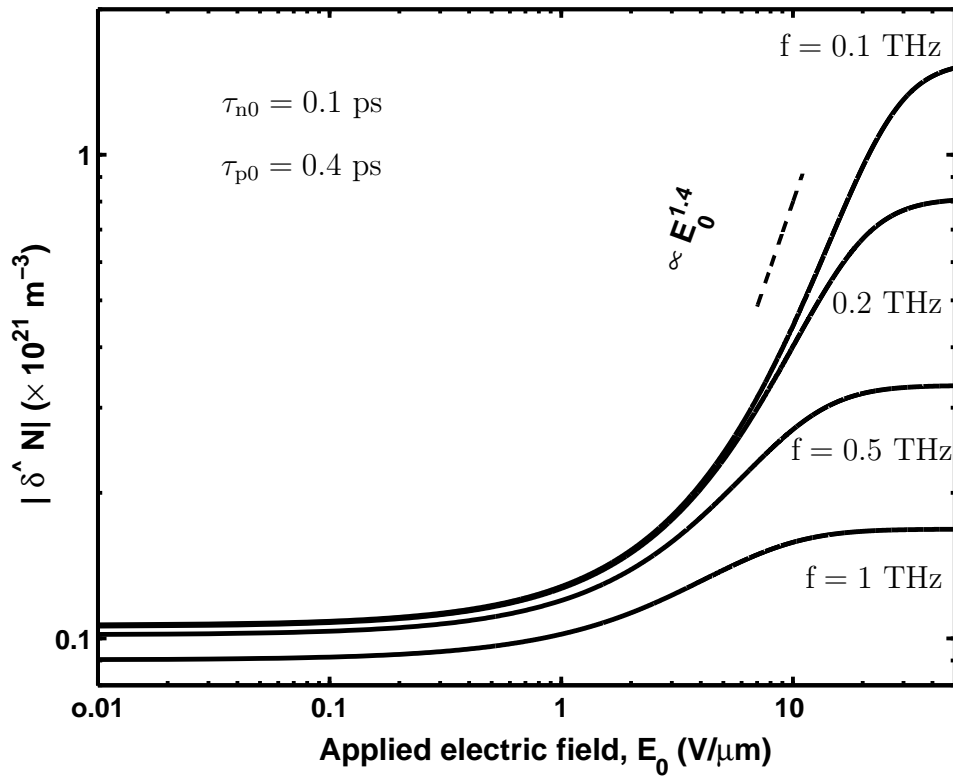


Figure 4.4: Amplitude of electron density inside the LTG-GaAs film versus applied electric field at different beat frequencies. The total applied optical power density is $I_0 = 0.4 \text{ mW}/\mu\text{m}^2$.

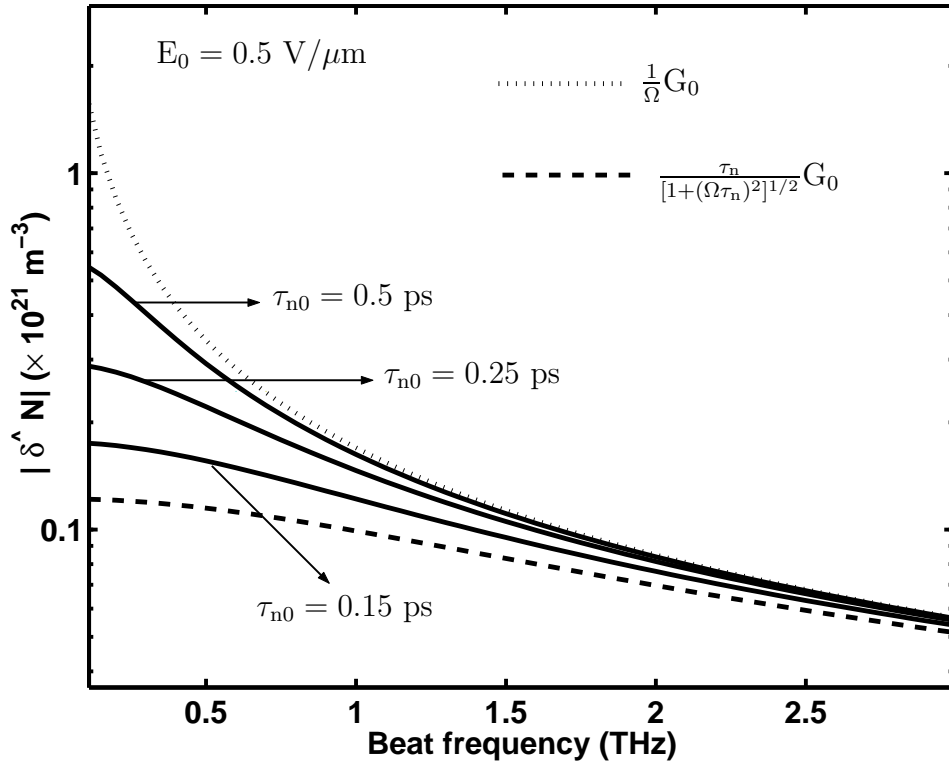


Figure 4.5: Amplitude of electron density versus beat frequency for different electron lifetimes in an LTG-GaAs photomixer. The total applied optical power density is $I_0 = 0.4 \text{ mW}/\mu\text{m}^2$.

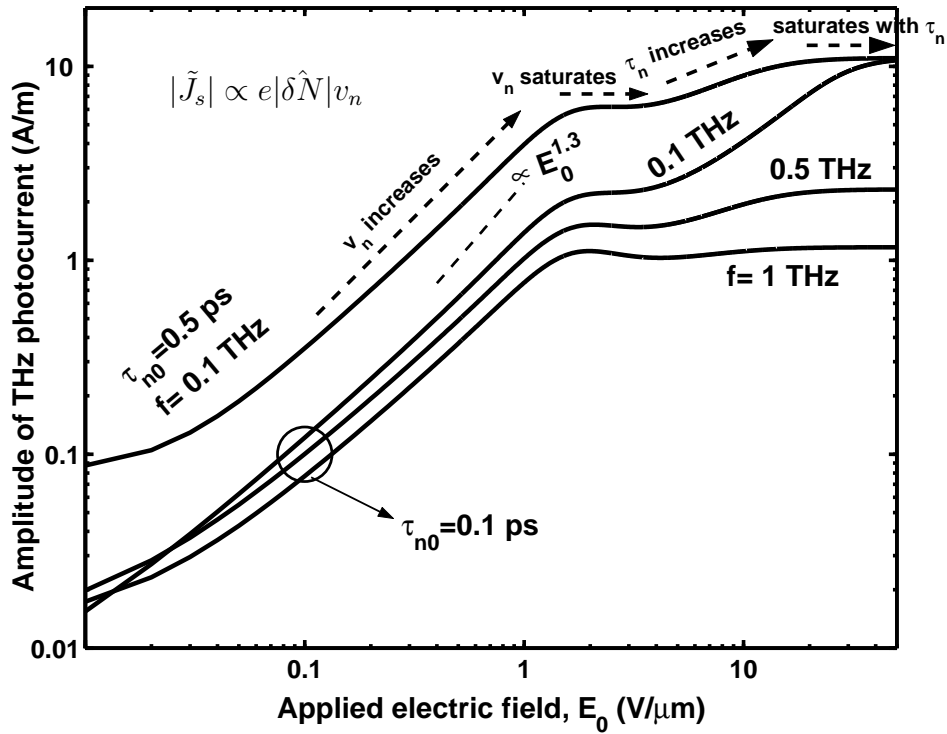


Figure 4.6: Amplitude of terahertz equivalent surface photocurrent in LTG-GaAs photomixer versus applied electric field at different beat frequencies and for two different low-field electron lifetimes. The total applied optical power density is $I_0 = 0.4 \text{ mW}/\mu\text{m}^2$.

elled as $|\tilde{J}_s| \propto e|\delta\hat{N}|v_n$. The electron drift velocity, v_n , approaches to its saturation value v_{sn} for high values of the applied electric field. The amplitude of the electron density, $|\delta\hat{N}|$ also saturates for high values of the applied electric field, hence the photocurrent saturation occurs at high values of E_0 . Note that the photocurrent saturation occurs at lower values of the applied electric field for higher frequencies. One may notice from Fig. 4.6 that the terahertz photocurrent shows a super-linear variation with the applied electric field before the saturation region; the behavior that has been experimentally shown by some authors [41], [78]. As it can be seen from Fig. 4.6, one can achieve a higher level of terahertz photocurrent by increasing the low field carrier lifetime, although increasing the carrier lifetime above 1 ps will not increase the terahertz photocurrent anymore. The carrier lifetime in an LTG-GaAs sample can be controlled by controlling its growth and annealing conditions [186].

The dc component of the generated photocurrent is one of the limiting factors of the achievable terahertz power in a terahertz photomixer [78]. Unlike the terahertz photocurrent, the dc photocurrent does not saturate with the applied electric field and also increases by increasing the carrier lifetime. Fig. 4.7 shows the amplitude of the dc photocurrent versus applied electric field for different electron lifetimes. As it can be seen from Figs. 4.6 and 4.7, there is a trade-off between the maximum sustainable dc photocurrent before the device failure and the maximum achievable terahertz signal in terms of the carrier lifetime and the applied electric field. The optimum operation condition for an LTG-GaAs photomixer is a dc bias just before the saturation region and a carrier life time around 0.5 ps.

Fig. 4.8 shows amplitude of the terahertz photocurrent versus beat frequency for different values of the electron lifetime. Comparing Fig. 4.5 with Fig. 4.8 shows that the terahertz photocurrent and the carrier density have the same form of

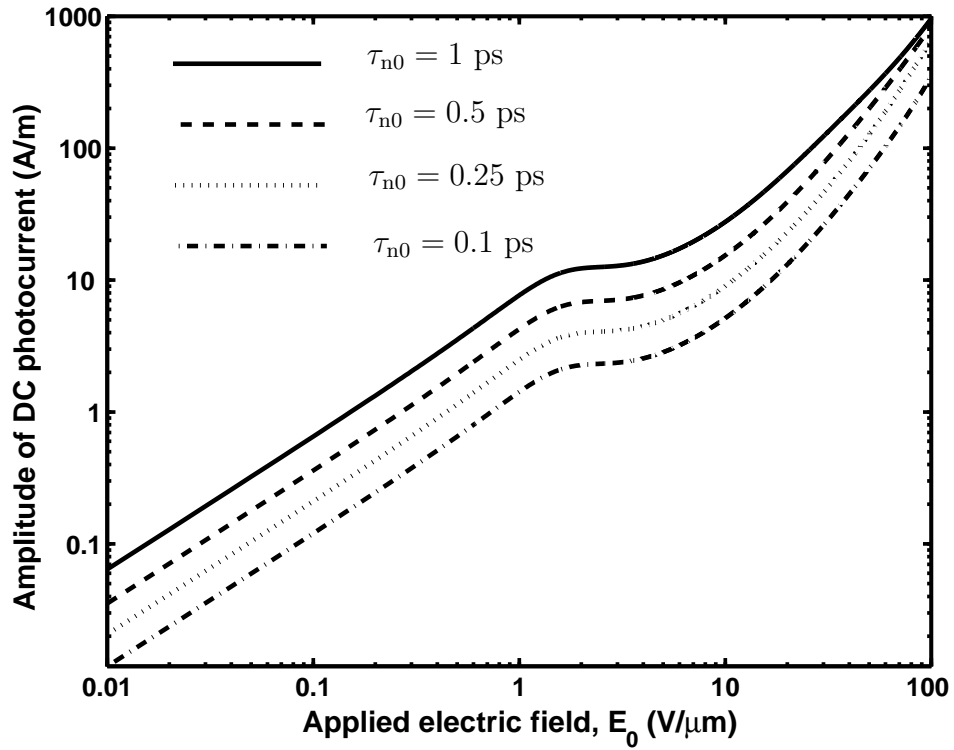


Figure 4.7: Amplitude of dc photocurrent in LTG-GaAs photomixer versus applied electric field at different low-field electron lifetimes. The total applied optical power density is $I_0 = 0.4 \text{ mW}/\mu\text{m}^2$.

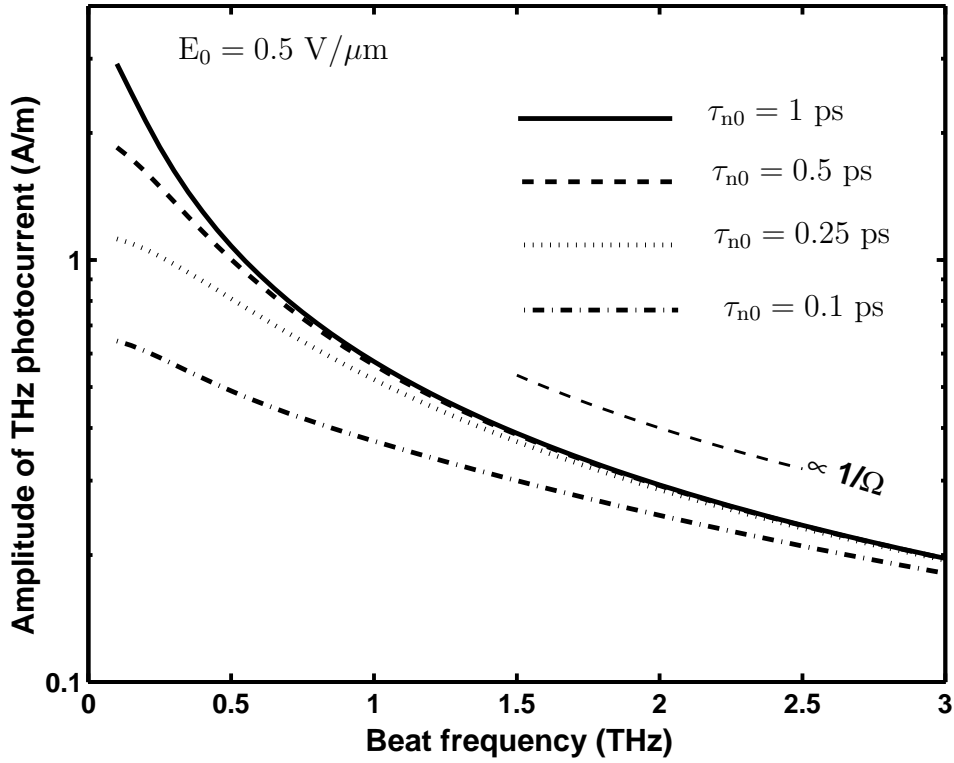


Figure 4.8: Amplitude of terahertz equivalent surface photocurrent in LTG-GaAs photomixer versus beat frequency at different low-field electron lifetimes. The total applied optical power density is $I_0 = 0.4 \text{ mW}/\mu\text{m}^2$.

dependency on the carrier lifetime. The amplitude of the terahertz photocurrent decreases by the rate of $1/\Omega$ with the beat frequency.

Fig. 4.9 shows amplitude of the terahertz photocurrent versus thickness of the photoconducting film. The amplitude of the terahertz photocurrent increases exponentially for the thicknesses smaller than the penetration depth, $1/\alpha$, since the thicker the photoconductor film the more the optical power absorption. The amplitude of the terahertz photocurrent saturates for the thicknesses beyond $2/\alpha$. Although Fig. 4.9 suggests higher thicknesses for the photoconducting film to achieve higher terahertz power, however the thicker photoconductor has smaller thermal conductivity [78], which can limit the maximum applicable optical power.

Fig. 4.10 shows variation of the longitudinal component of the grating vector, K_x , with angle between the two lasers. By changing K_x , one can control the phase distribution of the traveling-wave terahertz photocurrent (see Fig. 4.10), which can be used to design an array of the photomixer elements with beam steering capability [83].

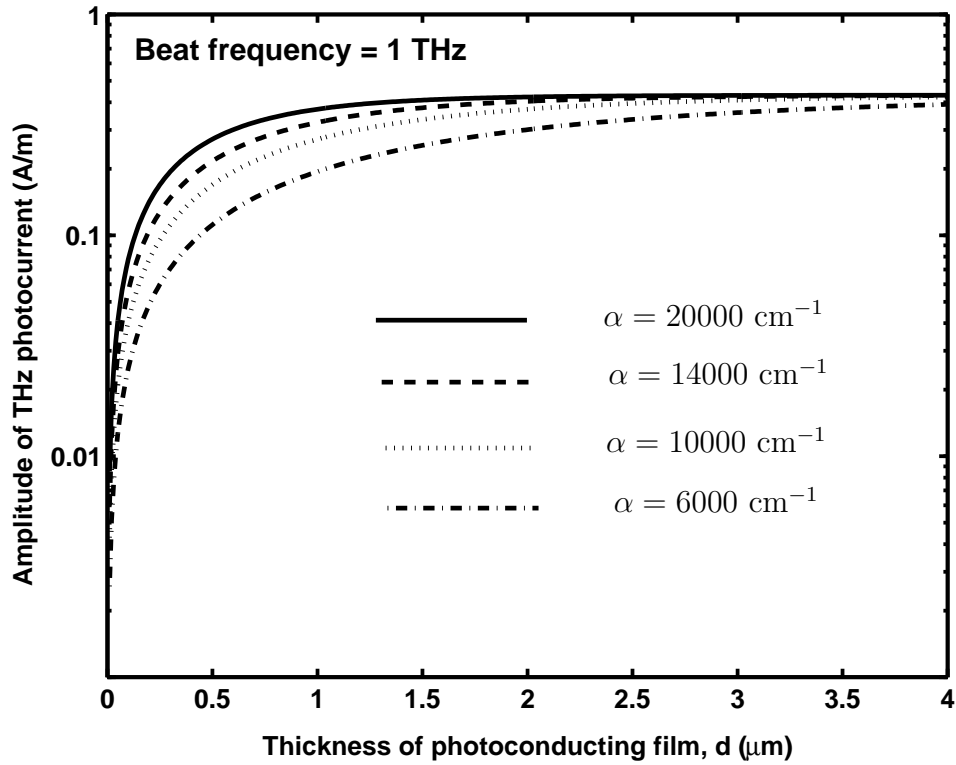


Figure 4.9: Amplitude of terahertz equivalent surface photocurrent versus thickness of the LTG-GaAs film for different absorption coefficients.

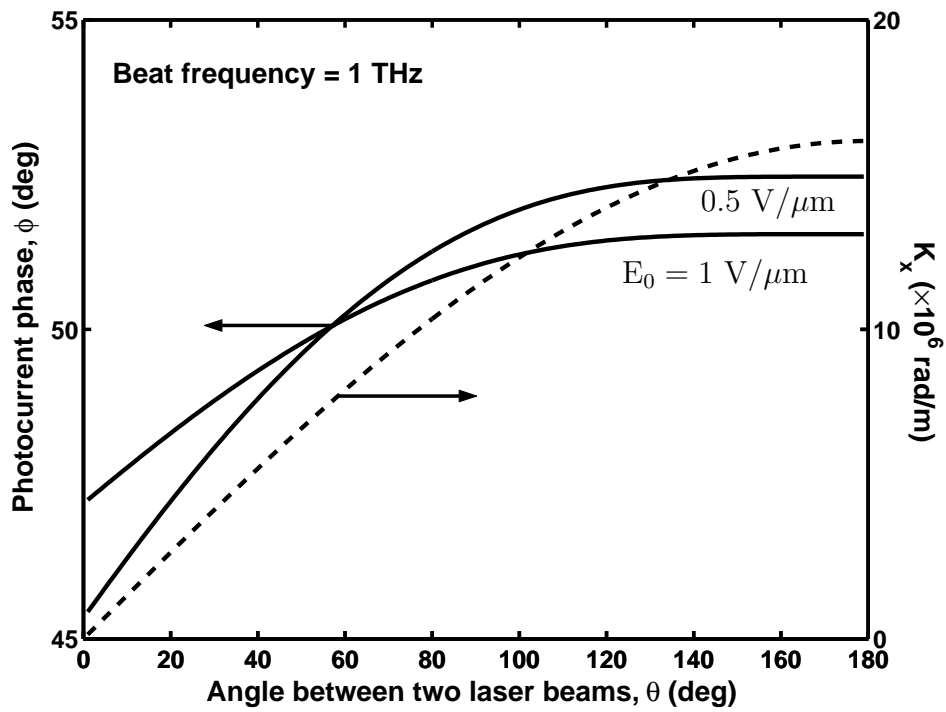


Figure 4.10: Longitudinal component of grating vector, K_x , and phase of terahertz photocurrent, ϕ , versus angle between the two laser beams.

Chapter 5

Integrated Photomixer-Antenna Elements

5.1 Introduction

In the last two chapters, we showed that the generated terahertz photocurrents in superconductive and photoconductive photomixers are travelling wave currents with a spatiotemporal distribution over the photomixing film. In this chapter we propose an integrated photomixer-antenna structure as an efficient terahertz source [81], [82]. Unlike conventional photomixers, in which a generated signal in an active region is coupled to an external antenna for radiation, in a photomixer-antenna element, the generated signal inside the photomixing film radiates simultaneously by designing the film as an efficient radiator. Incorporating a photomixing medium as an antenna element not only eliminates any source-to-antenna coupling problem, but also distributes the optical power over a bigger area and hence increases optical power handling capability of the device.

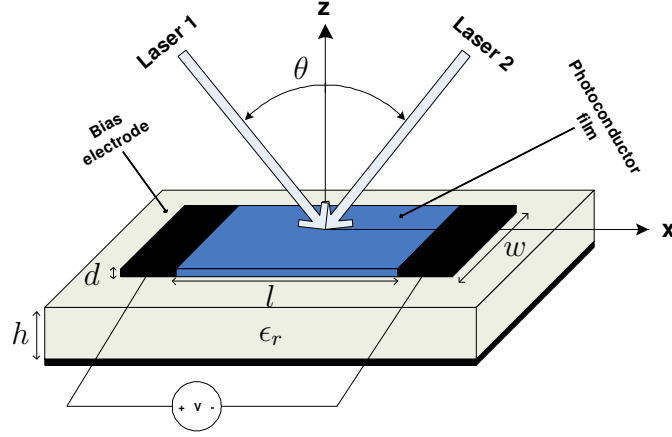


Figure 5.1: Longitudinal photoconductive photomixer scheme.

5.2 Longitudinal and Transversal Photomixer-Antenna Elements

Fig. 5.1 shows the configuration of a longitudinal photomixer. The two laser beams shine the entire film under the angle of θ in the $(x - z)$ plane, while the dc bias is applied in the x direction. In this case the grating vector \mathbf{K} is in the $(x - z)$ plane and hence from Eq. (4.64) the generated terahertz photocurrent can be written as

$$\tilde{J}_s(x) = [J_{s1}^2 + J_{s2}^2]^{1/2} e^{-j(K_x x + \phi)} \quad (5.1)$$

where J_{s1} , J_{s2} , and ϕ are given by Eqs. (4.67) to (4.69), respectively, and $K_x = (k_1 + k_2) \sin \theta / 2$ is the x -component of the grating vector, \mathbf{K} .

In this analysis we have not considered the effect of the finite width of the photoconductor film. For more accurate analysis, one has to apply the appropriate

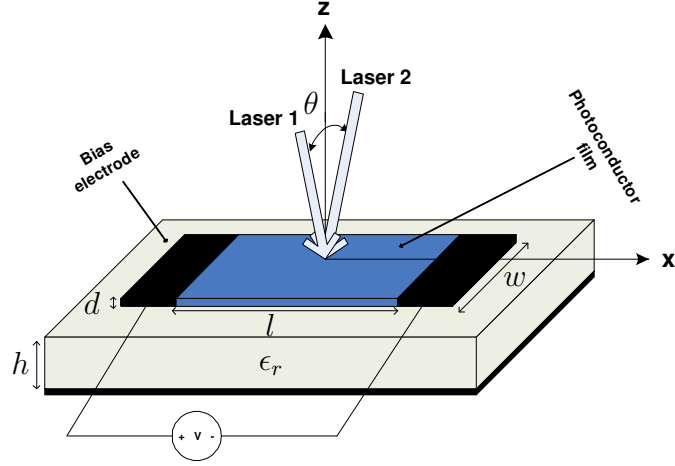


Figure 5.2: Transversal photoconductive photomixer scheme.

boundary conditions at the edges of the film to take this effect into account.

A transversal photomixer scheme is shown in Fig. 5.2. In this configuration, the optical interference grating is formed along the width of the photoconductor film, while the dc bias voltage is applied along the length of the film. In this case, the grating vector \mathbf{K} is in $(y - z)$ plane and hence from Eq. (4.64) the x component of the photocurrent can be written as

$$\tilde{J}_s(y) = [J_{s1}^2 + J_{s2}^2]^{1/2} e^{-j(K_y y + \phi)} \quad (5.2)$$

where J_{s1} , J_{s2} , and ϕ are given by Eqs. (4.67) to (4.69), respectively, in which K_x is replaced by zero, and $K_y = (k_1 + k_2) \sin \theta / 2$ is the y -component of the grating vector, \mathbf{K} .

Note that in this case the photocurrent has also a diffusion current component in y direction, which is much smaller than the drift current component given by Eq. (5.2).

The resulting traveling wave photocurrent distribution given by Eqs. (5.1) and

(5.2) can be either guided to a transmission line for circuit applications or can be radiated out by proper designing of the dimensions of the film.

5.2.1 Radiation from Photomixer-Antenna Elements

Since the current distribution inside the film is known and acts as a source of radiation, the electric current model can be employed to obtain the far field radiation from the antenna [203], [204].

The radiated field from an x -directed surface current source, $\tilde{J}_s(x, y)$ on a grounded substrate can be expressed as

$$E_{\theta(\phi)}(r, \theta, \phi) = E_{\theta(\phi)}^{hex} \int_{-w/2}^{w/2} \int_{-l/2}^{l/2} \tilde{J}_s(x, y) e^{jk_o \sin \theta [x \cos \phi + y \sin \phi]} dx dy \quad (5.3)$$

where $E_{\theta(\phi)}^{hex}$ is the radiated electric field from an x -directed Hertzian electric dipole on a grounded dielectric substrate given by [204]

$$E_{\theta}^{hex} = -E_0 G(\theta) \cos \phi \quad (5.4)$$

$$E_{\phi}^{hex} = E_0 F(\theta) \sin \phi \quad (5.5)$$

with

$$G(\theta) = \frac{2 \tan[k_0 h N(\theta)] \cos \theta}{\tan[k_0 h N(\theta)] - j \frac{\epsilon_r}{N(\theta)} \cos \theta} \quad (5.6)$$

$$F(\theta) = \frac{2 \tan[k_0 h N(\theta)]}{\tan[k_0 h N(\theta)] - j N(\theta) \sec \theta} \quad (5.7)$$

$$N(\theta) = \sqrt{\epsilon_r - \sin^2 \theta} \quad (5.8)$$

and

$$E_0 = \frac{j\Omega\mu_0}{4\pi r} e^{-jk_0 r} \quad (5.9)$$

Using Poynting's vector theorem [205], the radiated power can be written as

$$P_r = \frac{60}{\pi} \xi (J_{s1}^2 + J_{s2}^2) \quad (5.10)$$

where ξ is a configuration factor. For the longitudinal case

$$\begin{aligned} \xi = \int_0^{2\pi} \int_0^{\pi/2} \frac{\sin^2(k_0 w/2 \sin \theta \sin \phi)}{\sin \theta} \cdot \frac{\sin^2[l/2(k_0 \sin \theta \cos \phi - K_x)]}{(k_0 \sin \theta \cos \phi - K_x)^2} \\ \times [|G(\theta)|^2 \cot^2 \phi + |F(\theta)|^2] d\theta d\phi \end{aligned} \quad (5.11)$$

and for the transversal case

$$\begin{aligned} \xi = \int_0^{2\pi} \int_0^{\pi/2} \frac{\sin^2(k_0 l/2 \sin \theta \cos \phi)}{\sin \theta} \cdot \frac{\sin^2[w/2(k_0 \sin \theta \sin \phi - K_y)]}{(k_0 \sin \theta \sin \phi - K_y)^2} \\ \times [|G(\theta)|^2 + |F(\theta)|^2 \tan^2 \phi] d\theta d\phi \end{aligned} \quad (5.12)$$

in which ϵ_r and h are the relative dielectric constant and the thickness of the substrate, respectively. The radiated power is maximum for $l = \pi/K_x$ in the longitudinal case and for $w = \pi/K_y$ in the transversal case, at which a resonant condition occurs for the antenna.

The thickness of the substrate is determined based on the resonant condition and loss mechanisms of the structure. The best value for the thickness of the substrate, h , to minimize surface mode loss is [206]

$$h = \frac{\pi c}{2\Omega\sqrt{\epsilon_r - 1}} \quad (5.13)$$

The width of the photoconductor film in the longitudinal case and the length of the film in the transversal case determine the level of the absorbed optical power in the film as well as the directivity of the antenna.

5.2.2 Simulation Results for an LTG-GaAs Photomixer-Antenna Element

A photoconductive photomixer-antenna device made of LTG-GaAs is considered. All the physical parameters for a typical LTG-GaAs material are presented in Table 4.1.

The central wavelength of one of the lasers is 780 nm. The other laser is a tunable laser, which its wavelength can be tuned around 780 nm to result in the desired terahertz frequency. The total optical power density of the two lasers is $0.4 \text{ mW}/\mu\text{m}^2$. The angle between the two laser beams is $\theta = 4^\circ$. The resulting grating vector in the $x(y)$ direction is $K_{x(y)} = 0.561 (\mu\text{m})^{-1}$. The device is designed to operate at 2 THz. The substrate is GaAs with the relative permittivity of 12.6.

Based on the design criteria explained in the previous section, the optimum values of the geometrical parameters for the longitudinal and the transversal structures are computed. For the longitudinal case, the length of the film is $l = 5.6 \mu\text{m}$, while the width of the film is $w = 50 \mu\text{m}$. For the transversal case, the length and the width of the film are $l = 50 \mu\text{m}$ and $w = 5.6 \mu\text{m}$, respectively. The thickness of the film for both cases is $d = 2 \mu\text{m}$. The thickness of the substrate is a function of the beat frequency, and hence has a different value at different frequencies. This makes the proposed devices very narrow band radiators. At 2 THz, the thickness of the substrate is $h = 10.917 \mu\text{m}$.

Fig. 5.3 shows the amplitude of the terahertz photocurrent versus beat frequency,

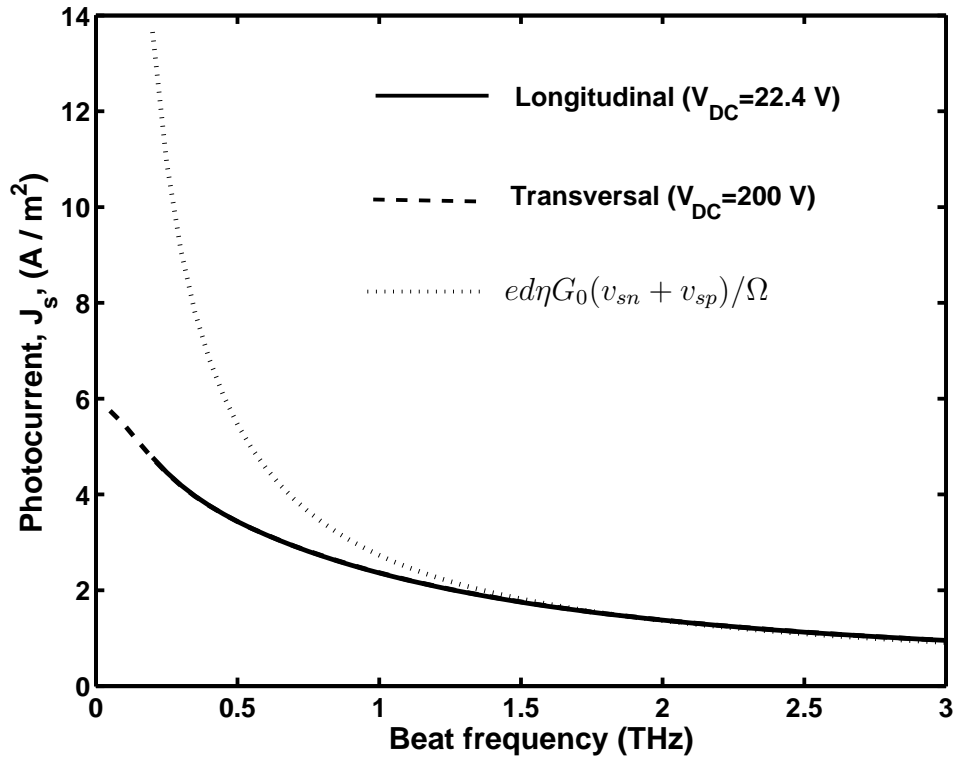


Figure 5.3: Amplitude of equivalent surface photocurrent in LTG-GaAs longitudinal and transversal photomixers. The total optical power density of the two lasers is $0.4 \text{ mW}/\mu\text{m}^2$. The applied dc bias to each element is $4 \text{ V}/\mu\text{m}$.

which decreases with frequency as $1/\Omega$ at high frequencies. As it can be seen from Fig. 5.3, the amplitude of the photocurrent is the same for the two cases. This means that the diffusion current is negligible in these devices, and the drift current is the main source of the terahertz signal. The dot-line curve shows an approximate expression for the terahertz photocurrent as $|\tilde{J}_s| \approx ed\eta G_0(v_{sn} + v_{sp})/\Omega$, which predicts accurate values for the terahertz photocurrent at high frequencies (see Eq. (4.63)). This approximation is not accurate for the low frequency range, where $\Omega\tau < 1$.

Shown in Fig. 5.4 is radiation power versus beat frequency for the transversal and the longitudinal photomixer-antenna devices. The absorbed optical power in each device is 74.6 mW. Since the amplitudes of the photocurrents for the two configurations are the same, the difference in the radiation power is the result of the difference in their configuration factors ξ (see Fig. 5.5). For the longitudinal case the photocurrent is a traveling wave current with its phase variation along x axis, while for the transversal case the phase variation of the traveling-wave photocurrent is along y axis. This results in different configuration factors for the two cases. From Fig. 5.4, the transversal scheme shows higher radiation power at high frequencies compare to its longitudinal counterpart; although it needs higher dc bias voltage due to its longer photo-excited length, l .

There is a frequency range around 2 THz, where two devices show better performance in terms of the radiation power. This behavior can be explained by Figs. 5.3 and 5.5. At low frequency range (< 1 THz), the amplitude of the photocurrent decreases smoothly with the beat frequency, while the configuration factor increases by the factor of Ω^2 . Hence from Eq. (5.10), the radiation power will increase with frequency for the low frequency range. At the high frequency range, the photocurrent decreases by the factor of $1/\Omega$, while the configuration factor linearly increases

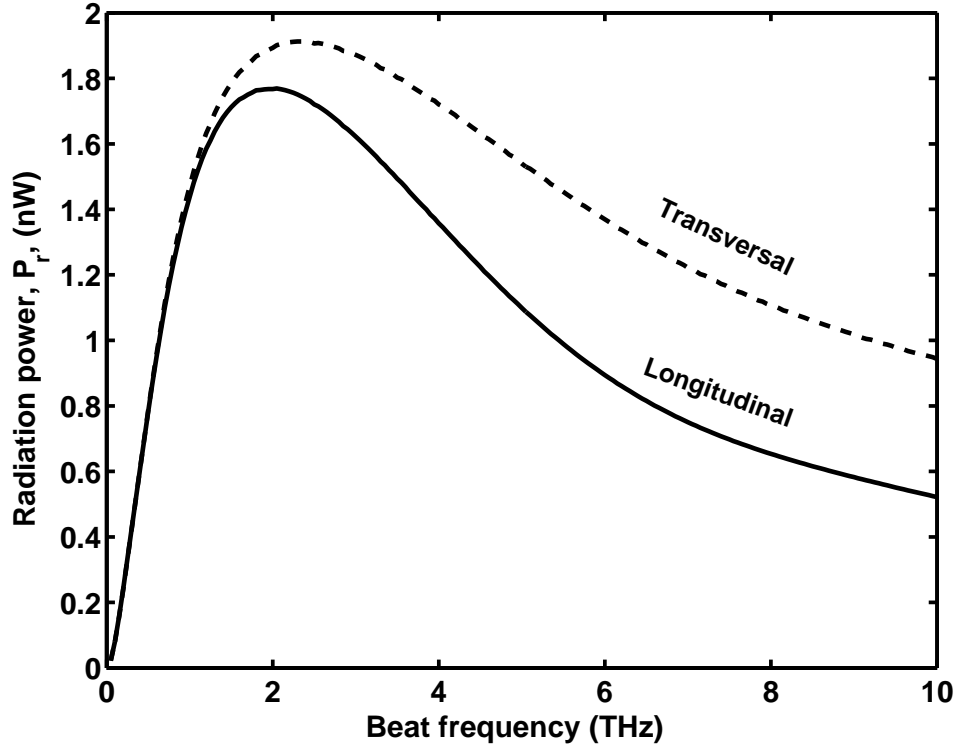


Figure 5.4: Radiation power of LTG-GaAs longitudinal and transversal photomixers. The total power density of the two lasers is $0.4 \text{ mW}/\mu\text{m}^2$. For the longitudinal case, the length of the film is $l = 5.6 \mu\text{m}$, while the width of the film is $w = 50 \mu\text{m}$. For the transversal case, the length and the width of the film are $l = 50 \mu\text{m}$ and $w = 5.6 \mu\text{m}$, respectively. The thickness of the film for both cases is $d = 2 \mu\text{m}$. The thickness of the substrate is changed according to the beat frequency to have maximum radiation at each frequency. The applied dc bias to each element is $4 \text{ V}/\mu\text{m}$.

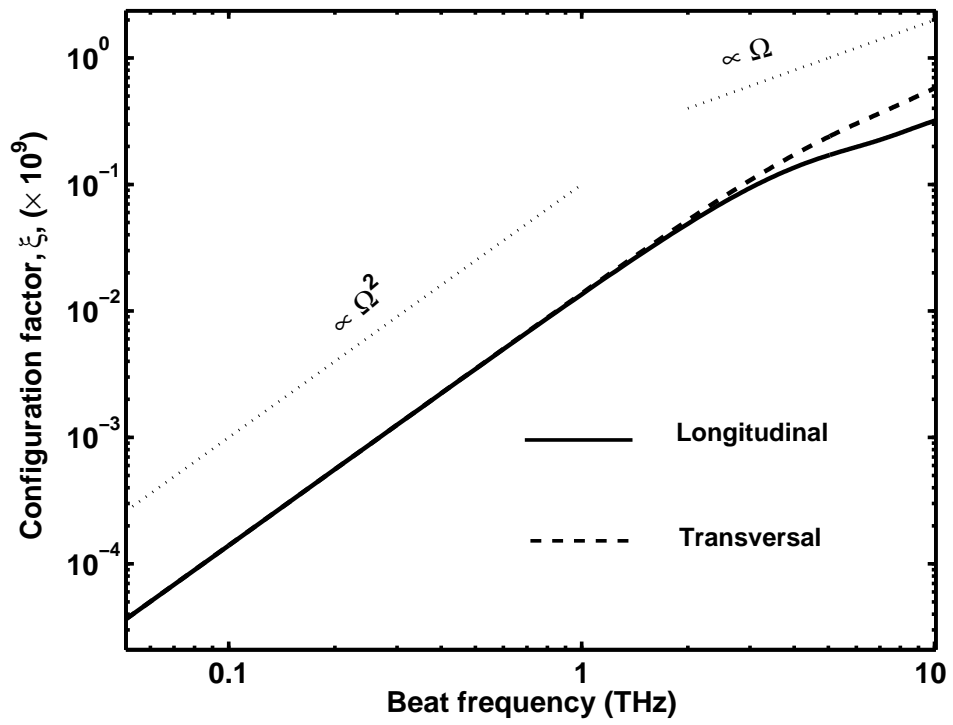


Figure 5.5: Configuration factor, ξ , for longitudinal and transversal photomixer-antenna devices.

by the beat frequency. This results in a decreasing radiation power by the factor of $1/\Omega$ at high frequency range.

Radiation power versus beat frequency for the longitudinal photomixer-antenna device operating at 2 THz is shown in Fig. 5.6. Since the structure is designed to resonate at the frequency of 2 THz ($\lambda = 10.917 \mu\text{m}$), the maximum radiation occurs at this frequency; although there are other harmonics that the device radiates reasonable power. One may use this narrow band characteristic of the proposed device to reduce the effect of the finite linewidth of the optical sources on device performance.

For the applications where a wideband radiator is needed, bow-tie or spiral antenna configurations can be used instead of simple rectangular antenna structure. The other choice is using thick substrate lens instead of the grounded substrate.

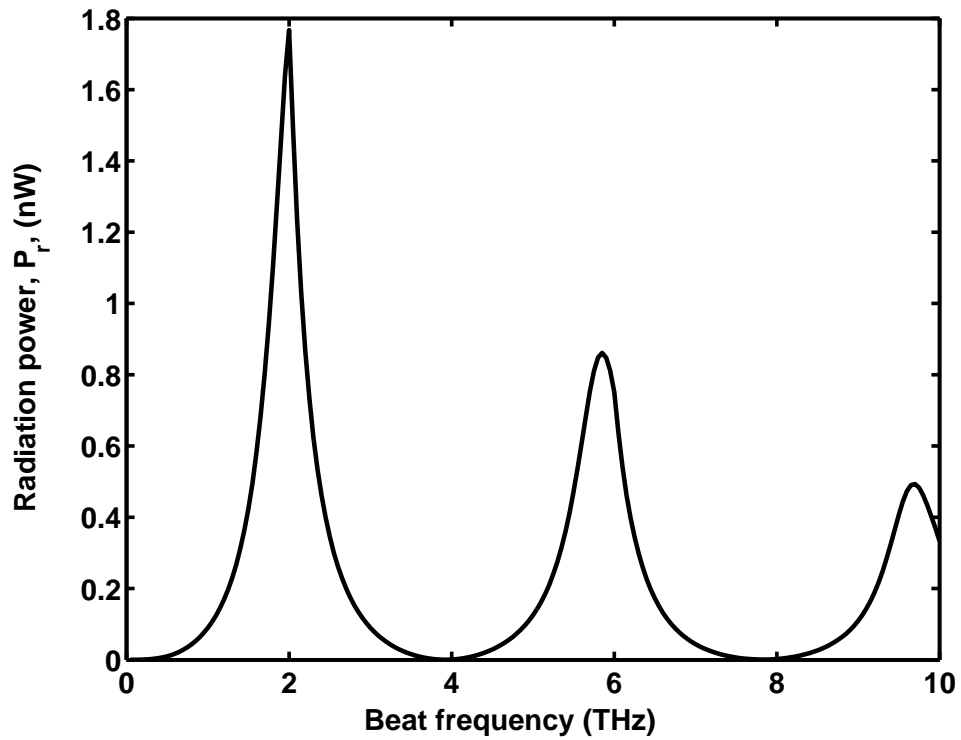


Figure 5.6: Radiation power of LTG-GaAs longitudinal photomixer designed for 2 THz beat frequency. The length of the film is $l = 5.6 \mu\text{m}$ and the width of the film is $w = 50 \mu\text{m}$. The thickness of the substrate is fixed at $h = 10.917 \mu\text{m}$ to have maximum radiation at 2 THz. The applied dc bias to each element is $4 \text{ V}/\mu\text{m}$.

Chapter 6

Photomixer-Antenna Array

The maximum available terahertz power from a single element photoconductive photomixer source is limited by the maximum sustainable optical power and dc bias before device failure. The available terahertz power can be increased by using an array of photomixers. The simple optical excitation scheme of a photomixer-antenna element makes it suitable for an array structure. Since there is no need for a feeding network for an array of these elements, one can excite the entire array by two laser beams. One can increase the radiation power by increasing the number of array elements and using high power lasers. On the other hand, one can change the phase distribution of the photocurrent in array elements by changing the angle between the two laser beams and steer the radiation beam.

6.1 Photoconductive Photomixer-Antenna Array

In this section, we introduce an array of photoconductive photomixer-antenna elements as a high power tunable CW terahertz source. The radiation characteristics

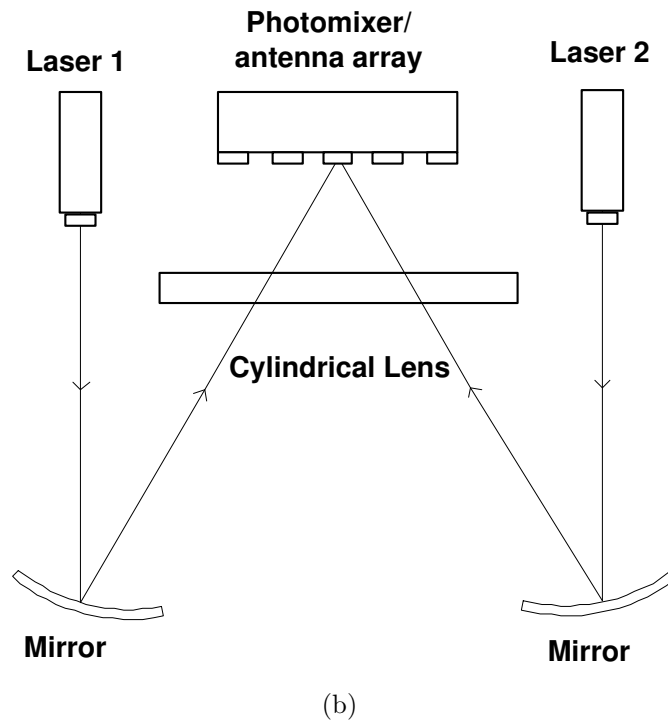
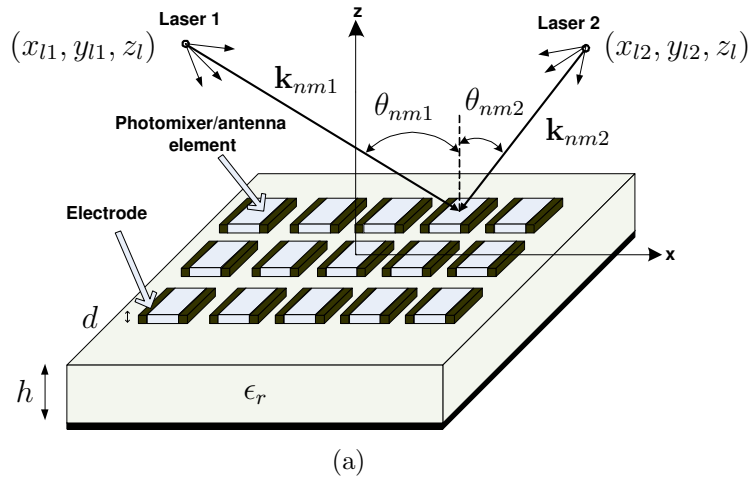


Figure 6.1: (a) Photoconductive photomixer-antenna array configuration (b) Optical excitation scheme.

of the proposed structure is analyzed and the simulation results for a designed sample are presented.

Fig. 6.1 shows the schematic of an $(2N + 1) \times (2M + 1)$ array of photoconductive photomixer-antenna elements. Photomixer elements are made of an ultra-fast photoconductor material, and are biased to a dc voltage by their bias electrodes. All the array elements are located above a grounded dielectric substrate. Two linearly polarized laser beams excite the entire structure. The corresponding electric field associated with each laser over the nm -th element can be written as

$$E_{nm1(2)} = |E_{nm1(2)}| e^{j(\omega_{1(2)}t - \mathbf{k}_{nm1(2)} \cdot \mathbf{r})} \quad (6.1)$$

where $n = -N, \dots, N$, $m = -M, \dots, M$, ω_1 and ω_2 are the angular frequencies of the lasers, \mathbf{k}_{nm1} and \mathbf{k}_{nm2} are the wave-vectors of the lasers over the nm -th element, and \mathbf{r} is the position vector over the same element. The lasers are assumed to be far enough from the surface of the photomixers so that the wave reaching each element can be assumed to be a local plane-wave. A uniform optical excitation can be achieved by coupling the laser beams to the array via an appropriate cylindrical lens.

Fig. 6.2 shows the array arrangement in $x - y$ plane. The wave-vectors \mathbf{k}_{nm1} and \mathbf{k}_{nm2} can be written as

$$\mathbf{k}_{nm1(2)} = k_{1(2)} \left[\cos \beta_{nm1(2)} \hat{x} + \cos \gamma_{nm1(2)} \hat{y} + \cos \theta_{nm1(2)} \hat{z} \right] \quad (6.2)$$

where k_1 and k_2 are the wave-numbers of the lasers in free space and

$$\cos \beta_{nm1(2)} = \frac{x_{nm} - x_{l1(2)}}{[(x_{nm} - x_{l1(2)})^2 + (y_{nm} - y_{l1(2)})^2 + z_l^2]^{1/2}} \quad (6.3)$$

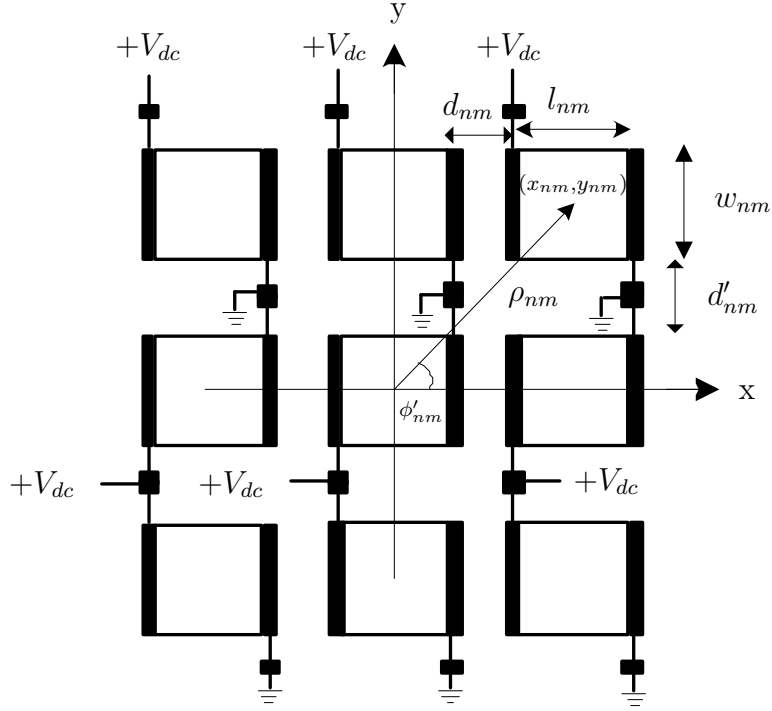


Figure 6.2: Array arrangement in $(x - y)$ plane.

$$\cos \gamma_{nm1(2)} = \frac{y_{nm} - y_{l1(2)}}{[(x_{nm} - x_{l1(2)})^2 + (y_{nm} - y_{l1(2)})^2 + z_l^2]^{1/2}} \quad (6.4)$$

$$\cos \theta_{nm1(2)} = \frac{-z_l}{[(x_{nm} - x_{l1(2)})^2 + (y_{nm} - y_{l1(2)})^2 + z_l^2]^{1/2}} \quad (6.5)$$

The incident laser beams interfere inside the array elements and create a spatiotemporal optical power density grating. Considering nonuniform absorption along the thickness of the photoconducting film, one can write the optical power density inside the nm -th element as

$$I_{nm}(\mathbf{r}, t) = I_0 T_{nm}(\theta_{nm1}, \theta_{nm2}) \left[1 + \eta_{nm} \cos(\Omega t - \mathbf{K}_{nm} \cdot \mathbf{r}) \right] e^{\alpha z} \quad (6.6)$$

where I_0 is the total optical power density of the lasers, T_{nm} is the optical power density transmission coefficient at photoconductor-air interface, α is the optical absorption coefficient, $0 < \eta_{nm} \leq 1$ is the modulation index or grating contrast, $\Omega = \omega_1 - \omega_2$ is the angular beat frequency, and $\mathbf{K}_{nm} = \mathbf{k}_{1nm} - \mathbf{k}_{2nm}$ is the grating vector.

The generated terahertz photocurrent inside the nm -th element is

$$\tilde{J}_{nm}^s(x, y) = J_{nm}^s e^{-j[K_{nmx}x + K_{nmy}y + \phi_{nm}]} \quad (6.7)$$

where

$$K_{nmx} = k_1 \cos \beta_{nm1} - k_2 \cos \beta_{nm2} \quad (6.8)$$

$$K_{nmy} = k_1 \cos \gamma_{nm1} - k_2 \cos \gamma_{nm2} \quad (6.9)$$

$$J_{nm}^s = \left[(J_{nm1}^s)^2 + (J_{nm2}^s)^2 \right]^{1/2} \quad (6.10)$$

$$\phi_{nm} = \tan^{-1} \frac{J_{nm2}^s}{J_{nm1}^s} \quad (6.11)$$

The expressions for J_{1nm}^s and J_{2nm}^s can be extracted from Eqs. (4.67) and (4.68), respectively.

The far field radiation from the nm -th element can be written as (see Fig. 6.2 for the definition of the parameters)

$$\begin{aligned} E_{\theta(\phi)}^{nm}(r, \theta, \phi) &= 4E_{\theta(\phi)}^{hex} \tilde{J}_{snm}(x_{nm}, y_{nm}) e^{jk_0 \rho_{nm} \sin \theta \cos(\phi - \phi'_{nm})} \\ &\times \frac{\sin[l_{nm}/2(k_0 \sin \theta \cos \phi - K_{nmx})]}{K_{nmx} - k_0 \sin \theta \cos \phi} \\ &\times \frac{\sin[w_{nm}/2(k_0 \sin \theta \sin \phi - K_{nmy})]}{k_0 \sin \theta \sin \phi - K_{nmy}} \end{aligned} \quad (6.12)$$

where $E_{\theta(\phi)}^{hex}$ are given by Eqs. (5.4) to (5.9) [page 79]. The superposition of all these radiated fields is the field produced by the array

$$E_{\theta(\phi)}(r, \theta, \phi) = \sum_{n=-N}^N \sum_{m=-M}^M E_{\theta(\phi)}^{nm}(r, \theta, \phi) \quad (6.13)$$

The total radiated power can be calculated using Poynting's vector theorem [205]

$$P_r = \frac{1}{2\eta_0} \int_0^{\pi/2} \int_0^{2\pi} [|E_\theta|^2 + |E_\phi|^2] r^2 \sin \theta \, d\phi d\theta \quad (6.14)$$

where η_0 is the free space impedance.

6.1.1 Array Design Procedure

The primary goal is to achieve maximum radiation power, which from Eq. (6.12) for the nm -th element occurs for

$$l_{nm} = \pi / K_{nmx} = \lambda_{nmx} / 2 \quad (6.15)$$

$$w_{nm} = \pi / K_{nmy} = \lambda_{nmy} / 2 \quad (6.16)$$

where λ_{nmx} and λ_{nmy} are the photocurrent spatial wavelengths along x-axis and y-axis, respectively. It can be seen from Eq. (6.8) that the x-component of the grating vector, K_{nmx} , is a relatively big number. From Eq. (6.15), the optimum values for the lengths of the array elements will be in the order of a few micrometers. On the other hand, the y-component of the grating vector, K_{nmy} , given by Eq. (6.9) is a small number and becomes zero for the array elements located on x-axis. Hence from Eq. (6.16), the wider the array elements the higher the radiation power.

In Eq. (6.15) both l_{nm} and K_{nmx} are related to the position of the nm -th element

in x-y plane. To find the optimum values of the lengths of the array elements from Eq. (6.15), one has to solve the following iterative equation for x_{nm}

$$\begin{aligned} x_{n(\pm m)} &= x_{n(\pm(m-1))} \pm 1/2l_{n(\pm(m-1))} \\ &\pm 3\pi/2 \left[\frac{(x_{n(\pm m)} - x_{l1})k_1}{[(x_{n(\pm m)} - x_{l1})^2 + (y_{nm} - y_{l1})^2 + z_l^2]^{1/2}} \right. \\ &\left. - \frac{(x_{n(\pm m)} - x_{l2})k_2}{[(x_{n(\pm m)} - x_{l2})^2 + (y_{nm} - y_{l2})^2 + z_l^2]^{1/2}} \right]^{-1} \end{aligned} \quad (6.17)$$

where $m = 1, \dots, M$, $n = -N, \dots, N$, $x_{n0} = 0$, and

$$l_{n0} = \pi \left[\frac{-x_{l1}}{[x_{l1}^2 + (y_{n0} - y_{l1})^2 + z_l^2]^{1/2}} k_1 + \frac{x_{l2}}{[x_{l2}^2 + (y_{n0} - y_{l2})^2 + z_l^2]^{1/2}} k_2 \right]^{-1} \quad (6.18)$$

The lengths of the array elements, l_{nm} , and their separation distances in x direction, d_{nm} , are equal to have a constructive spatial power combination, and can be calculated as

$$\begin{aligned} l_{nm} = d_{nm} &= \pi \left[\frac{x_{nm} - x_{l1}}{[(x_{nm} - x_{l1})^2 + (y_{nm} - y_{l1})^2 + z_l^2]^{1/2}} k_1 \right. \\ &\left. - \frac{x_{nm} - x_{l2}}{[(x_{nm} - x_{l2})^2 + (y_{nm} - y_{l2})^2 + z_l^2]^{1/2}} k_2 \right]^{-1} \end{aligned} \quad (6.19)$$

where $n = -N, \dots, N$ and $m = -M, \dots, -1, 1, \dots, M$.

The thickness of the substrate is determined based on the resonant condition and loss mechanisms of the structure and is given by Eq. (5.13) [page 80].

This design procedure guarantees maximum radiation for each of the array elements, but does not necessarily guarantee the maximum radiation for the entire array. To have maximum radiation for the entire array, one has to maximize Eq. (6.14), which is difficult to do analytically. As we will see in the next section, the radiation power for a designed array is close to the maximum radiation of the entire array.

6.1.2 Simulation Results for an LTG-GaAs Photomixer-Antenna Array

An 1×31 array configuration is considered for simulation purpose. Since the separation distance of the array elements in y direction is arbitrary, we set it equal to zero to maximize the photo-excited region and increase the radiation power. The array elements are made of LTG-GaAs located above a grounded GaAs substrate with the relative permittivity of 12.6. The elements are biased to a dc voltage of 7.5 V. Note that the applied electric field must be lower than GaAs breakdown field, which is around $40 \text{ V}/\mu\text{m}$ [190], [192]. The thickness of the array elements is $2 \mu\text{m}$. All the physical parameters for a typical LTG-GaAs material are presented in Table 3.1.

The entire array is excited by two detuned single-mode lasers operating around 780 nm with their frequency difference falling in the terahertz spectrum. The total optical power density of the two lasers is $0.12 \text{ mW}/\mu\text{m}^2$. The LTG-GaAs photomixers can withstand an optical power density of $0.9 \text{ mW}/\mu\text{m}^2$ with $4 \text{ V}/\mu\text{m}$ dc bias at room temperature [46]. The two lasers are located in $x - z$ plane with $x_{l2} = -x_{l1} = 1.3 \text{ mm}$ and $z_l = 50 \text{ mm}$. The array is designed to work at 1 THz. For this frequency the optimum value for the thickness of the substrate is $21.8 \mu\text{m}$. The lengths of the array elements and their separation distances are calculated from Eqs. (6.17) to (6.19), and are around $7.46 \mu\text{m}$. The width of the array elements is $120 \mu\text{m}$.

Fig. 6.3 shows radiation power versus beat frequency for the designed array. The power of each laser is 3.33 W, and the consumed optical power in each element is 107 mW. A Ti:sapphire laser can generate the required optical power. In order to decrease the thermal effects of the absorbed optical power and the applied dc bias,

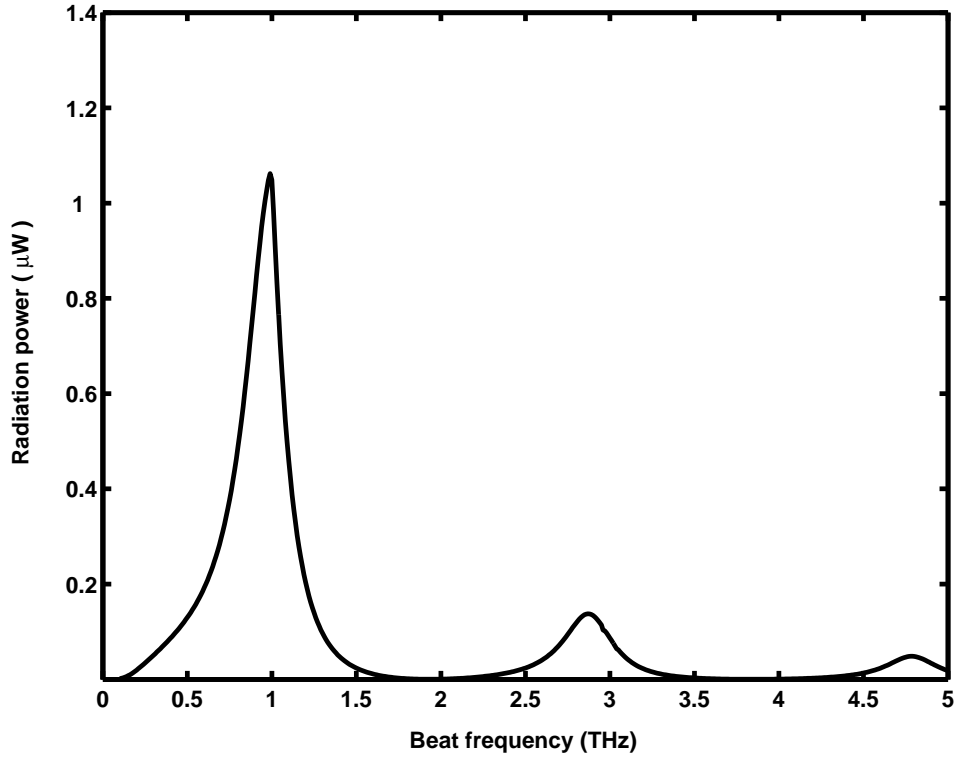


Figure 6.3: Total terahertz radiation power of an 1×31 photoconductive photomixer- antenna array made of LTG-GaAs versus beat frequency. The thickness of the substrate is fixed at $21.8 \mu\text{m}$ to have maximum radiation at 1 THz. The total optical power density of the two lasers is $0.12 \text{ mW}/\mu\text{m}^2$. The lengths of the array elements and their separation distances are calculated from Eqs. (6.17) to (6.19), and are around $7.46 \mu\text{m}$. The width of the array elements is $120 \mu\text{m}$. The elements are biased to a dc voltage of 7.5 V.

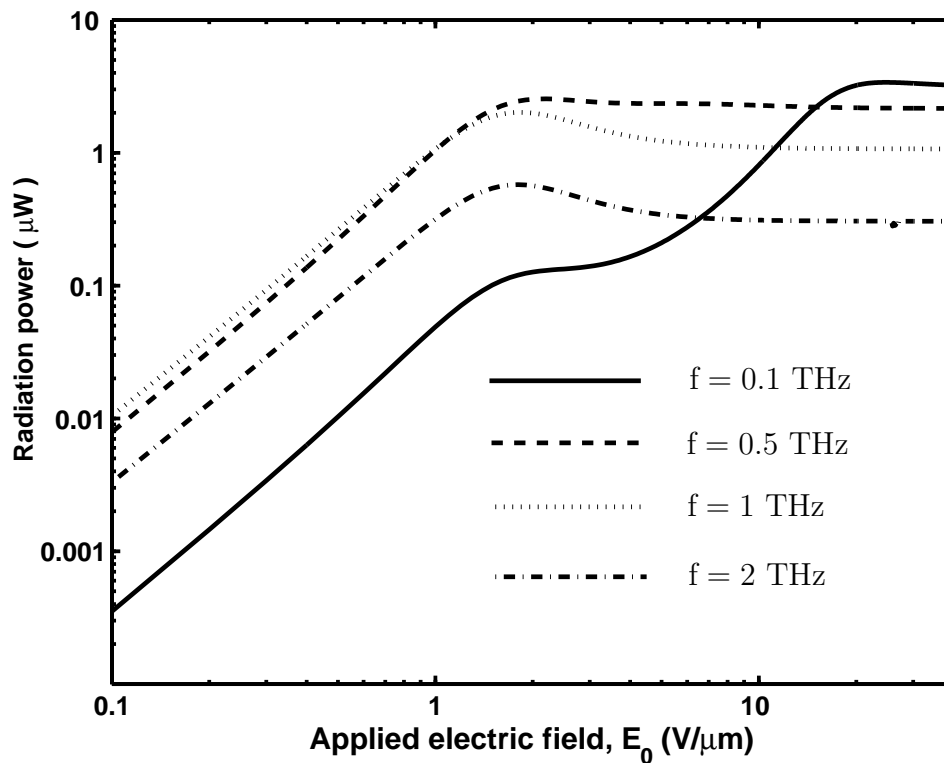


Figure 6.4: Total terahertz radiation power of an 1×31 photoconductive photomixer-antenna array made of LTG-GaAs versus applied electric field at different beat frequencies. The thickness of the substrate is changed according to the beat frequency to have maximum radiation at each frequency. The total power density of the two lasers is $0.12 \text{ mW}/\mu\text{m}^2$.

one can use a good thermal conductor layer, such as AlAs layer [78], beneath the LTG-GaAs layer. Operating the photomixer at the low temperatures is another way to increase the maximum sustainable optical power and dc bias of the device [46]. It can be seen from Fig. 6.3 that around $1 \mu\text{W}$ power is achievable at 1 THz. The optical-to-electrical efficiency of the device is 0.0032%. The optimum thickness of the substrate is a function of frequency, which makes the structure a narrow band radiator.

Shown in Fig. 6.4 is radiated power versus applied dc bias. The applied electric field is the ratio of the applied dc voltage to the length of the array elements. The radiation power saturates with the applied electric field, which is the result of the carrier velocity saturation in photoconductor. As it can be seen from Fig. 6.4, for an LTG-GaAs sample with the physical parameters given in Table 3.1, the saturation region starts at the applied electric field around $E_0 = 3 \text{ V}/\mu\text{m}$ for the beat frequency above 0.5 THz. The optimum value of the applied dc bias for maximum terahertz radiation and minimum thermal effect is the value corresponding to the starting point of the saturation region.

Fig. 6.5 shows radiation power versus beat frequency, where the thickness of the substrate is changed according to the beat frequency to have maximum radiation at each frequency. According to Fig. 6.5, the radiation power decreases with frequency by the rate of $1/\Omega$ [79].

From Fig. 6.1, the angle between the beams of the two lasers located in $x - z$ plane can be defined as $\theta_l = \theta_{001} + \theta_{002} = -\tan^{-1}(x_{l1}/z_l) + \tan^{-1}(x_{l2}/z_l)$. Fig. 6.6 shows radiation pattern at the plane of $\phi = 0$ for different values of θ_l , and for arrays with different number of elements. It can be seen that by changing the angle between the two lasers one can steer the radiation beam. The grating vector, \mathbf{K}_{nm} , changes by changing the angle between the two lasers, which consequently

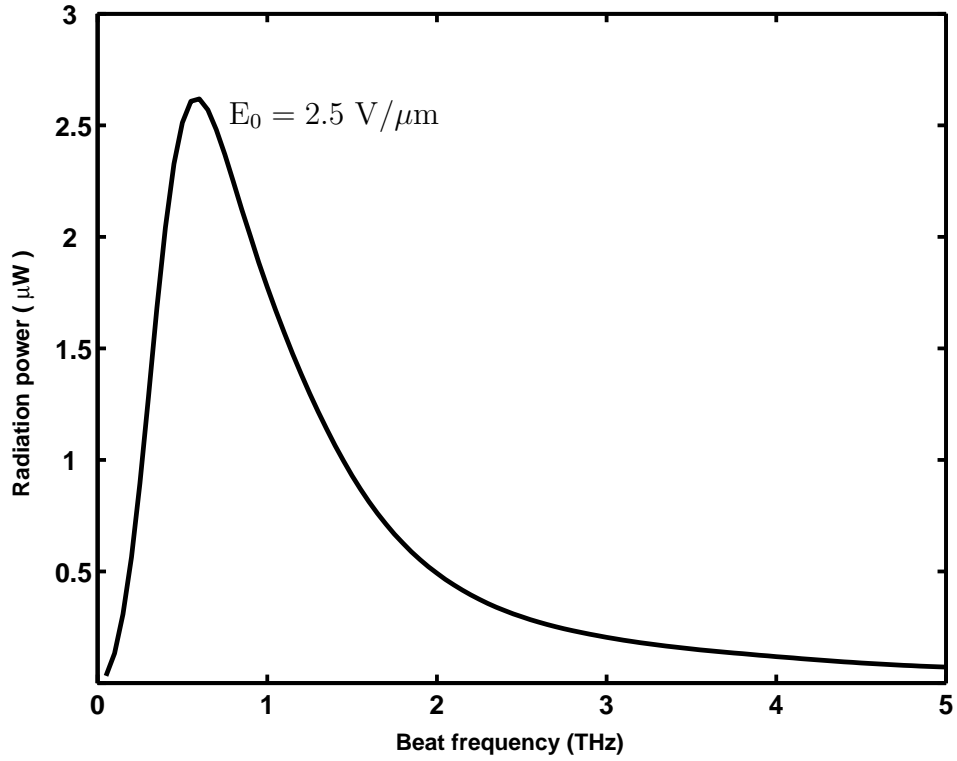


Figure 6.5: Total terahertz radiation power of an 1×31 photoconductive photomixer-antenna array made of LTG-GaAs versus beat frequency. The thickness of the substrate changes according to the beat frequency to have maximum radiation at each frequency. The total optical power density of the two lasers is $0.12 \text{ mW}/\mu\text{m}^2$.

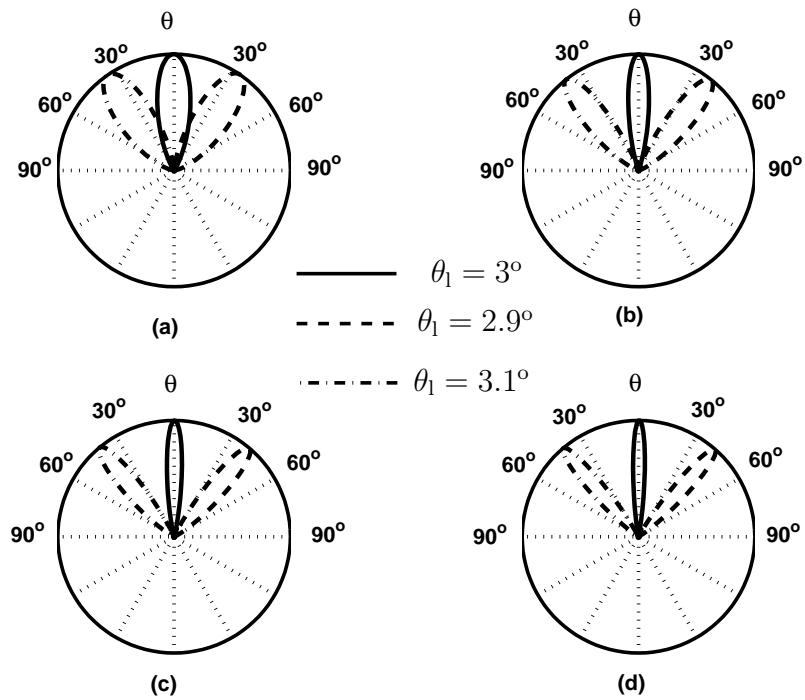


Figure 6.6: Radiation pattern at $\phi = 0$ plane for different number of array elements and at the beat frequency of 1 THz; (a) 1×31 array (FWHM = 6.59°), (b) 1×51 array (FWHM = 4°), (c) 1×71 array (FWHM = 2.88°), (d) 1×91 array (FWHM = 2.3°).

changes the phase distribution of the current over the array elements and results in pattern deflection. It also can be seen from Fig. 6.6 that the radiation beam becomes narrower by increasing the number of array elements. Fig. 6.7 shows the radiation pattern of the designed array at $\phi = 0$ and $\phi = \pi/2$ planes. The radiation pattern is symmetric and its side-lobe level is around -13.2 dB.

Shown in Fig. 6.8 is radiation power for different values of the angle between the two lasers. As it can be seen from Fig. 6.8, the maximum radiation of the entire array occurs at an angle very close to $\theta_l = 3^\circ$. The radiation power rapidly drops for the angles far from the angle that the array is designed for, because at these angles the maximum radiation condition given by Eq. (6.15) is no longer valid. The line shown in Fig. 6.8 is asymmetric with respect to θ_l , since the grating vector \mathbf{K}_{nm} is not symmetric with respect to θ_l .

Fig. 6.9 shows that one can increase the terahertz radiation power by using higher power lasers and increasing the number of array elements. The radiation power does not scale as the square of the number of array elements, while it is proportional to the square of the optical power (see Fig. 6.10). Hence, for a given amount of the optical power, the optimum design is an array with minimum number of elements, while each element absorbs its maximum consumable optical power.

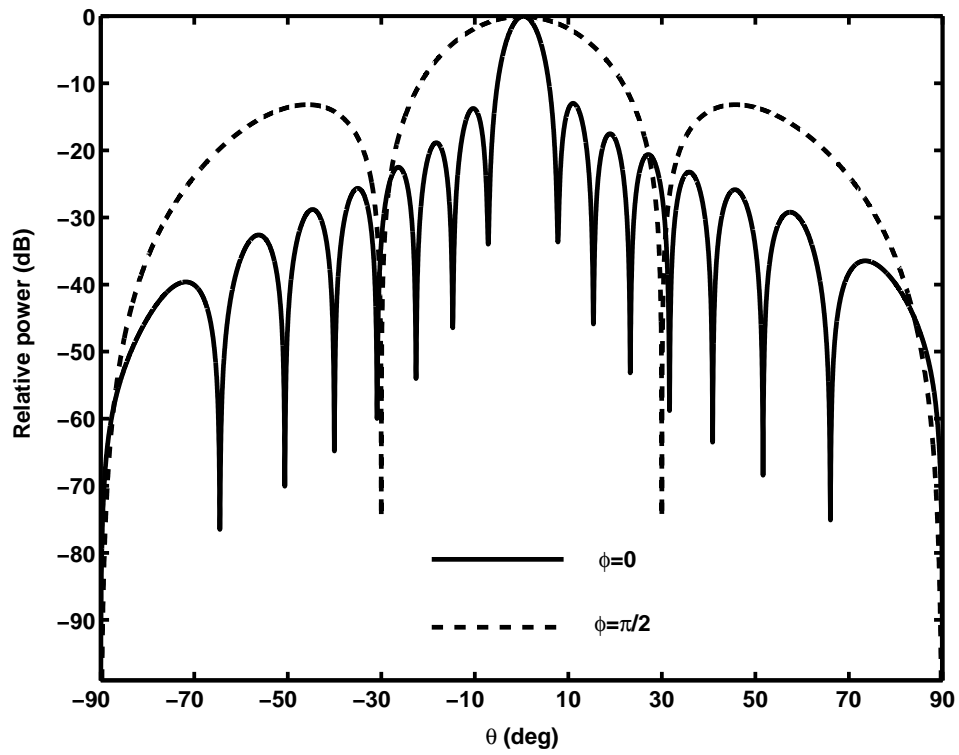


Figure 6.7: Radiation pattern at $\phi = 0$ and $\phi = \pi/2$ planes for an 1×31 array at the beat frequency of 1 THz and $\theta_1 = 3.02^\circ$.

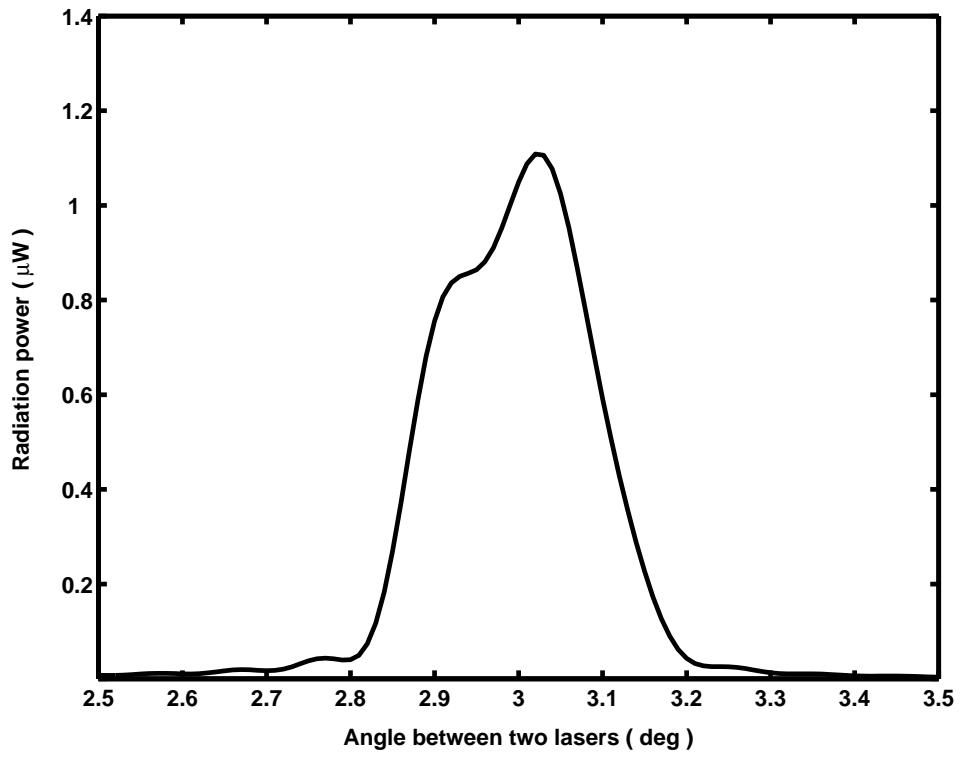


Figure 6.8: Terahertz radiation power versus angle between the two lasers at the beat frequency of 1 THz.

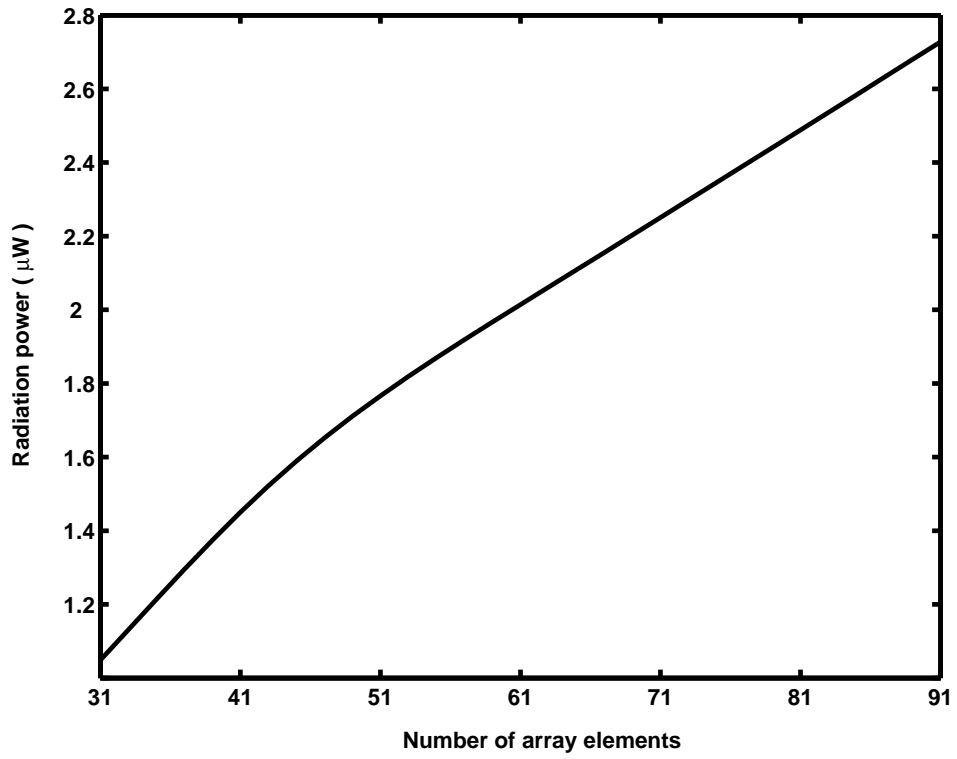


Figure 6.9: Terahertz radiation power versus number of array elements at the beat frequency of 1 THz and for a constant optical power density of $0.12 \text{ mW}/\mu\text{m}^2$.

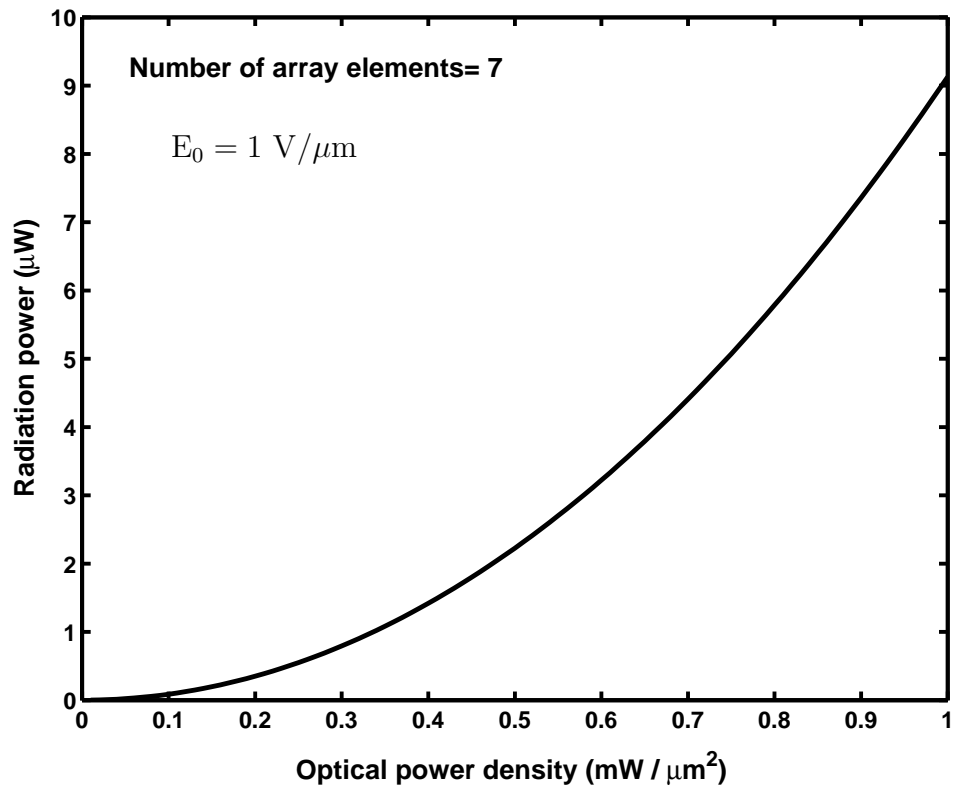


Figure 6.10: Terahertz radiation power versus total optical power density at the beat frequency of 1 THz.

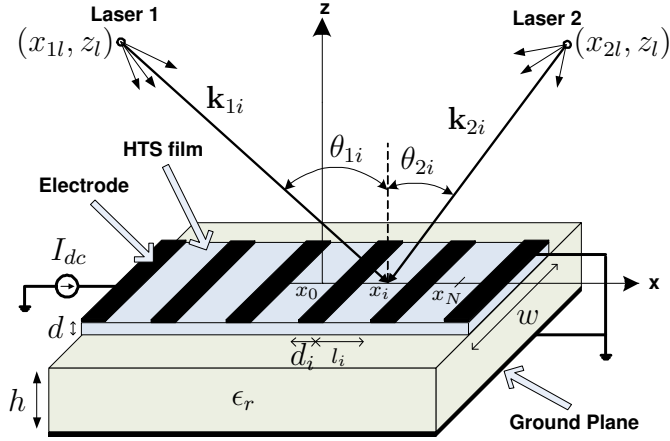


Figure 6.11: Superconductive photomixer-antenna array configuration.

6.2 Superconductive Photomixer-Antenna Array

Fig. 6.11 shows the schematic of an array of HTS photomixer-antenna elements. The array structure consists of an epitaxially grown HTS thin film on a suitable substrate using a growing technique such as molecular beam epitaxy (MBE), sputtering, laser ablation, or metal-organic chemical vapor deposition (MOCVD) [207]. The HTS film can be patterned using standard photolithographic techniques. The electrodes can be printed on the HTS film by lift-off techniques followed by an annealing process in an oxygenated environment to reduce the contact resistance and improve the adhesion of the metal pads to the HTS film [177]. The ground plane can be deposited on the back side of the substrate by evaporation or sputtering techniques. A dc current source connected to the electrodes provides a constant bias current for the array elements. One can change the number of array elements by connecting the current source to the appropriate electrode.

Two linearly polarized lasers are located in $x - z$ plane far enough from the surface

of the photomixers so that the wave reaching each element can be assumed to be a local plane-wave. The corresponding electric field associated with each laser over the i -th element can be written as

$$E_{1(2)i} = |E_{1(2)i}| e^{j(\omega_{1(2)}t - \mathbf{k}_{1(2)i} \cdot \mathbf{r})} \quad (6.20)$$

where $i = -N, \dots, N$, ω_1 and ω_2 are the angular frequencies of the lasers, \mathbf{k}_{1i} and \mathbf{k}_{2i} are the wave-vectors of the lasers over the i -th element, and \mathbf{r} is the position vector over the same element.

The wave-vectors \mathbf{k}_{1i} and \mathbf{k}_{2i} can be written as

$$\mathbf{k}_{1i} = \frac{(x_i - x_{1l})\hat{x} - z_l\hat{z}}{[(x_i - x_{1l})^2 + z_l^2]^{1/2}} k_1 \quad (6.21)$$

$$\mathbf{k}_{2i} = \frac{(x_i - x_{2l})\hat{x} - z_l\hat{z}}{[(x_i - x_{2l})^2 + z_l^2]^{1/2}} k_2 \quad (6.22)$$

where k_1 and k_2 are the wave-numbers of the lasers in free space.

The incident laser beams interfere inside the elements and create a spatiotemporal grating. The optical power distribution inside the i -th element can be written as

$$P_i(\mathbf{r}, t) = P_{0i}(1 - R) \left[1 + \eta_i \cos(\Omega t - \mathbf{K}_i \cdot \mathbf{r}) \right] e^{\alpha z} \quad (6.23)$$

where P_{0i} is the total power of the lasers, R is the optical reflectivity, α is the optical absorption coefficient, $0 < \eta_i \leq 1$ is the modulation index or grating contrast, $\Omega = \omega_1 - \omega_2$ is the angular beat frequency, and $\mathbf{K}_i = \mathbf{k}_{1i} - \mathbf{k}_{2i}$ is the grating vector. The total equivalent surface current density over the i -th element of the array can be written as [80]

$$J_i^s(x, t) = J_{dc}^s + \Re\{ \tilde{J}_i^s e^{j\Omega t} \} \quad (6.24)$$

where

$$J_{dc}^s = \frac{I_{dc}}{w} \quad (6.25)$$

$$\tilde{J}_i^s = J_i^s e^{-j[K_{ix}x + \phi_i]} \quad (6.26)$$

with

$$J_i^s = [(J_{1i}^s)^2 + (J_{2i}^s)^2]^{1/2} \quad (6.27)$$

$$K_{ix} = \frac{(x_i - x_{1l})k_1}{[(x_i - x_{1l})^2 + z_l^2]^{1/2}} - \frac{(x_i - x_{2l})k_2}{[(x_i - x_{2l})^2 + z_l^2]^{1/2}} \quad (6.28)$$

$$\phi_i = \tan^{-1} \frac{J_{2i}^s}{J_{1i}^s} \quad (6.29)$$

The expressions for J_{1i}^s and J_{2i}^s can be extracted from Eqs. (3.40) and (3.41), respectively.

As it can be seen from Eq. (6.24), the total current inside each element contains a dc component and a traveling-wave terahertz component, where the dc component is equal to the bias current. From energy conversion point of view, in each element a part of the energy of the exciting lasers is converted to the terahertz signal [80]. Having the current distribution over each element, the far field radiation can be calculated as

$$E_{\theta(\phi)}^i(r, \theta, \phi) = E_{\theta(\phi)}^{hex} \int_{-w/2}^{w/2} \int_{x_i-l_i/2}^{x_i+l_i/2} J_i^s e^{-j[K_{ix}x + \phi_i]} \times e^{jk_0 \sin \theta [x \cos \phi + y \sin \phi]} dx dy \quad (6.30)$$

Doing the integration results in

$$E_{\theta(\phi)}^i(r, \theta, \phi) = 4E_{\theta(\phi)}^{hex} J_i^s e^{-j\phi_i} e^{j[k_0 \sin \theta \cos \phi - K_{ix}]x_i} \times \frac{\sin[l_i/2(k_0 \sin \theta \cos \phi - K_{ix})]}{K_{ix} - k_0 \sin \theta \cos \phi} \frac{\sin[w/2(k_0 \sin \theta \sin \phi)]}{k_0 \sin \theta \sin \phi} \quad (6.31)$$

where $E_{\theta(\phi)}^{hex}$ are given by Eqs. (5.4) to (5.9) [page 79] and k_0 is the free space wave-number. The superposition of all these radiated fields is the field produced by the array

$$E_{\theta(\phi)}(r, \theta, \phi) = \sum_{i=-N}^N E_{\theta(\phi)}^i(r, \theta, \phi) \quad (6.32)$$

The total radiated power can be calculated using Poynting's vector theorem [205]

$$P_r = \frac{1}{2\eta_0} \int_0^{\pi/2} \int_0^{2\pi} [|E_\theta|^2 + |E_\phi|^2] r^2 \sin \theta \, d\phi d\theta \quad (6.33)$$

where η_0 is the free space impedance.

6.2.1 Array Design Procedure

The length and the location of the array elements must be chosen judiciously to have maximum radiation for each element and constructive power combination. From Eq. (6.31), the maximum radiation for the i -th element occurs for

$$l_i = \pi / K_{ix} = \lambda_{ix} / 2 \quad (6.34)$$

where λ_{ix} is the photocurrent spatial wavelength along x-axis.

In Eq. (6.34), both l_i and K_{ix} are related to the position of the i -th element along x-axis. To find the optimum values for the lengths of the array elements from Eq. (6.34), one has to solve the following iterative equation for x_i

$$x_{\pm i} = x_{\pm(i-1)} \pm \frac{1}{2} l_{\pm(i-1)} \pm \frac{3\pi}{2} \left[\frac{(x_{\pm i} - x_{1l})k_1}{[(x_{\pm i} - x_{1l})^2 + z_l^2]^{1/2}} - \frac{(x_{\pm i} - x_{2l})k_2}{[(x_{\pm i} - x_{2l})^2 + z_l^2]^{1/2}} \right]^{-1} \quad (6.35)$$

where $i = 1, \dots, N$, $x_0 = 0$, and

$$l_0 = \pi \left[\frac{-x_{1l}}{(x_{1l}^2 + z_l^2)^{1/2}} k_1 + \frac{x_{2l}}{(x_{2l}^2 + z_l^2)^{1/2}} k_2 \right]^{-1} \quad (6.36)$$

To have a constructive spatial power combining, one has to choose $d_i = l_i$. Once x_i is calculated from Eq. (6.35), one can calculate the lengths of the array elements l_i and their separation distances d_i as

$$l_i = d_i = \pi \left[\frac{(x_i - x_{1l})k_1}{[(x_i - x_{1l})^2 + z_l^2]^{1/2}} - \frac{(x_i - x_{2l})k_2}{[(x_i - x_{2l})^2 + z_l^2]^{1/2}} \right]^{-1} \quad (6.37)$$

where $i = -N, \dots - 1, 1, \dots, N$.

The thickness of the substrate is given by Eq. (5.13) [page 80].

To have maximum radiation for the entire array, one has to maximize the expression given by Eq. (6.33), which is difficult to do analytically. As we will see in the next section, after designing the array based on the above-mentioned procedure, the maximum radiation can be achieved by a small tuning of the positions of the lasers.

6.2.2 Simulation Results for an YBCO Photomixer-Antenna Array

An array with 61 elements is considered for simulation purpose. The array elements are made of $\text{YBa}_2\text{Cu}_3\text{O}_{7-\delta}$ high-temperature superconductor, which is epitaxially grown on LaAlO_3 substrate with relative permittivity of 24. The ground plane is deposited on the back side of the substrate. The thickness and the width of the array elements are 130 nm and 40 μm , respectively. The array elements are biased to a dc current of 23.8 mA. All the physical parameters for a typical $\text{YBa}_2\text{Cu}_3\text{O}_{7-\delta}$

material are presented in Table 4.1.

The entire array is excited by two detuned single-mode lasers operating around 532 nm with their frequency difference falling in the terahertz spectrum. Each laser radiates 114 mW optical power, which results in 3.4 mW total absorbed power for each element. The two lasers are located in $x - z$ plane with $x_{2l} = -x_{1l} = 1.3$ mm and $z_l = 50$ mm.

From Fig. 6.11, the angle between the two lasers can be defined as $\theta_l = \theta_{10} + \theta_{20} = -\tan^{-1}(x_{1l}/z_l) + \tan^{-1}(x_{2l}/z_l)$, which results in $\theta_l = 3^\circ$ for this specific configuration. The array is designed to work at 3 THz frequency. At this frequency, the optimum value for the thickness of the substrate is $5.21 \mu\text{m}$. The lengths of the array elements and their separation distances are calculated from Eqs. (6.35) to (6.37) (see Fig. 6.12).

Shown in Fig. 6.13 is radiation power versus angle between the two lasers. As it can be seen from Fig. 6.13, the optimum value for the angle between the two lasers is $\theta_l = 3.08^\circ$, where the maximum radiation of the entire array happens. Hence, after designing the array for $\theta_l = 3^\circ$, the lasers must be relocated to have $\theta_l = 3.08^\circ$. The radiation power rapidly drops for the angles far from the angle that the array is designed for, since at these angles the maximum radiation condition given by Eq. (6.34) is no longer valid.

Fig. 6.14 shows radiation power versus beat frequency for the designed array. It can be seen that about 0.2 mW power is achievable at 3 THz. The bath temperature is $T_0 = 85$ K. Note that upon optical excitation, the temperature of the HTS film increases above the bath temperature. To have the HTS film in its superconducting state, the power of the lasers must be smaller than a critical value [80]. Fig. 6.14 also shows the variation of the radiation power with thickness of the substrate.

Fig. 6.15 shows radiation power versus beat frequency at two different bath tem-

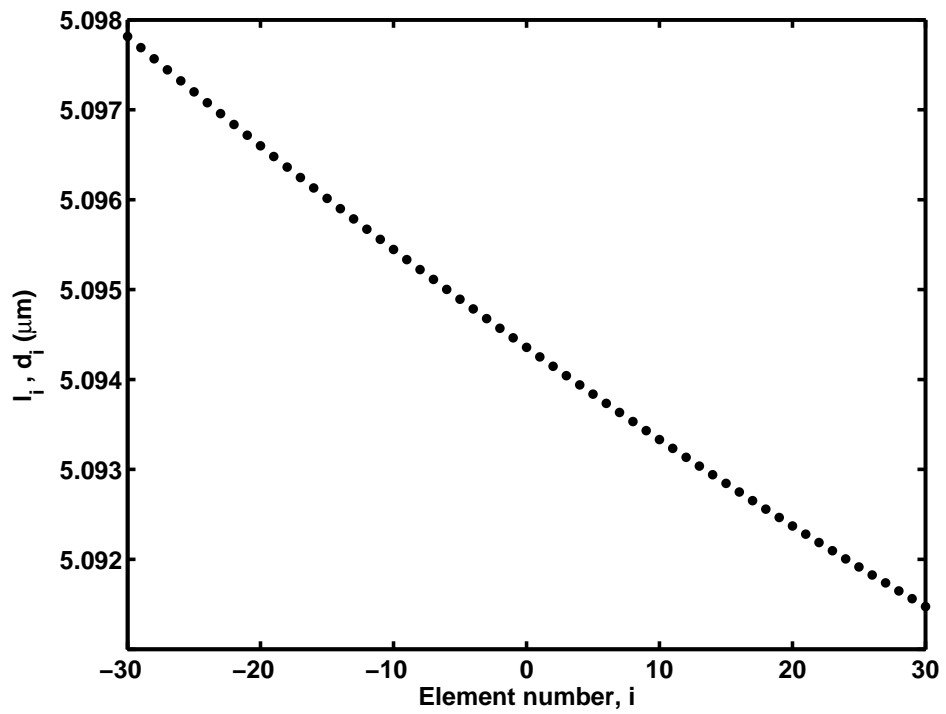


Figure 6.12: Lengths of the array elements and their separation distances.

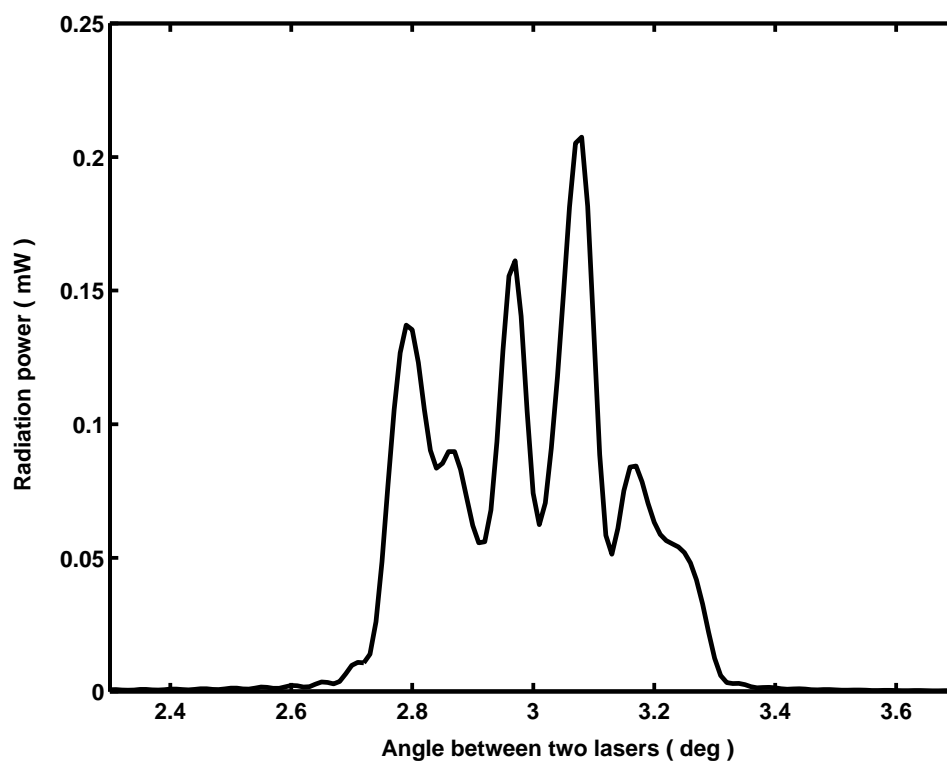


Figure 6.13: Terahertz radiation power versus angle between the two lasers.

peratures, where the thickness of the substrate is changed according to the beat frequency to have maximum radiation at each frequency. As it can be seen from Fig. 6.15, the radiation power increases with the beat frequency, the behavior that has been explained in Chapter 3, and also has been reported by Stevens and Edwards [57]. Fig. 6.15 also shows that the radiation power is higher for the bath temperatures closer to the critical temperature of the HTS material. The maximum obtainable frequency is limited by the gap frequency of the YBCO sample, which can be from 5 THz to 30 THz for different samples.

Fig. 6.16 shows radiation pattern for different values of θ_i . The array has a narrow beam radiation pattern with - 13 dB side-lobe level. It can be seen that by changing the angle between the two lasers one can steer the radiation beam. The beam steering is due to the change of the grating vector, \mathbf{K}_i , which consequently changes of the current phase distribution over the array elements.

One can increase the terahertz radiation power by using higher power lasers and increasing the number of array elements. The size of an array with 101 elements is $1 \text{ mm} \times 40 \text{ }\mu\text{m}$. Using two lasers with total optical power of 379 mW, one can achieve 0.44 mW power at 3 THz for an array with 101 elements.

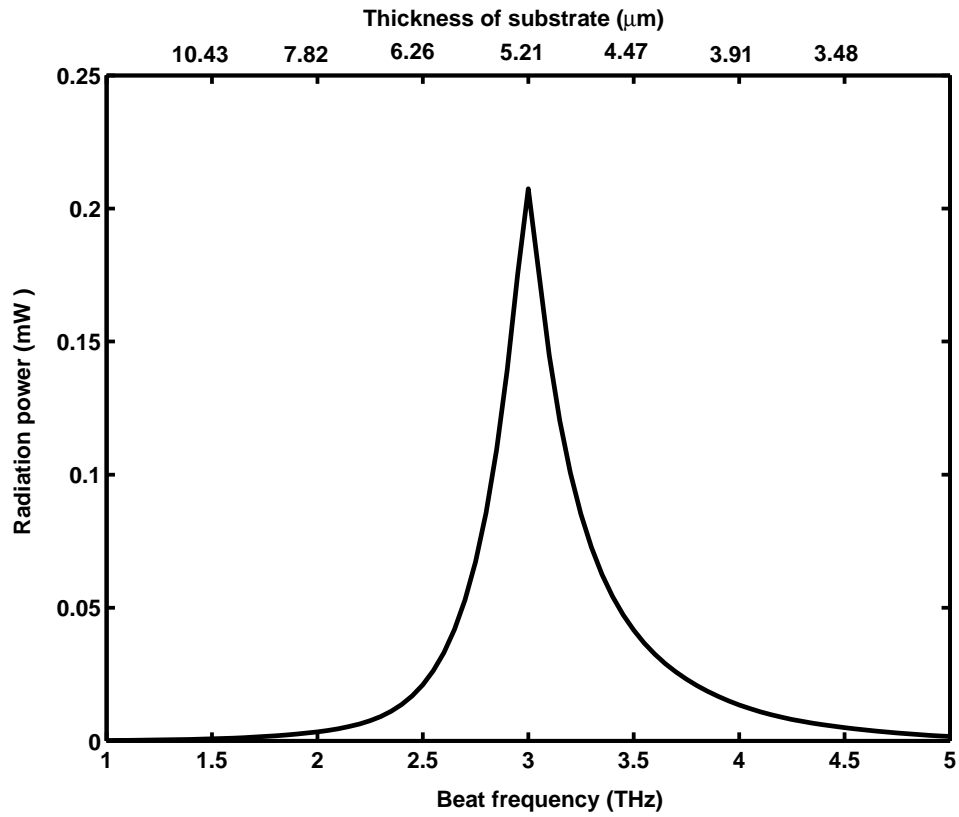


Figure 6.14: Terahertz radiation power versus beat frequency for an YBCO array with 61 elements designed to operate at 3 THz. The thickness of the substrate is 5.21 μm . The thickness and the width of the array elements are 130 nm and 40 μm , respectively. The bath temperature is $T_0 = 85$ K. Each laser radiates 114 mW optical power. The applied dc bias is 23.8 mA.

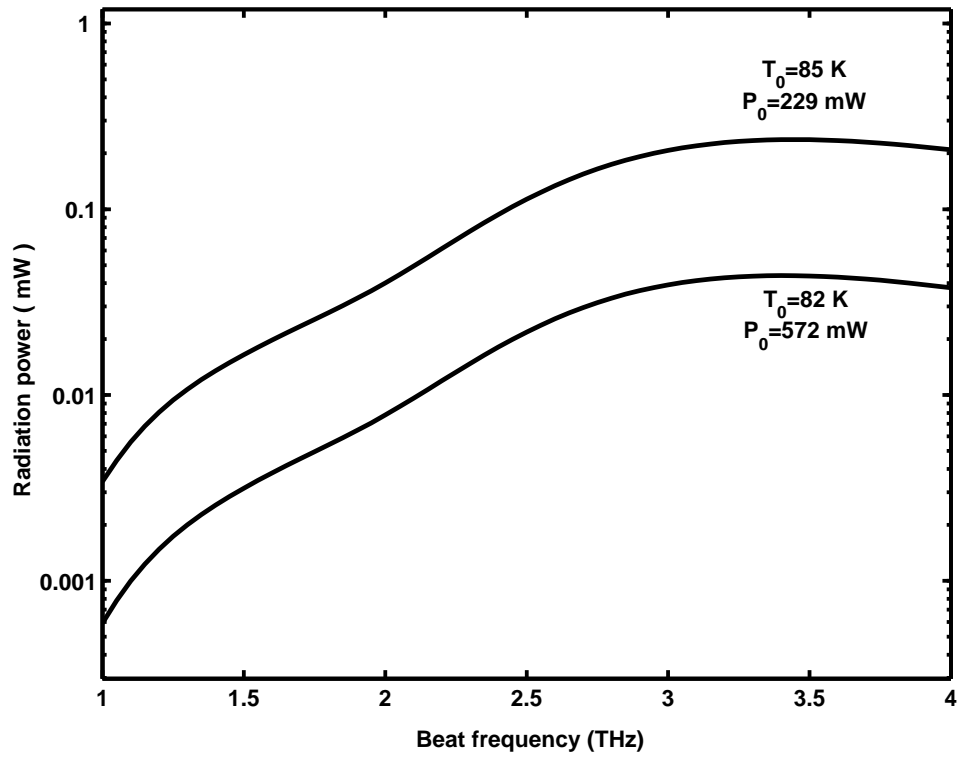


Figure 6.15: Total terahertz radiation power for an YBCO array with 61 elements versus beat frequency at two bath temperatures. The critical temperature is $T_c = 87 \text{ K}$. The thickness of the substrate changes according to the beat frequency to have maximum radiation at each frequency. The applied dc bias is 23.8 mA.

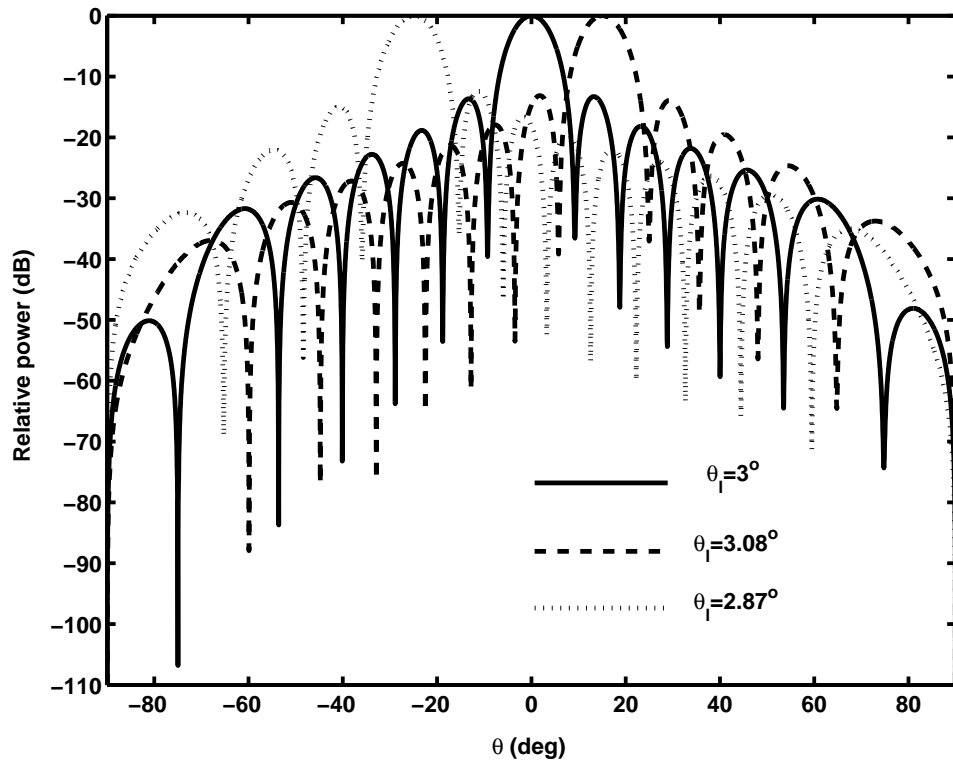


Figure 6.16: Radiation pattern of the array at $\phi = 0$ plane for different angles between the two lasers.

Chapter 7

Photomixer-Antenna Array with Integrated Excitation Scheme

In the photomixer-antenna array structures introduced in chapter 6 more than %50 of the exciting laser power either reflects back at the photomixer surface or shines the unwanted areas. Also for these structures, the configuration is very sensitive to vibration and beam directing setup. In this chapter, we propose a photoconductive photomixer-antenna array with integrated excitation scheme, in which the laser beams are guided inside the substrate and excite the photomixer elements. In this way the laser power is only being consumed by photomixer elements, and the photomixer-antenna elements can be integrated with other optical components on a single substrate. Since the excitation of the substrate waveguide can be done by optical fiber coupling, the whole structure is robust and less sensitive to vibration and other environmental parameters.

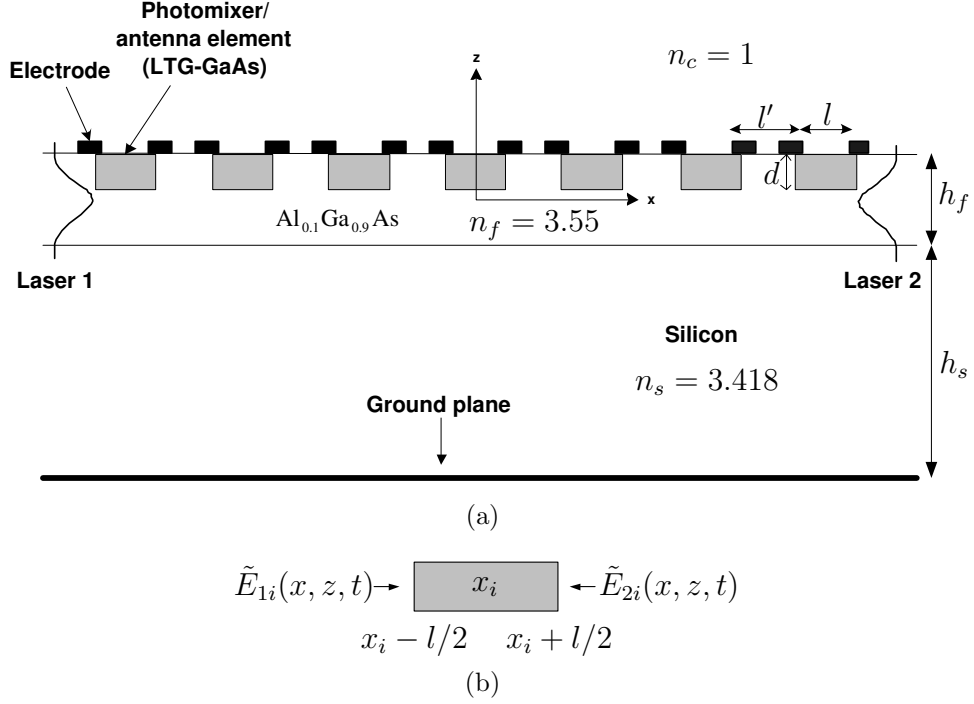


Figure 7.1: (a) A photomixer-antenna array with integrated excitation scheme. The laser beams are guided inside the core layer made of $\text{Al}_{0.1}\text{Ga}_{0.9}\text{As}$ with refractive index of $n_f = 3.55$ and excite the photomixer-antenna elements made of LTG-GaAs. (b) Electric field distribution around i -th element.

7.1 Array Design I

Fig. 7.1 shows the schematic of a photoconductive photomixer-antenna array with integrated excitation scheme. The photomixer-antenna elements are located above a grounded dielectric slab waveguide structure. The wavelengths of the lasers are around 780 nm. The laser beams are guided inside the core layer made of $\text{Al}_{0.1}\text{Ga}_{0.9}\text{As}$ with refractive index of $n_f = 3.55$ and with band gap around 1.5 eV [208]. The photomixer-antenna elements made of LTG-GaAs are buried inside the core layer. The $\text{Al}_{0.1}\text{Ga}_{0.9}\text{As}$ layer is located above a grounded dielectric layer made of silicon with refractive index of $n_s = 3.418$. Since the refractive index of

LTG-GaAs ($n_{\text{GaAs}} = 3.58$) is close to that of $\text{Al}_{0.1}\text{Ga}_{0.9}\text{As}$, we neglect any reflection from LTG-GaAs/ $\text{Al}_{0.1}\text{Ga}_{0.9}\text{As}$ interfaces, and we assume that the entire structure is a three layer asymmetric single mode slab waveguide. Although this is a good approximation for an array with limited number of elements, however, for an array with a large number of elements even a small difference in the refractive index of the waveguide and the photomixer elements may cause an inaccuracy in the results of the simulation.

The lasers' beam are launched inside the core of the waveguide structure from two sides of the waveguide and excite the photomixer-antenna elements while they travel along the length of the waveguide. The thickness of the film is designed in such a way that the waveguide becomes a single mode waveguide at the given lasers' frequencies. The electric field of the TE_0 mode corresponding to the two laser beams over the i -th element can be written as (see Fig. 7.1)

$$\tilde{E}_{1i}(x, z, t) = E_1(z)e^{-\frac{1}{2}\alpha(x-x_i+l/2)}e^{-\frac{1}{2}(i-1)\alpha l}e^{j[\omega_1 t - \beta_{1x}(x+Nl+(N+1/2)l)]} \quad (7.1)$$

$$\tilde{E}_{2i}(x, z, t) = E_2(z)e^{-\frac{1}{2}\alpha(x-x_i-l/2)}e^{-\frac{1}{2}(2N+1-i)\alpha l}e^{j[\omega_2 t - \beta_{2x}(x-Nl-(N+1/2)l)]} \quad (7.2)$$

$$x_i - l/2 \leq x \leq x_i + l/2 \quad (7.3)$$

where α is the absorption coefficient, ω_1 and ω_2 are the angular frequency of the two lasers, and β_{1x} and β_{2x} are the wavenumbers of the propagating modes, respectively. The amplitude of the two modes, $E_1(z)$ and $E_2(z)$ can be written as [209]

$$E_{1(2)}(z) = A_{1(2)} \cos(\beta_{1(2)z}z - \phi) \quad (7.4)$$

where

$$A_{1(2)} = \left[\frac{2\omega_{1(2)}\mu_0 P_{1(2)}}{W\beta_{1(2)x}h_f(1 + \frac{1}{2w} + \frac{1}{2w'})} \right]^{1/2} \quad (7.5)$$

$$\beta_{1(2)z} = [k_{1(2)}^2 n_f^2 - \beta_{1(2)x}]^{1/2} \quad (7.6)$$

$$\phi = \frac{\nu\pi}{2} + \frac{1}{2} \tan^{-1} \left(\frac{w}{u} \right) - \frac{1}{2} \tan^{-1} \left(\frac{w'}{u} \right), \quad \nu = 0, 1, \dots \quad (7.7)$$

in which $P_{1(2)}$ are the two lasers' power, W is the width of the waveguide, $k_{1(2)}$ are the two lasers' wavenumber in free space, and

$$\beta_{1(2)x} = k_{1(2)} [n_s^2 + b(n_f^2 - n_s^2)]^{1/2} \quad (7.8)$$

$$h_f = \frac{v}{\max\{k_1, k_2\} \sqrt{n_f^2 - n_s^2}} \quad (7.9)$$

$$w = v\sqrt{b} \quad (7.10)$$

$$w' = v\sqrt{b + \gamma} \quad (7.11)$$

$$u = v\sqrt{1 - b} \quad (7.12)$$

$$v = \frac{1}{2} \tan^{-1} \sqrt{\gamma} + \frac{\nu\pi}{2}, \quad \nu = 1, 2, \dots \quad (7.13)$$

$$\gamma = \frac{n_s^2 - n_c^2}{n_f^2 - n_s^2} \quad (7.14)$$

The parameter b is the normalized propagation constant, which can be calculated from the following dispersion equation [209]

$$2v\sqrt{1 - b} = \nu\pi + \tan^{-1} \sqrt{b/(1 - b)} + \tan^{-1} \sqrt{(b + \gamma)/(1 - b)} \quad (7.15)$$

where $\nu = 0, 1, 2, \dots$ is the mode number.

The optical power density inside the i -th element is proportional to the square of

the total electric field and can be written as

$$I_i(x, z, t) = \frac{n_e}{2\eta_0} \left[E_1^2(z) e^{-\alpha(x-x_i+(i-1/2)l)} + E_2^2(z) e^{\alpha(x-x_i-(2N-i+3/2)l)} \right. \\ \left. 2E_1(z)E_2(z)e^{-\alpha(N+1/2)l} \cos(\Omega t - K_x x - \Phi) \right] \quad (7.16)$$

where

$$n_e = [n_s^2 + b(n_f^2 - n_s^2)]^{1/2} \quad (7.17)$$

$$K_x = \beta_{1x} + \beta_{2x} \quad (7.18)$$

$$\Omega = \omega_1 - \omega_2 \quad (7.19)$$

$$\Phi = (\beta_{1x} - \beta_{2x}) [Nl' + (N + 1/2)l] \quad (7.20)$$

The carrier generation rate in terms of the optical power density can be written as

$$G_i(x, z, t) = \frac{\alpha}{\hbar\omega} I_i(x, z, t) \\ = G_{1i}(x, z) + G_{2i}(x, z) + \delta G(z) \cos(\Omega t - K_x x - \Phi) \quad (7.21)$$

where ω is the average of the angular frequencies of the two lasers and

$$G_{1i}(x, z) = \frac{\alpha n_e}{2\hbar\omega\eta_0} A_1^2 e^{-\alpha(x-x_i+(i-1/2)l)} \left[1 + \cos(2\beta_{1z}z - 2\phi) \right] \quad (7.22)$$

$$G_{2i}(x, z) = \frac{\alpha n_e}{2\hbar\omega\eta_0} A_2^2 e^{\alpha(x-x_i-(2N-i+3/2)l)} \left[1 + \cos(2\beta_{2z}z - 2\phi) \right] \quad (7.23)$$

$$\delta G(z) = \frac{\alpha n_e}{2\hbar\omega\eta_0} A_1 A_2 e^{-\alpha(N+1/2)l} \left[\cos((\beta_{1z} + \beta_{2z})z - 2\phi) + \cos((\beta_{1z} - \beta_{2z})z) \right] \quad (7.24)$$

By taking the average of $G_{1i}(x, z)$, $G_{2i}(x, z)$, and $\delta G(z)$ over the thickness and the length of the i -th element, one can find the effective carrier generation rate inside the i -th element as

$$\bar{G}_i(x, t) = \bar{G}_{0i} \left[1 + \eta_i \cos(\Omega t - K_x x - \Phi) \right] \quad (7.25)$$

where

$$\bar{G}_{0i} = \bar{G}_{1i} + \bar{G}_{2i} \quad (7.26)$$

$$\eta_i = \frac{\delta \bar{G}}{\bar{G}_{1i} + \bar{G}_{2i}} \quad (7.27)$$

with

$$\bar{G}_{1i} = \frac{n_e A_1^2}{4d l \hbar \omega \eta_0} e^{-\alpha(i-1)l} (1 - e^{-\alpha l}) \left[d + \frac{1}{\beta_{1z}} \sin(\beta_{1z} d) \cos(\beta_{1z}(2h_f - d) - 2\phi) \right] \quad (7.28)$$

$$\bar{G}_{2i} = \frac{n_e A_2^2}{4d l \hbar \omega \eta_0} e^{-\alpha(2N+1-i)l} (1 - e^{-\alpha l}) \left[d + \frac{1}{\beta_{2z}} \sin(\beta_{2z} d) \cos(\beta_{2z}(2h_f - d) - 2\phi) \right] \quad (7.29)$$

$$\begin{aligned} \delta \bar{G} = \frac{\alpha n_e A_1 A_2}{d \hbar \omega \eta_0} e^{-\alpha(N+1/2)l} & \left[\frac{1}{\beta_{1z} + \beta_{2z}} \sin \frac{\beta_{1z} + \beta_{2z}}{2} d \cos \left(\frac{\beta_{1z} + \beta_{2z}}{2} (2h_f - d) - 2\phi \right) \right. \\ & \left. + \frac{1}{\beta_{1z} - \beta_{2z}} \sin \frac{\beta_{1z} - \beta_{2z}}{2} d \cos \left(\frac{\beta_{1z} - \beta_{2z}}{2} (2h_f - d) \right) \right] \quad (7.30) \end{aligned}$$

The carrier generation rate given by Eq. (7.25) has the same form as Eq. (4.4), except for the term $e^{\alpha z}$. One can use the analysis given in Chapter 4 and find the generated terahertz photocurrent inside the i -th element as

$$\tilde{J}_i^s(x) = J_i^s e^{-j[K_x x + \phi_i]} \quad (7.31)$$

where

$$J_i^s = \left[(J_{1i}^s)^2 + (J_{2i}^s)^2 \right]^{1/2} \quad (7.32)$$

$$\phi_i = \Phi + \tan^{-1} \frac{J_{2i}^s}{J_{1i}^s} \quad (7.33)$$

with

$$J_{1i}^s = ed \left[v_n |\delta \hat{N}_i| \cos \phi_{ni} + v_p |\delta \hat{P}_i| \cos \phi_{pi} \right. \\ \left. + D_n K_x |\delta \hat{N}_i| \sin \phi_{ni} - D_p K_x |\delta \hat{P}_i| \sin \phi_{pi} \right] \quad (7.34)$$

$$J_{2i}^s = ed \left[-v_n |\delta \hat{N}_i| \sin \phi_{ni} - v_p |\delta \hat{P}_i| \sin \phi_{pi} \right. \\ \left. + D_n K_x |\delta \hat{N}_i| \cos \phi_{ni} - D_p K_x |\delta \hat{P}_i| \cos \phi_{pi} \right] \quad (7.35)$$

$$\delta \hat{N}_i = |\delta \hat{N}_i| e^{j\phi_{ni}} = \frac{a_{ni} + jb_{ni}}{a_i + jb_i} \eta_i \bar{G}_{0i} \quad (7.36)$$

$$\delta \hat{P}_i = |\delta \hat{P}_i| e^{j\phi_{pi}} = \frac{a_{pi} + jb_{pi}}{a_i + jb_i} \eta_i \bar{G}_{0i} \quad (7.37)$$

$$a_{n[p]i} = \tau_{p[n]}^{-1} + D_{p[n]} K_x^2 + \frac{e}{\epsilon} (\mu_n \bar{N}_{0i} + \mu_p \bar{P}_{0i}) \quad (7.38)$$

$$b_{n[p]i} = \Omega - \mu_{p[n]} E_0 K_x \quad (7.39)$$

$$a_i = a_{ni} a_{pi} - b_{ni} b_{pi} - \frac{e}{\epsilon} [\mu_p a_{ni} \bar{P}_{0i} + \mu_n a_{pi} \bar{N}_{0i}] \quad (7.40)$$

$$b_i = a_{pi} b_{ni} + a_{ni} b_{pi} - \frac{e}{\epsilon} [\mu_p b_{ni} \bar{P}_{0i} + \mu_n b_{pi} \bar{N}_{0i}] \quad (7.41)$$

$$\bar{N}_{0i} [\bar{P}_{0i}] = \bar{N}_{01i} [\bar{P}_{01i}] + \bar{N}_{02i} [\bar{P}_{02i}] \quad (7.42)$$

The parameters \bar{N}_{01i} , \bar{N}_{02i} , \bar{P}_{01i} , and \bar{P}_{02i} can be calculated from the equations given in Appendix A, where G_0 is replaced by \bar{G}_{1i} to calculate \bar{N}_{01i} and \bar{P}_{01i} , and is replaced by \bar{G}_{2i} to calculate \bar{N}_{02i} and \bar{P}_{02i} .

The terahertz photocurrent distribution given by Eq. (7.31) has the same form as that of Eq. (6.26). The radiation power can be calculated by Eqs. (6.31) to (6.33). The length of the elements and the separation distance between the elements are equal and are given by

$$l = l' = \frac{\pi}{K_x} \quad (7.43)$$

7.2 Simulation Results

An array with 19 elements is considered. The physical parameters of the LTG-GaAs material are given in Table 3.1. The thickness of the core layer, h_f , for single mode operation at 780 nm is $0.573 \mu\text{m}$. The thickness of the substrate, h_s , at the frequency of 1 THz is $22.4 \mu\text{m}$. The grating vector, K_x , at the frequency of 1 THz is $56.5 (\mu\text{m})^{-1}$. From Eq. (7.43), the length of the array elements at the frequency of 1 THz is 55.6 nm. The width of the array elements is $100 \mu\text{m}$. The dc bias voltage over each element is 0.139 V. The optical power coupled to the waveguide from each of the lasers is 100 mW.

Fig. 7.2 shows the radiation power versus beat frequency for different values of the thickness of the photomixer-antenna elements. The thickness of the substrate is changed according to the beat frequency to have maximum radiation at each frequency. The radiation power increases by increasing the thickness of the photomixer-antenna elements.

Fig. 7.3 shows the absorbed optical power in each element for the array elements with the thickness of $0.573 \mu\text{m}$ working at 1 THz. The length of the array elements is very small, which limits the maximum consumable optical power in each element. It also makes it difficult to fabricate the designed array. High value of the grating vector given by Eq. (7.18) results in a small value for the length of the

array elements. In the next section we analyze an array configuration, in which the two laser beams are launched from one side of the optical waveguide. In this configuration, the resulting grating vector is equal to the subtraction of the two propagation constants of the two beams inside the waveguide, which results in the resonant length of the array elements in the order of $40 \mu\text{m}$.

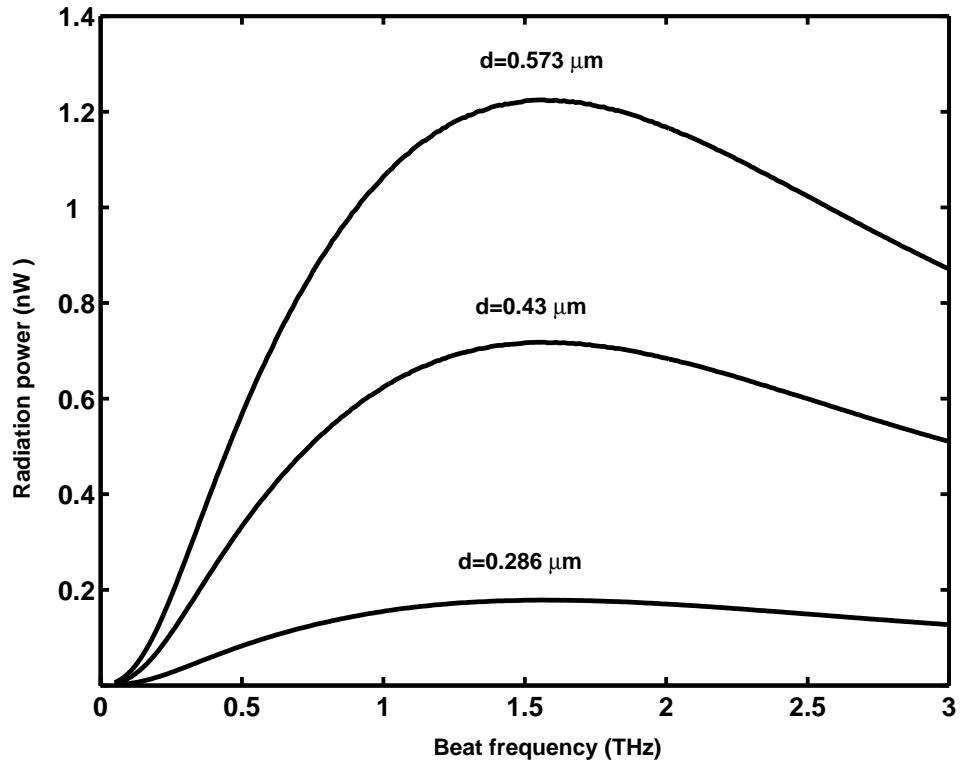


Figure 7.2: Terahertz radiation power versus beat frequency for different values of the thickness of the photomixer-antenna elements. The number of array elements is 19. The thickness of the core layer is $h_f = 0.573 \mu\text{m}$. The thickness of the substrate at the frequency of 1 THz is $h_s = 22.4 \mu\text{m}$. The length of the array elements at the frequency of 1 THz is 55.6 nm. The width of the array elements is $100 \mu\text{m}$. The dc bias voltage over each element is 0.139 V. The optical power coupled to the waveguide from each of the lasers is 100 mW.

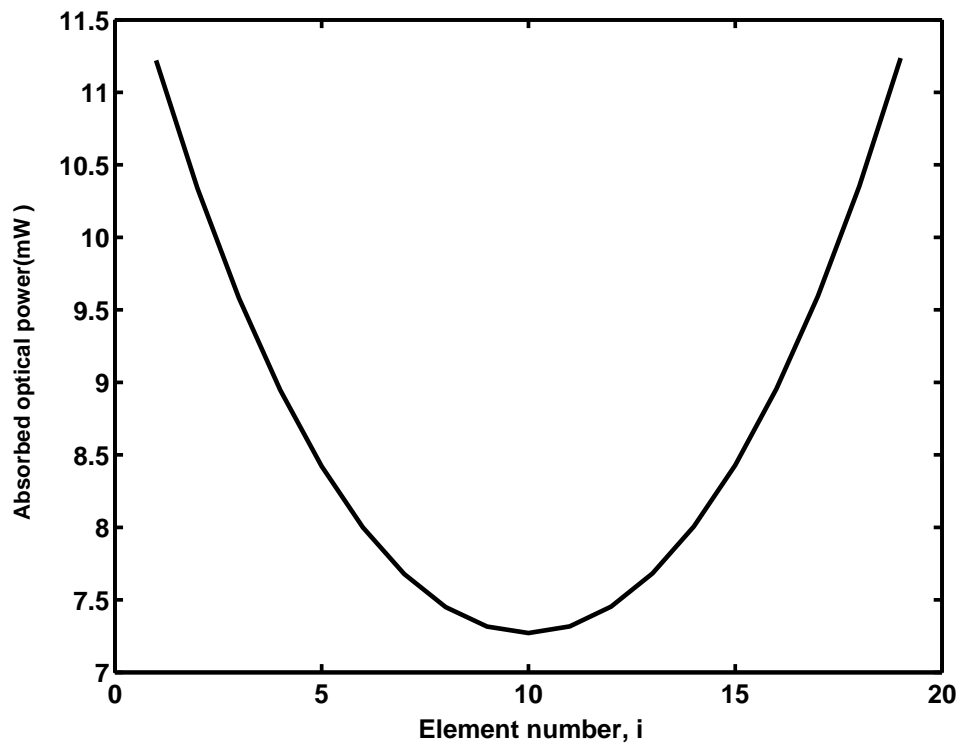


Figure 7.3: Absorbed optical power in each element.

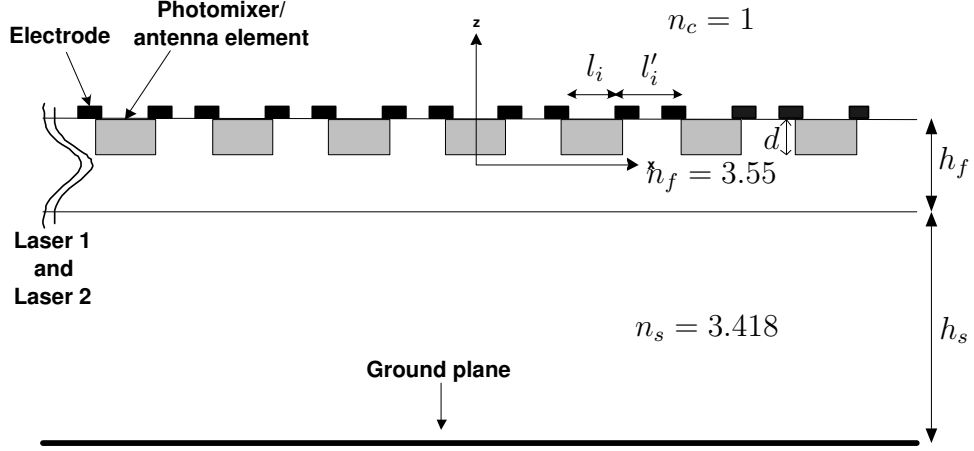


Figure 7.4: A photomixer-antenna array with integrated excitation scheme: two laser beams are launched from one side of the optical waveguide.

7.3 Array Design II

In this section we consider a photomixer-antenna array as shown in Fig. 7.4, where the two laser beams are launched from the left side of the waveguide. In this case the electric field of the TE_0 mode corresponding to the two laser beams over the i -th element can be written as

$$\tilde{E}_{1(2)i}(x, z, t) = E_{1(2)}(z) e^{-\frac{1}{2}\alpha(x-x_i+l_i^t+l_i/2)} e^{j[\omega_{1(2)}t-\beta_{1(2)x}(x+x_0)]} \quad (7.44)$$

where $E_{1(2)}(z)$ are given by Eq. (7.4), $\beta_{1(2)x}$ are given by Eq. (7.8), and

$$l_i^t = \sum_{n=1}^{i-1} l_n \quad (7.45)$$

$$x_0 = \sum_{n=1}^N (l_n + l'_n) + \frac{l_{N+1}}{2} \quad (7.46)$$

The optical power density inside the i -th element can be written as

$$I_i(x, z, t) = \frac{n_e}{2\eta_0} e^{-\alpha(x-x_i+l_i^t+l_i/2)} \left[E_1^2(z) + E_2^2(z) + 2E_1(z)E_2(z) \cos(\Omega t - K_x x - \Phi) \right] \quad (7.47)$$

where

$$K_x = \beta_{1x} - \beta_{2x} \quad (7.48)$$

$$\Omega = \omega_1 - \omega_2 \quad (7.49)$$

$$\Phi = (\beta_{1x} - \beta_{2x})x_0 \quad (7.50)$$

The effective carrier generation rate inside the i -th element can be written as

$$\bar{G}_i(x, t) = \bar{G}_{0i} \left[1 + \eta_i \cos(\Omega t - K_x x - \Phi) \right] \quad (7.51)$$

where $\bar{G}_{0i} = \bar{G}_{1i} + \bar{G}_{2i}$ and $\eta_i = \frac{\delta \bar{G}_i}{\bar{G}_{1i} + \bar{G}_{2i}}$ with

$$\bar{G}_{1(2)i} = \frac{n_e A_{1(2)}^2}{4dl_i \hbar \omega \eta_0} e^{-\alpha l_i^t} (1 - e^{-\alpha l_i}) \left[d + \frac{1}{\beta_{1(2)z}} \sin(\beta_{1(2)z} d) \cos(\beta_{1(2)z} (2h_f - d) - 2\phi) \right] \quad (7.52)$$

$$\begin{aligned} \delta \bar{G}_i = & \frac{n_e A_1 A_2}{dl_i \hbar \omega \eta_0} e^{-\alpha l_i^t} (1 - e^{-\alpha l_i}) \\ & \left[\frac{1}{\beta_{1z} + \beta_{2z}} \sin\left(\frac{\beta_{1z} + \beta_{2z}}{2} d\right) \cos\left(\frac{\beta_{1z} + \beta_{2z}}{2} (2h_f - d) - 2\phi\right) \right. \\ & \left. + \frac{1}{\beta_{1z} - \beta_{2z}} \sin\left(\frac{\beta_{1z} - \beta_{2z}}{2} d\right) \cos\left(\frac{\beta_{1z} - \beta_{2z}}{2} (2h_f - d)\right) \right] \quad (7.53) \end{aligned}$$

One can calculate the generated terahertz photocurrent inside the i -th element using Eqs. (7.31)-(7.42) and the radiation power using Eqs. (6.31)-(6.33).

For this design, the resonant length of the array elements given by Eq. (7.43) is in the order of $40 \mu\text{m}$. One has to choose the lengths of the array elements in such a way that the consumed optical power in each element becomes less than the maximum sustainable power by that element. In other words, the lengths of the array elements will be much less than the resonant length. We design the lengths of the array elements to have equal absorbed optical power in each element.

Fig. 7.5 shows the power flow diagram along the array structure. For equal absorbed optical power inside the i -th and the $(i + 1)$ -th elements one can write

$$P_i^{in} - P_i^{out} = P_{i+1}^{in} - P_{i+1}^{out} \quad (7.54)$$

where

$$P_i^{out} = P_i^{in} e^{-\alpha l_i} \quad (7.55)$$

$$P_{i+1}^{out} = P_{i+1}^{in} e^{-\alpha l_{i+1}} \quad (7.56)$$

Substituting Eqs. (7.55) and (7.56) into Eq. (7.54) results in

$$l_{i+1} = -\frac{1}{\alpha} \ln(2 - e^{\alpha l_i}), \quad i = 1, 2, \dots, 2N + 1 \quad (7.57)$$

Eq. (7.57) is valid for $l_i < \frac{1}{\alpha} \ln 2$.

The length of the first element, l_1 can be calculated from

$$(Wl_1)P_{max} = (1 - e^{-\alpha l_1})P_0 \quad (7.58)$$

where W is the width of the array elements, P_{max} is the maximum sustainable optical power by the photomixer-antenna elements in W/m^2 , and P_0 is the total

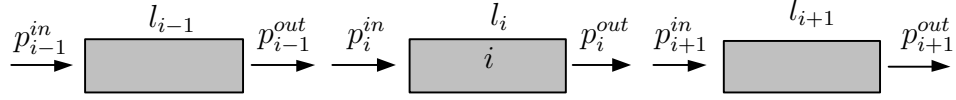


Figure 7.5: Power flow diagram along the array structure.

input optical power.

7.4 Simulation Results

An array with 5 elements is designed. The thickness of the core layer, h_f , for single mode operation at 780 nm is $0.573 \mu\text{m}$. The thickness of the substrate, h_s , at the frequency of 1 THz is $22.4 \mu\text{m}$. The grating vector, K_x , at the frequency of 1 THz is $0.0735 (\mu\text{m})^{-1}$. The optical power of each laser is 100 mW. Assuming the maximum sustainable optical power by each element is $0.9 \text{ mW}/\mu\text{m}^2$, the lengths of the array elements can be calculated from Eqs. (7.57) and (7.58) as 220 nm, 282 nm, 395 nm, 663 nm, and $2.814 \mu\text{m}$. The thickness and the width of the array elements are $0.573 \mu\text{m}$ and $200 \mu\text{m}$, respectively. The absorbed optical in each element is 39.5 mW. The applied electric field over each element is $2.5 \text{ V}/\mu\text{m}$.

Fig. 7.6 shows radiation power versus beat frequency. The thickness of the substrate is changed according to the beat frequency to have maximum radiation at each frequency.

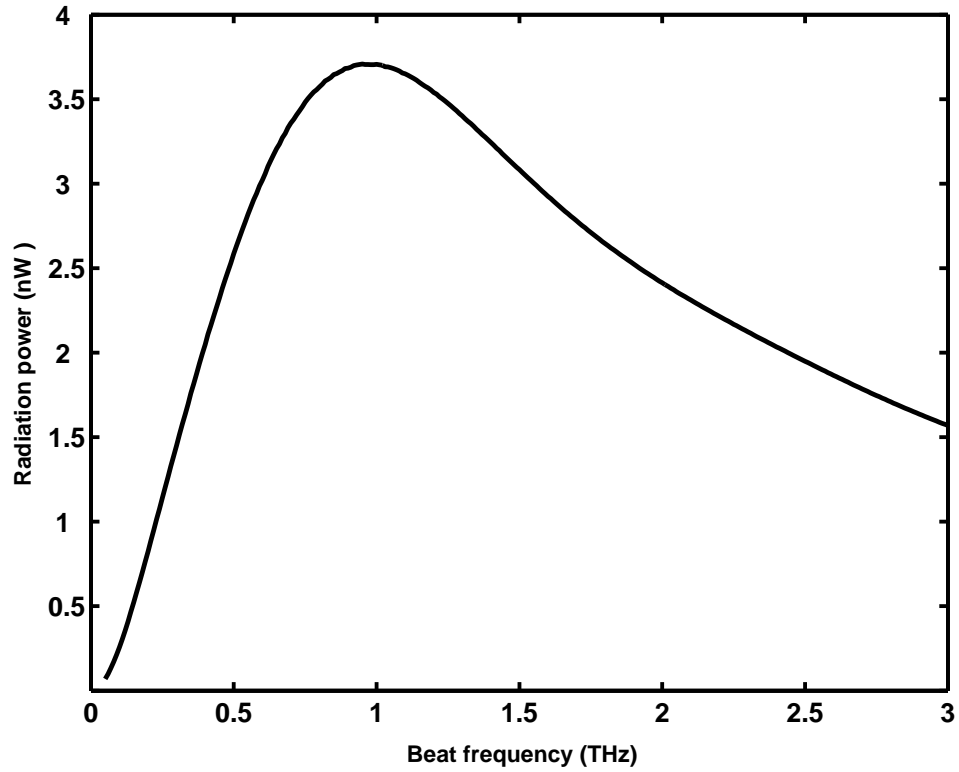


Figure 7.6: Terahertz radiation power versus beat frequency for an array with 5 elements. The thickness of the core layer is $h_f = 0.573 \mu\text{m}$. The thickness of the substrate at the frequency of 1 THz is , $h_s = 22.4 \mu\text{m}$. The optical power of each laser is 100 mW. The lengths of the array elements are 220 nm, 282 nm, 395 nm, 663 nm, and $2.814 \mu\text{m}$. The thickness and the width of the array elements are $0.573 \mu\text{m}$ and $200 \mu\text{m}$, respectively. The absorbed optical in each element is 39.5 mW. The applied electric field over each element is $2.5 \text{ V}/\mu\text{m}$.

Chapter 8

Concluding Remarks

8.1 Summary and Contributions

The photomixing phenomenon in superconductors has been studied in detail. The analytic expression for the generated photocurrent inside a superconductor film excited by two CW laser beams has been derived using the fundamental carrier transport equations for the superconductor material. The two-temperature model has been used to find the spatiotemporal distribution of the electron and phonon temperatures due to the interfering laser beams inside the superconductor film. The resulting electron and phonon temperatures as well as the amplitude and the phase of the generated photocurrent for an HTS photomixer have been analyzed and their dependencies on the bath temperature, the beat frequency, and the angle between the two laser beams have been explored.

The interaction of the laser and the photoconductor in a typical photomixing scheme has been studied. The continuity equations for the carriers have been solved in their general form for a photomixing configuration, in which two CW

laser beams excite a dc biased photoconductor. A general analytical expression for the photocurrent has been derived. The dependencies of the generated terahertz photocurrent on the physical parameters as well as the photomixer configuration have been explored. The saturation behavior of the terahertz photocurrent with the applied dc bias has been explored. The developed models can be used for designing and optimization of terahertz sources.

A terahertz photoconductive photomixer-antenna device based on the integration of a photomixer and an antenna element has been proposed. Two longitudinal and transversal schemes, in which the optical illumination planes are respectively parallel and normal to the direction of the applied bias, are investigated in detail. The analytic expressions for the photocurrent distribution and the radiation power have been derived for both configurations. The generated photocurrent inside the photoconductor film acts as a radiation source and by choosing proper values for the dimensions of the antenna configuration, the proposed structure radiates out the terahertz power to the free space.

A continuous-wave terahertz photomixer array source made of LTG-GaAs has been designed and analyzed. It has been shown that a few micro-watt terahertz power is achievable from a typical array source at 1 THz. The dependency of the radiation power on the beat frequency and the applied dc bias has been studied. It also has been shown that the radiation beam can be steered over more than $\pm 30^\circ$ by changing the angle between the two exiting laser beams.

A terahertz photomixer-antenna array source made of $\text{YBa}_2\text{Cu}_3\text{O}_{7-\delta}$ thin film has been designed and analyzed. It has been shown that a sub-milliwatt terahertz power is achievable from a typical array structure. It also has been shown that the radiation beam can be steered more than $\pm 20^\circ$ by changing the angle between the two exiting laser beams.

Two terahertz photomixer-antenna array configurations with integrated optical excitation have been designed and simulation results are presented. In the proposed structures, the laser beams are guided inside the substrate and excite the photomixer elements. It has been shown that a few nW terahertz power can be achieved using two lasers with 100 mW output power.

The proposed devices are attractive for the terahertz applications, including terahertz spectroscopy and sensing, terahertz imaging, and local oscillators in terahertz heterodyne receivers.

8.2 Future Work

Followings are some possible directions for the further research work:

- **Fabrication and test of the proposed photomixer sources**
- **Looking for low-cost solutions for photomixer sources**

One of the ideas can be using light emitting diodes (LEDs) instead of lasers in photomixers to lower their complexity and cost. LEDs are cheaper than lasers and do not need temperature and current controlling systems. The challenging problems with LEDs are their wide line-width, phase noise, and random output polarization.

Most of the developed photoconductive photomixers are made of LTG-GaAs and use lasers with wavelengths from 750 nm to 850 nm. Some researchers are working on new compositions suitable for photomixing at 1310 nm-1550 nm optical telecommunication wavelengths, for which lasers, detectors, and variety of other optical components are commercially available at relatively lower costs. The two most promising materials are InGaAs containing ErAs

particles and GaSb containing ErSb nanoparticles. Realization of a terahertz photomixer working at the optical telecommunication wavelengths is a great success from both technology and cost point of view.

Another low-cost solution can be looking at possibility of using polymers as mixing media in photomixers. Polymers can be produced and implemented relatively easier than high-quality photoconductors, and if one can use them as mixing media in a photomixer, the overall cost will drastically decrease.

- **Using electromagnetic band gap (EBG) structures in photomixers**

EBG structures can be incorporated into the photomixer-antenna devices to suppress substrate modes and increase their efficiencies. There are also interesting reports on terahertz sources with guided schemes, which suffer from high metallic loss in their waveguiding sections. Using EBGs as guiding medium for generated terahertz signals can be a solution to this problem.

- **Studying the effects of the lasers' characteristics on the performance of a photomixer**

The frequency spectrum of the generated signal in a photomixer is a function of the frequency spectrum and the phase noise of the exciting lasers. Using the developed model for photomixers, one can study the effects of finite line-width and phase noise of the exciting lasers on the performance of photomixers.

Appendix A

Calculation of the Carrier Densities N_0 and P_0

To find N_0 and P_0 , one has to solve the nonlinear coupled equation set given by Eqs. (4.24) and (4.25). The resulting equation for N_0 is

$$\kappa_1 N_0^3 + \kappa_2 N_0^2 + \kappa_3 N_0 + \kappa_4 = 0 \quad (\text{A.1})$$

where

$$\kappa_1 = -\frac{e}{\epsilon} \frac{1}{\alpha d} (1 - e^{-\alpha d}) \left[\eta_p \mu_p \tau_p + \eta_n \mu_n \tau_n \right] \quad (\text{A.2})$$

$$\kappa_2 = (\mu_n + \mu_p) \eta_n \eta_p \frac{e}{\epsilon} \frac{1}{\alpha d} (1 - e^{-\alpha d}) \tau_n \tau_p G_0 - \frac{\eta_p \mu_p \tau_p}{\eta_n \mu_n \tau_n} - 1 \quad (\text{A.3})$$

$$\kappa_3 = \left(\frac{2\eta_p \mu_p \tau_p}{\mu_n} + \tau_n \eta_n \right) G_0 \quad (\text{A.4})$$

$$\kappa_4 = -\frac{\mu_p}{\mu_n} \tau_n \tau_p \eta_n \eta_p G_0^2 \quad (\text{A.5})$$

with $\eta_n = 1/(1 - \alpha^2 L_n^2)$ and $\eta_p = 1/(1 - \alpha^2 L_p^2)$.

One can find P_0 in terms of N_0 as

$$P_0 = \frac{1}{\tau_n \mu_n \frac{\epsilon}{\alpha d} (1 - e^{-\alpha d})} \left(\tau_n \mu_n \frac{\epsilon}{\alpha} \bar{N}_0 + \eta_n^{-1} - \frac{\tau_n G_0}{N_0} \right) \quad (\text{A.6})$$

An approximate solution to Eqs. (4.24) and (4.25) is

$$N_0 = \frac{\tau_n G_0}{1 - \alpha^2 \tau_n D_n} \approx \tau_n G_0 \quad (\text{A.7})$$

$$P_0 = \frac{\tau_p G_0}{1 - \alpha^2 \tau_p D_p} \approx \tau_p G_0 \quad (\text{A.8})$$

Publications

Journal articles

- [1] D. Saeedkia, R. R. Mansour, and S. Safavi-Naeini “The interaction of laser and photoconductor in a continuous-wave terahertz photomixer,” *IEEE J. Quantum Elec.*, Vol. 41, No. 9, pp. 1188-1196, September 2005.
- [2] D. Saeedkia, R. R. Mansour, and S. Safavi-Naeini “Modeling and Analysis of High-Temperature Superconductor terahertz Photomixers,” *IEEE Trans. Appl. Superconduct.*, Vol. 15, No. 3, September 2005.
- [3] D. Saeedkia, R. R. Mansour, and S. Safavi-Naeini “A Sub-Milliwatt Terahertz High-Temperature Superconductive Photomixer Array Source: Analysis and Design,” *IEEE Trans. Appl. Superconduct.*, Vol. 15, No. 4, September 2005.
- [4] D. Saeedkia, A. H. Majedi, S. Safavi-Naeini, and R. R. Mansour, “Analysis and design of photoconductive integrated photomixer/antenna for THz applications,” *IEEE J. Quantum Elec.*, Vol. 41, No. 2, pp. 234-241, February 2005.
- [5] D. Saeedkia, R. R. Mansour, and S. Safavi-Naeini “Analysis of a Photoconductive Photomixer Array Source Designed for Terahertz Applications,” *IEEE Trans. Antennas Propagat.*, in press.
- [6] D. Saeedkia, A. H. Majedi, S. Safavi-Naeini, and R. R. Mansour, “High-Temperature Superconductive Photomixer Patch Antenna: Theory and Design,” Special Issue on Recent Progress in Microwave and Millimeter-wave Photonics Technology, *IEICE Trans. Electron.*, Vol. E86-C, No.7, pp. 1318-1327, July 2003.

- [7] D. Saeedkia, A. H. Majedi, S. Safavi-Naeini, and R. R. Mansour, "Frequency- and Time-Varying Scattering Parameters of a Photo-Excited Superconducting Microbridge," *IEEE Microwave Wireless Comp. Lett.*, Vol. 15, No. 8, pp. 510-512, August 2005.
- [8] A. H. Majedi, D. Saeedkia, S. K. Chaudhuri, and S. Safavi-Naeini, "Physical Modeling and Frequency Response Analysis of A High-Temperature Superconducting THz Photomixer," *IEEE Trans. Microwave Theory Tech.*, Vol. 52, No. 10, pp. 2430-2437, October 2004. Special Issue on Terahertz Electronics.

Refereed conference papers

- [1] D. Saeedkia, A. H. Majedi, S. Safavi-Naeini, and R. R. Mansour, "CW Photoconductive Photomixer/Antenna Array Source for THz Applications," IEEE International Topical Meeting on Microwave Photonics, Ogunquit, Maine, USA, October 2004. *MWP'04 Technical Digest*, October 2004, PP. 317-320.
- [2] D. Saeedkia, A. H. Majedi, S. Safavi-Naeini, and R. R. Mansour, "Photomixing properties of high-temperature superconductors and photoconductors: analysis and comparison," presented at the SPIE International Symposium Photonics North, September 2004, Ottawa, Canada. *Optical Components and Devices, Proceedings of SPIE*, Volume 5577, PP. 648-658.
- [3] D. Saeedkia, A. H. Majedi, S. Safavi-Naeini, and R. R. Mansour, "A CW Photoconductive Integrated Photomixer/Antenna THz Source," SPIE Photonics West Symposium 2004, San Jose, California, USA. *Terahertz and Gigahertz Electronics and Photonics III, Proceedings of SPIE*, Volume 5354, PP. 94-103.

- [4] D. Saeedkia, A. H. Majedi, S. Safavi-Naeini, and R. R. Mansour, "A novel concept for integrated high-temperature superconductive photomixer patch antenna," International Superconducting Electronics Conference, 2003, Sydney, Australia.
- [5] D. Saeedkia, S. Safavi-Naeini, and R. R. Mansour, "A Photoconductor Photomixer Array Source with Integrated Excitation," Joint 30th International Conference on Infrared and Millimeter Waves and 13th International Conference on Terahertz Electronics, Virginia, USA, September 2005, to be presented.
- [6] D. Saeedkia, S. Safavi-Naeini, and R. R. Mansour, "A High-Temperature Superconductor Photomixer/Antenna Array Source for Terahertz Applications," Joint 30th International Conference on Infrared and Millimeter Waves and 13th International Conference on Terahertz Electronics, Virginia, USA, September 2005, to be presented.
- [7] D. Saeedkia, S. Safavi-Naeini, and R. R. Mansour, "Modeling of High-Temperature Superconductor Terahertz Photomixers," Joint 30th International Conference on Infrared and Millimeter Waves and 13th International Conference on Terahertz Electronics, Virginia, USA, September 2005, to be presented.
- [8] D. Saeedkia, S. Safavi-Naeini, and R. R. Mansour, "Modeling of Photoconductor Terahertz Photomixers," Joint 30th International Conference on Infrared and Millimeter Waves and 13th International Conference on Terahertz Electronics, Virginia, USA, September 2005, to be presented.

Bibliography

- [1] P. H. Siegel, “Terahertz Technology in Biology and Medicine,” *IEEE Trans. Microwave Theory Tech.*, vol. 52, no. 10, pp. 2438–2447, 2004.
- [2] T. W. Crowe, T. Globus, D. L. Woolard, and J. L. Hesler, “Terahertz sources and detectors and their application to biological sensing,” *Phil. Trans. R. Soc. Lond. A*, vol. 362, no. 1815, pp. 365–377, 2004.
- [3] P. H. Bolivar, M. Nagel, F. Richter, M. Brucherseifer, H. Kurz, A. Bosserhoff, and R. Buttner, “Label-free THz sensing of genetic sequences: towards THz biochips,” *Phil. Trans. R. Soc. Lond. A*, vol. 362, no. 1815, pp. 323–335, 2004.
- [4] T. Globus, D. Woolard, M. Bykhovskaia, B. Gelmont, L. Werbos, and A. Samuels, “THz-frequency spectroscopic sensing of DNA and related biological materials,” *International Journal of High Speed Electronics and Systems*, vol. 13, no. 4, pp. 903–936, 2003.
- [5] M. R. Scarfi, M. Romano, R. Dipietro, O. Zeni, A. Doria, G. P. Gallerano, E. Giovenale, G. Messina, A. Lai, G. Campurra, D. Coniglio, and M. D’Arienzo, “THz Exposure of Whole Blood for the Study of Biological Effects on Human Lymphocytes,” *J. Biol. Phys.*, vol. 29, pp. 171–175, 2003.

- [6] S. W. Smye, J. M. Chamberlain, A. J. Fitzgerald, and E. Berry, “The interaction between terahertz radiation and biological tissue,” *Phys. Med. Biol.*, vol. 46, pp. R101–R112, 2001.
- [7] S. Wang, B. Ferguson, D. Abbott, and X.-C. Zhang, “T-ray imaging and tomography,” *J. Biol. Phys.*, vol. 29, no. 2-3, pp. 247–256, 2003.
- [8] D. M. Mittleman, R. H. Jacobsen, and M. C. Nuss, “T-Ray Imaging,” *IEEE J. Sel. Top. Quantum Electron.*, vol. 2, no. 3, pp. 679–692, 1996.
- [9] B. B. Hu and M. C. Nuss, “Imaging with terahertz waves,” *Opt. Lett.*, vol. 20, no. 16, pp. 1716–1718, 1995.
- [10] M. Naftaly, A. P. Foulds, R. E. Miles, and A. G. Davies, “Terahertz Transmission Spectroscopy of Nonpolar Materials and Relationship with Composition and Properties,” *Int. J. Infrared Millim. Waves*, vol. 26, no. 1, pp. 55–64, 2005.
- [11] Y. Watanabe, K. Kawase, T. Ikari, H. Ito, Y. Ishikawa, and H. Minamide, “Component analysis of chemical mixtures using terahertz spectroscopic imaging,” *Opt. Commun.*, vol. 234, no. 1-6, pp. 125–129, 2004.
- [12] E. R. Brown, J. Bjarnason, T. L. J. Chan, D. C. Driscoll, M. Hanson, and A. C. Gossard, “Room temperature, THz photomixing sweep oscillator and its application to spectroscopic transmission through organic materials,” *Rev. Sci. Instrum.*, vol. 75, no. 12, pp. 5333–5342, 2004.
- [13] T. L. J. Chan, J. E. Bjarnason, A. W. M. Lee, M. A. Celis, and E. R. Brown, “Attenuation contrast between biomolecular and inorganic materials at terahertz frequencies,” *Appl. Phys. Lett.*, vol. 85, no. 13, pp. 2523–2525, 2004.

- [14] J. Darmo, T. Muller, W. Parz, J. Kroll, G. Strasser, and K. Unterrainer, “Few-cycle terahertz generation and spectroscopy of nanostructures,” *Phil. Trans. R. Soc. Lond. A*, vol. 362, no. 1815, pp. 251–262, 2004.
- [15] D. Mittleman, Ed., *Sensing with Terahertz Radiation*. Springer-Verlag, 2003.
- [16] M. C. Beard, G. M. Turner, and C. A. Schmuttenmaer, “Terahertz Spectroscopy,” *J. Phys. Chem. B*, vol. 106, pp. 7146–7159, 2002.
- [17] P. F. Taday, “Applications of terahertz spectroscopy to pharmaceutical sciences,” *Phil. Trans. R. Soc. Lond. A*, vol. 362, no. 1815, pp. 351–364, 2004.
- [18] V. P. Wallace, P. F. Taday, A. J. Fitzgerald, R. M. Woodward, J. Cluff, R. J. Pye, and D. D. Arnone, “Terahertz pulsed imaging and spectroscopy for biomedical and pharmaceutical applications,” *Faraday Discuss.*, vol. 126, pp. 255–263, 2004.
- [19] N. Karpowicz, H. Zhong, C. Zhang, K.-I. Lin, J.-S. Hwang, J. Xu, and X.-C. Zhang, “Compact continuous-wave subterahertz system for inspection applications,” *Appl. Phys. Lett.*, vol. 86, no. 5, pp. 54105–3, 2005.
- [20] M. K. Choi, A. Bettermann, and D. W. Van Der Weide, “Potential for detection of explosive and biological hazards with electronic terahertz systems,” *Phil. Trans. R. Soc. Lond. A*, vol. 362, no. 1815, pp. 337–349, 2004.
- [21] M. C. Kemp, P. F. Taday, B. E. Cole, J. A. Cluff, A. J. Fitzgerald, and W. R. Tribe, “Security applications of terahertz technology,” in *The Proceedings of SPIE Conference*, vol. 5070, August 2003, pp. 44–52.

- [22] D. Woolard, R. Kaul, R. Suenram, A. Hight Walker, T. Globus, and A. Samuels, "Terahertz Electronics for Chemical and Biological Warfare Agent Detection," in *IEEE MTT-S Int. Microwave Symp. Dig.*, 1999, pp. 925–928.
- [23] T. Nagatsuma, "Millimeter-Wave Photonic Technologies for Communications and Sensor Applications," in *New Photonics Technologies for the Information Age: The Dream of Ubiquitous Services*, pp. 193–212, ed. by S. Sudo and K. Okamoto (Artech House, 2004).
- [24] C. M. Mann, "Towards Terahertz Communications Systems," in *Terahertz Sources and Systems*, pp. 261–267, ed. by R. E. Miles, P. Harrison, and D. Lippens (Kluwer Academic Publisher, Printed in the Netherlands, 2001).
- [25] A. Hirata, H. Ishii, and T. Nagatsuma, "Design and characterization of a 120-GHz millimeter-wave antenna for integrated photonic transmitters," *The Proceedings of International Topical Meeting on Microwave/Photonics*, pp. 229–232, 2000.
- [26] D. Steer, G. Dolman, and P. Row, "Radio system design for broadband residential access," in *IEEE Radio and Wireless Conference*, Aug. 1999, pp. 31–34.
- [27] A. J. Fitzgerald, E. Berry, N. N. Zinovev, G. C. Walker, M. A. Smith, and J. M. Chamberlain, "An introduction to medical imaging with coherent terahertz frequency radiation," *Phys. Med. Biol.*, vol. 47, pp. R67–R84, 2002.
- [28] P. Knobloch, C. Schildknecht, T. Kleine-Ostmann, M. Koch, S. Hoffmann, M. Hofmann, E. Rehberg, M. Sperling, K. Donhuijsen, G. Hein, and K. Pierz, "Medical THz imaging: an investigation of histopathological samples," *Phys. Med. Biol.*, vol. 47, no. 21, pp. 3875–3884, 2002.

- [29] A. J. Fitzgerald, E. Berry, N. N. Zinovev, S. H. Vanniasinkam, R. E. Miles, J. M. Chamberlain, and M. A. Smith, “Catalogue of Human Tissue Optical Properties at Terahertz Frequencies,” *J. Biol. Phys.*, vol. 129, pp. 123–128, 2003.
- [30] J.-I. Nishizawa, T. Sasaki, K. Suto, T. Yamada, T. Tanabe, T. Tanno, T. Sawai, and Y. Miura, “THz imaging of nucleobases and cancerous tissue using a GaP THz-wave generator,” *Opt. Commun.*, vol. 244, no. 1-6, pp. 469–474, 2005.
- [31] E. Pickwell, B. E. Cole, A. J. Fitzgerald, M. Pepper, and V. PWallace, “In vivo study of human skin using pulsed terahertz radiation,” *Phys. Med. Biol.*, vol. 49, pp. 1595–1607, 2004.
- [32] V. P. Wallace, A. J. Fitzgerald, S. Shankar, N. Flanagan, R. Pye, J. Cluff, and D. D. Arnone, “Terahertz pulsed imaging of basal cell carcinoma ex vivo and in vivo,” *Brit. J. Dermatol.*, vol. 151, pp. 424–432, 2004.
- [33] R. M. Woodward, V. P. Wallace, R. J. Pye, B. E. Cole, D. D. Arnone, E. H. Linfield, and M. Pepper, “Terahertz Pulse Imaging of ex vivo Basal Cell Carcinoma,” *The Journal of Investigative Dermatology*, vol. 120, no. 1, pp. 72–78, January 2003.
- [34] D. A. Crawley, C. Longbottom, B. Cole, C. M. Ciesla, D. Arnone, V. Wallace, and M. Pepper, “Terahertz pulse imaging: A pilot study of potential applications in dentistry ,” *Caries Res.*, vol. 37, no. 5, pp. 352–359, 2003.
- [35] N. N. Zinovev, A. F. Fitzgerald, S. M. Strafford, D. J. Wood, F. A. Carmichael, R. E. Miles, M. A. Smith, and J. M. Chamberlain, “Identification of tooth decay using terahertz imaging and spectroscopy,” in *Twenty*

Seventh International Conference on Infrared and Millimeter Waves, Sept. 2002, pp. 13–14.

- [36] M. C. Teich, “Field-Theoretical Treatment of Photomixing,” *Appl. Phys. Lett.*, vol. 14, no. 6, pp. 201–203, 1969.
- [37] Jack Soohoo, S.-K. Yao, J. E. Miller, R. R. Shurtz, Y. Taur, and R. A. Gudmundsen, “A Laser-Induced Traveling-Wave Device for Generating Millimeter Waves,” *IEEE Trans. Microwave Theory Tech.*, vol. MTT-29, no. 11, pp. 1174–1181, 1981.
- [38] G. J. Simonis and K. G. Purchase, “Optical generation, distribution and control of microwaves using laser heterodyne,” *IEEE Trans. Microwave Theory Tech.*, vol. 38, no. 5, pp. 667–669, 1990.
- [39] E. R. Brown, F. W. Smith, and K. A. McIntosh, “Coherent millimeter-wave generation by heterodyne conversion in low-temperature-grown GaAs photoconductors,” *J. Appl. Phys.*, vol. 73, no. 3, pp. 1480–1484, 1993.
- [40] E. R. Brown, K. A. McIntosh, F. W. Smith, M. J. Manfra, and C. L. Dennis, “Measurements of optical-heterodyne conversion in low-temperature-grown GaAs,” *Appl. Phys. Lett.*, vol. 62, no. 11, pp. 1206–1208, 1993.
- [41] E. R. Brown, K. A. McIntosh, F. W. Smith, K. B. Nichols, M. J. Manfra, C. L. Dennis, and J. P. Mattia, “Milliwatt output levels and superquadratic bias dependence in a low-temperature-grown GaAs photomixer,” *Appl. Phys. Lett.*, vol. 64, no. 24, pp. 3311–3313, 1994.
- [42] E. R. Brown, K. A. McIntosh, K. B. Nichols, and C. L. Dennis, “Photomixing up to 3.8 THz in low-temperature-grown GaAs,” *Appl. Phys. Lett.*, vol. 66, no. 3, pp. 285–287, 1995.

- [43] K. A. McIntosh, E. R. Brown, K. B. Nichols, O. B. McMahon, W. F. Dinatale, and T. M. Lyszczarz, "Terahertz photomixing with diode lasers in low-temperature-grown GaAs," *Appl. Phys. Lett.*, vol. 67, no. 26, pp. 3844–3846, 1995.
- [44] S. Matsuura, M. Tani, and K. Sakai, "Generation of cw THz radiation by optical heterodyne with diode lasers and LTG-GaAs photoconductors," in *The Proceedings of International Topical Meeting on Microwave Photonics*, vol. 1, 1996, pp. 13–16.
- [45] S. Verghese, K. A. McIntosh, and E. R. Brown, "Highly tunable fiber-coupled photomixers with coherent terahertz output power," *IEEE Trans. Microwave Theory Tech.*, vol. 45, no. 8, pp. 1301–1309, 1997.
- [46] S. Verghese, K. A. McIntosh and E. R. Brown, "Optical and terahertz power limits in the low-temperature-grown GaAs photomixers," *Appl. Phys. Lett.*, vol. 71, no. 19, pp. 2743–2745, 1997.
- [47] S. Verghese, K. A. McIntosh, S. Calawa, W. F. Dinatale, E. K. Duerr, and K. A. Molvar, "Generation and detection of coherent terahertz waves using two photomixers," *Appl. Phys. Lett.*, vol. 73, no. 26, pp. 3824–3826, 1998.
- [48] S. Verghese, E. K. Duerr, K. A. McIntosh, S. M. Duffy, S. D. Calawa, C.-Y. E. Tong, R. Kimberk, and R. Blundell, "A Photomixer Local Oscillator for a 630-GHz Heterodyne Receiver," *IEEE Microwave and Guided Wave Lett.*, vol. 9, no. 6, pp. 245–247, 1999.
- [49] S. Matsuura, G. A. Blake, R. A. Wyss, J. C. Pearson, C. Kadow, A. W. Jackson, and A. C. Gossard, "A traveling-wave THz photomixer based on

- angle-tuned phase matching,” *Appl. Phys. Lett.*, vol. 74, no. 19, pp. 2872–2874, 1999.
- [50] P. Gu, F. Chang, M. Tani, K. Sakai, and C.-L. Pan, “Generation of Coherent cw-Terahertz Radiation Using a Tunable Dual-Wavelength External Cavity Laser Diode,” *Jpn. J. Appl. Phys.*, vol. 38, no. 11A, pp. L1246–L1248, 1999.
- [51] N. Zamdmer, *The Design and Testing of Integrated Circuits for Submillimeter-wave Spectroscopy*. Massachusetts Institute of Technology, 1999, ph.D. Thesis.
- [52] N. Zamdmer, Q. Hu, K. A. McIntosh, S. Verghese, and A. Forster, “On-chip frequency-domain submillimeter-wave transceiver,” *Appl. Phys. Lett.*, vol. 75, no. 24, pp. 3877–3879, 1999.
- [53] E. K. Duerr, K. A. McIntosh, S. M. Duffy, S. D. Calawa, S. Verghese, C.-Y. E. Tong, R. Kimberk, and R. Blundell, “Demonstration of a 630-GHz Photomixer Used as a Local Oscillator,” in *IEEE MTT-S Int. Microwave Symp. Dig.*, 1999, pp. 127–129.
- [54] A. Stohr, R. Heinzelmann, C. Kaczmarek, and D. Jager, “Ultra-broadband K_a to W-band 1.55 μm travelling-wave photomixer,” *Electron. Letts.*, vol. 36, no. 11, pp. 970–972, 2000.
- [55] M. Tani, P. Gu, M. Hyodo, K. Sakai, and T. Hidaka, “Generation of coherent terahertz radiation by photomixing of dual-mode lasers,” *Optical and Quantum Electronics*, vol. 32, pp. 503–520, 2000.
- [56] C. Kadow, A. W. Jackson, A. C. Gossard, S. Matsuura, and G. A. Blake, “Self-assembled ErAs islands in GaAs for optical-heterodyne terahertz generation,” *Appl. Phys. Lett.*, vol. 76, no. 24, pp. 3510–3512, 2000.

- [57] C. J. Stevens and D. J. Edwards, “High Temperature Superconducting MM-wave Photomixers,” in *Technical Digest. International Topical Meeting on Microwave Photonics*, Sept. 2000, pp. 237–240.
- [58] C. J. Stevens and D. J. Edwards, “Photomixing receiver using the kinetic inductive effect in high T_c superconductors,” *Electron. Letts.*, vol. 37, no. 23, pp. 1420–1421, 2001.
- [59] S. M. Duffy, S. Verghese, K. A. McIntosh, A. Jackson, C. Gossard, and S. Matsuura, “Accurate Modeling of Dual Dipole and Slot Elements Used with Photomixers for Coherent Terahertz Output Power,” *IEEE Trans. Microwave Theory Tech.*, vol. 49, no. 6, pp. 1032–1038, 2001.
- [60] E. Peytavit, G. Mouret, J. F. Lampin, S. Arscott, P. Masselin, L. Desplanque, O. Vanbesien, R. Bocquet, F. Mollot, and D. Lippens, “Terahertz electromagnetic generation via optical frequency difference,” *IEE Proc. Optoelectron.*, vol. 149, no. 3, pp. 82–87, 2002.
- [61] D. Pasqualini, A. Neto, and R. A. Wyss, “Distributed sources on coplanar waveguides: application to photomixers for THz local oscillators,” *Microw. Opt. Technol. Lett.*, vol. 33, no. 6, pp. 430–435, 2002.
- [62] E. R. Brown, “THz generation by photomixing in ultrafast photoconductors,” *International Journal of High Speed Electronics and Systems*, vol. 13, no. 2, pp. 497–545, 2003.
- [63] J. E. Bjarnason, T. L. J. Chan, A. W. M. Lee, E. R. Brown, D. C. Driscoll, M. Hanson, A. C. Gossard, and R. E. Muller, “ErAs:GaAs photomixer with two-decade tunability and 12 mW peak output power,” *Appl. Phys. Lett.*, vol. 85, no. 18, pp. 3983–3985, 2004.

- [64] M. Naftaly, M. R. Stone, A. Malcoci, R. E. Miles, and I. C. Mayorga, "Generation of CW terahertz radiation using two-colour laser with Fabry-Perot etalon," *Electron. Letts.*, vol. 41, no. 3, pp. 128–129, 2005.
- [65] I. S. Gregory, C. Baker, W. R. Tribe, I. V. Bradley, M. J. Evans, E. H. Linfield, A. G. Davies, and M. Missous, "Optimization of Photomixers and Antennas for Continuous-Wave Terahertz Emission," *IEEE J. Quantum Elec.*, vol. 41, no. 5, pp. 717–728, 2005.
- [66] G. Mouret, S. Matton, R. Bocquet, F. Hindle, E. Peytavit, J. F. Lampin, and D. Lippens, "Far-infrared cw difference-frequency generation using vertically integrated and planar low temperature grown GaAs photomixers: application to H_2S rotational spectrum up to 3 THz ," *Appl. Phys. B*, vol. 79, no. 6, pp. 725–729, 2004.
- [67] D. F. Plusquellic, T.M. Korter, G. T. Fraser, R. J. Lavrich, E. C. Benck, C. R. Bucher, A. R. Hight Walker, and J. L. Domenech, "Continuous-wave terahertz spectroscopy of plasmas and biomolecules," *International Journal of High Speed Electronics and Systems*, vol. 13, no. 4, pp. 1287–1306, 2003.
- [68] O. Morikawa, M. Fujita, and M. Hangyo, "Application of photomixing of multimode LD light on THz spectroscopy," in *Conference Digest. Twenty Seventh International Conference on Infrared and Millimeter Waves*, Sept. 2002, pp. 249–250.
- [69] A. S. Pine, R. D. Suenram, E. R. Brown, and K. A. McIntosh, "A Terahertz Photomixing Spectrometer: Application to SO_2 Self Broadening," *Journal of Molecular Spectroscopy*, vol. 175, pp. 37–43, 1996.

- [70] T. Löffler, K. J. Siebert, H. Quast, N. Hasegawa, G. Loata, R. Wipf, T. Hahn, M. Thomson, R. Leonhardt, and H. G. Roskos, “All-optoelectronic continuous-wave terahertz systems,” *Phil. Trans. R. Soc. Lond. A*, vol. 362, no. 1815, pp. 263–281, 2004.
- [71] K. J. Siebert, T. Löffler, H. Quast, M. Thomson, T. Bauer, R. Leonhardt, S. Czasch, and H. G. Roskos, “All-optoelectronic continuous wave THz imaging for biomedical applications,” *Phys. Med. Biol.*, vol. 47, no. 21, pp. 3743–3748, 2002.
- [72] J. E. Bjarnason, T. L. J. Chan, A. W. M. Lee, M. A. Celis, and E. R. Brown, “Millimeter-wave, terahertz, and mid-infrared transmission through common clothing,” *Appl. Phys. Lett.*, vol. 85, no. 4, pp. 519–521, 2004.
- [73] E. R. Brown, “A photoconductive model for superior GaAs THz photomixer,” *Appl. Phys. Lett.*, vol. 75, no. 6, pp. 769–771, 1999.
- [74] E. A. Michael, B. Vowinkel, R. Schieder, M. Mikulics, M. Marso, and P. Kordos, “Large-area traveling-wave photonic mixers for increased continuous terahertz power,” *Appl. Phys. Lett.*, vol. 86, no. 11, pp. 111 120–3, 2005.
- [75] R. Mendis, C. Sydlo, J. Sigmund, M. Feiginov, P. Meissner, and H. L. Hartnagel, “Tunable CW-THz system with a log-periodic photoconductive emitter,” *Solid-State Electron.*, vol. 48, no. 10-11, pp. 2041–2045, 2004.
- [76] I. S. Gregory, W. R. Tribe, B. E. Cole, M. J. Evans, E. H. Linfield, A. G. Davies, and M. Missous, “Resonant dipole antennas for continuous-wave terahertz photomixers,” *Appl. Phys. Lett.*, vol. 85, no. 9, pp. 1622–1624, 2004.
- [77] C. Sydlo, J. Sigmund, H. L. Hartnagel, G. Loata, K. J. Siebert, and H. G. Roskos, “Efficient THz-Emitters for Low-temperature-grown GaAs Pho-

- tomixers,” in *Proceedings of IEEE Tenth International Conference on Terahertz Electronics*, Sept. 2002, pp. 60–62.
- [78] A. W. Jackson, *Low-Temperatur-Grown GaAs Photomixers Designed for Increased Terahertz Output Power*. University of California Santa Barbara, 1999, ph.D. Thesis.
- [79] D. Saeedkia, S. Safavi-Naeini, and R. R. Mansour, “The intraction of laser and photoconductor in a continuous-wave terahertz photomixer,” *IEEE J. Quantum Elec.*, vol. 41, no. 9, pp. 1188–1196, September 2005.
- [80] D. Saeedkia, R. R. Mansour, and S. Safavi-Naeini, “Modeling and Analysis of High-Temperature Superconductor terahertz Photomixers,” *IEEE Trans. Appl. Superconduct.*, vol. 15, no. 3, September 2005.
- [81] D. Saeedkia, A. H. Majedi, S. Safavi-Naeini, and R. R. Mansour, “Analysis and design of a photoconductive integrated photomixer/antenna for terahertz applications,” *IEEE J. Quantum Elec.*, vol. 41, no. 2, pp. 234–241, February 2005.
- [82] —, “High-Temperature Superconductive Photomixer Patch Antenna: Theory and Design,” *IEICE Trans. Elecron.*, vol. E86-C, no. 7, pp. 1318–1327, July 2003.
- [83] D. Saeedkia, R. R. Mansour, and S. Safavi-Naeini, “Analysis of a Photoconductive Photomixer Array Source Designed for Terahertz Applications,” *IEEE Trans. Antennas Propagat.*, in press.
- [84] D. Saeedkia, A. H. Majedi, S. Safavi-Naeini, and R. R. Mansour, “CW Photoconductive Photomixer/Antenna Array Source for THz Applications,” in

- IEEE International Topical Meeting on Microwave Photonics*, October 2004, pp. 317–320.
- [85] D. Saeedkia, R. R. Mansour, and S. Safavi-Naeini, “A Sub-Milliwatt Terahertz High-Temperature Superconductive Photomixer Array Source: Analysis and Design,” *IEEE Trans. Appl. Superconduct.*, vol. 15, no. 3, September 2005.
- [86] K. Flech, B. G. Danly, H. R. Jory, K. E. Kreischer, W. Lawson, B. Levush, and R. J. Temkin, “Characteristics and Applications of Fast-Wave Gyrodevices,” *Proceedings of IEEE*, vol. 87, no. 5, pp. 752–781, 1999.
- [87] S. Krishnagopal and V. Kumar, “Free-electron lasers,” *Radiat. Phys. Chem.*, vol. 70, no. 4-5, pp. 559–569, 2004.
- [88] H. P. Freund and G. R. Neil, “Free-Electron Lasers: Vacuum Electronic Generators of Coherent Radiation,” *Proceedings of IEEE*, vol. 87, no. 5, pp. 782–803, 1999.
- [89] R. Kompfner and N. T. Williams, “Backward-wave tubes,” *Proc. IRE*, vol. 41, p. 1602, 1953.
- [90] K. Felch, M. Blank, P. Borchard, T. S. Chu, J. Feinstein, H. R. Jory, J. A. Lorbeck, C. M. Loring, Y. M. Mizuhara, J. M. Neilson, R. Schumacher, and R. J. Temkin, “Long pulse and CW tests of a 110 GHz gyrotron with an initial, quasioptical converter,” *IEEE Trans. Plasma Sci.*, vol. 24, no. 3, pp. 558–569, 1996.
- [91] G. Dammertz *et. al.*, “Development of a 140-GHz 1-MW Continuous Wave Gyrotron for the W7-X Stellarator,” *IEEE Trans. Plasma Sci.*, vol. 30, no. 3, pp. 808–818, 2002.

- [92] B. Piosczyk, G. Dammertz, O. Dumbrajs, O. Drumm, S. Illy, J. Jin, and M. Thumm, “A 2-MW, 170-GHz Coaxial Cavity Gyrotron,” *IEEE Trans. Plasma Sci.*, vol. 32, no. 3, pp. 413–417, 2004.
- [93] L. Granatstein, R. K. Parker, and C. M. Armstrong , “Vacuum Electronics at the Dawn of the Twenty-First Century,” *Proceedings of IEEE*, vol. 87, no. 5, pp. 702–716, 1999.
- [94] H. P. Freund and T. J. Antonsen, *Principles of Free-Electron Lasers*, 2nd ed. London, U.K.: Chapman & Hall, 1996.
- [95] G. P. Williams, “FAR-IR/THz radiation from the Jefferson Laboratory, energy recovered linac, free electron laser,” *Rev. Sci. Instrum.*, vol. 73, no. 3, pp. 1461–1463, 2002.
- [96] G. R. Neil and G. P. Williams, “Evolution of the high power THz source program at Jefferson Lab,” *Infrared Phys. Technol.*, vol. 43, no. 5-6, pp. 389–391, 2004.
- [97] M. Billardon, P. Elleaume, J. M. Ortega, C. Bazin, M. Bergher, M. Velghe, Y. Petroff, D. A. G. Deacon, K. E. Robinson, and J. M. J. Madey, “First Operation of a Storage-Ring Free-Electron Laser,” *Phys. Rev. Lett.*, vol. 51, no. 18, pp. 1652–1655, 1983.
- [98] C. Pellegrini and S. Reiche, “The Development of X-Ray Free-Electron Lasers,” *IEEE J. Sel. Top. Quantum Electron.*, vol. 10, no. 6, pp. 1393–1404, 2004.
- [99] L. P. Schmidt, S. Biber, G. Rehm, and K. Huber, “THz Measurement Technologies and Applications,” *14th International Conference on Microwaves, Radar and Wireless Communications*, vol. 2, pp. 581–587, 2002.

- [100] R. L. Ives, D. Marsden, M. Caplan, C. Kory, J. Neilson, and S. Schwartzkopf, “Advanced terahertz backward wave oscillators,” in *4th IEEE International Conference on Vacuum Electronics*, May 2003, pp. 20–21.
- [101] R. L. Ives, “Microfabrication of High-Frequency Vacuum Electron Devices,” *IEEE Trans. Plasma Sci.*, vol. 32, no. 3, pp. 1277–1291, 2004.
- [102] T. Y. Chang and T. J. Bridges, “Laser action at 452, 496, and 541 μm in optically pumped CH_3F ,” *Opt. Commun.*, vol. 1, p. 423, 1970.
- [103] M. Inguscio, G. Moruzzi, K. M. Evenson, and D. A. Jennings, “A review of frequency measurements of optically pumped lasers from 0.1 to 8 THz,” *J. Appl. Phys.*, vol. 60, no. 12, pp. R161–R192, 1986.
- [104] D. D. Bicanic, B. F. J. Zuidberg, and A. Dymanus, “Generation of continuously tunable laser sidebands in the submillimeter region,” *Appl. Phys. Lett.*, vol. 32, no. 6, pp. 367–369, 1978.
- [105] G. A. Blake, K. B. Laughlin, R. C. Cohen, K. L. Busarow, D-H. Gwo, C. A. Schmuttenmaer, D. W. Steyert, and R. J. Saykally, “Tunable far infrared laser spectrometers,” *Rev. Sci. Instrum.*, vol. 62, no. 7, pp. 1693–1700, 1991.
- [106] M. C. Gaidis, H. M. Pickett, C. D. Smith, S. C. Martin, P. R. Smith, and P. H. Siegel, “A review of frequency measurements of optically pumped lasers from 0.1 to 8 THz,” *J. Appl. Phys.*, vol. 60, no. 12, pp. R161–R192, 1986.
- [107] G. I. Haddad and R. J. Trew, “Microwave Solid-State Active Devices,” *IEEE Trans. Microwave Theory Tech.*, vol. 50, no. 3, pp. 760–779, 2002.
- [108] H. Eisele, A. Rydberg, and G. I. Haddad, “Recent Advances in the Performance of InP Gunn Devices and GaAs TUNNETT Diodes for the 100-300-

- GHz Frequency Range and Above,” *IEEE Trans. Microwave Theory Tech.*, vol. 48, no. 4, pp. 626–631, 2000.
- [109] H. Eisele and G. I. Haddad, “Two-Terminal Millimeter-Wave Sources,” *IEEE Trans. Microwave Theory Tech.*, vol. 46, no. 6, pp. 739–746, 1998.
- [110] E. R. Brown and C. D. Parker, “Resonant tunnel diodes as submillimetre-wave sources,” *Phil. Trans. R. Soc. Lond. A*, vol. 354, pp. 2365–2381, 1996.
- [111] H. Eisele and R. Kamoua, “Submillimeter-Wave InP Gunn Devices,” *IEEE Trans. Microwave Theory Tech.*, vol. 52, no. 10, pp. 2371–2378, 2004.
- [112] L. Wandinger, “mm-Wave InP Gunn devices: Status and trends,” *Microwave J.*, vol. 24, no. 3, pp. 71–78, 1981.
- [113] H. Eisele and G. I. Haddad, “High-performance InP Gunn devices for fundamental-mode operation in D-band (110-170 GHz),” *IEEE Microwave and Guided Wave Lett.*, vol. 5, pp. 385–387, 1995.
- [114] M. Asada, “Optoelectronic devices for terahertz amplification and oscillation,” in *The 17th Annual Meeting of the IEEE Lasers and Electro-Optics Society*, vol. 2, November 2004, pp. 671–672.
- [115] E. R. Brown, J. R. Soderstrom, C. D. Parker, L. J. Mahoney, K. M. Molvar, and T. C. McGill, “Oscillations up to 712 GHz in InAs/AlSb resonant tunneling diodes,” *Appl. Phys. Lett.*, vol. 58, pp. 2291–2293, 1991.
- [116] M. Dragoman and D. Dragoman, “Carbon nanotube resonant-tunneling diodes,” *Physica E*, vol. 24, no. 3-4, pp. 282–289, 2004.
- [117] H. Eisele, M. Naftaly, and R. Kamoua, “Generation of submillimeter-wave radiation with GaAs TUNNETT diodes and InP Gunn devices in a second

- or higher harmonic mode,” *Int. J. Infrared Millim. Waves*, vol. 26, no. 1, pp. 1–14, 2005.
- [118] E. R. Brown, C. D. Parker, A. R. Calawa, M. J. Manfra, and K. M. Molvar, “A quasioptical resonant-tunneling-diode oscillator operating above 200 GHz,” *IEEE Trans. Microwave Theory Tech.*, vol. 41, no. 4, pp. 720–722, 1993.
- [119] H. Eisele, “Second-harmonic power extraction from InP Gunn devices with more than 1 mW in the 260-320 GHz frequency range,” *Electron. Letts.*, vol. 34, no. 25, pp. 2412–2413, 1998.
- [120] M. Wollitzer, J. Buechler, F. Schaffler, and J.-F. Luy, “D-band Si-IMPATT diodes with 300 mW output power at 140 GHz,” *Electron. Letts.*, vol. 32, no. 2, pp. 122–123, 1996.
- [121] M. Ino, T. Ishibashi, and M. Ohmori, “C.W. Oscillation with $p^+ - p - n^+$ Silicon IMPATT Diodes in 200 GHz and 300 GHz,” *Electron. Letts.*, vol. 12, no. 6, pp. 148–149, 1976.
- [122] H. Eisele, “355 GHz oscillator with GaAs TUNNETT diode,” *Electron. Letts.*, vol. 41, no. 6, pp. 55–56, 2005.
- [123] K. Shinohara, Y. Yamashita, A. Endoh, I. Watanabe, K. Hikosaka, T. Matsui, T. Mimura, and S. Hiyamizu, “547-GHz f_t $\text{In}_{0.7}\text{Ga}_{0.3}\text{As} - \text{In}_{0.52}\text{Al}_{0.48}\text{As}$ HEMTs With Reduced Source and Drain Resistance,” *IEEE Electron Device Lett.*, vol. 25, no. 5, pp. 241–243, 2004.
- [124] L. Samoska, A. Peralta, M. Hu, M. Micovic, and A. Schmitz, “A 20 mW, 150 GHz InP HEMT MMIC Power Amplifier Module,” *IEEE Microwave Wireless Comp. Lett.*, vol. 14, no. 2, pp. 56–58, 2004.

- [125] A. Tessmann, A. Leuther, H. Massler, M. Kurl, C. Schwoerer, M. Schlechtweg, and G. Weimann, "A 220 GHz metamorphic HEMT amplifier MMIC," in *IEEE Compound Semiconductor Integrated Circuit Symposium Digest*, 2004, pp. 297–300.
- [126] L. A. Samoska, T. C. Gaier, A. Peralta, S. Weibreb, J. Bruston, I. Mehdi, Y. Chen, H. H. Liao, M. Nishimoto, R. Lai, H. Wang, and Y. C. Leong, "MMIC power amplifiers as local oscillator drivers for FIRST," in *The Proceedings of SPIE Conference*, vol. 4013, August 2000, pp. 275–284.
- [127] J. Ward, G. Chattopadhyay, A. Maestrini, E. Schlecht, J. Gill, H. Javadi, D. Pukala, F. Maiwald, and I. Mehdi, "Tunable All-Solid-State Local Oscillators to 1900 GHz," in *Fifteenth International Symposium on Space Terahertz Technology*, Amherst, Massachusetts, 2004.
- [128] A. Maestrini, J. Ward, J. Gill, H. Javadi, E. Schlecht, G. Chattopadhyay, F. Maiwald, N. R. Erickson, and I. Mehdi, "A 1.7-1.9 THz Local Oscillator Source," *IEEE Microwave Wireless Comp. Lett.*, vol. 14, no. 6, pp. 253–255, 2004.
- [129] G. Chattopadhyay, E. Schlecht, J. S. Ward, J. J. Gill, Hh H. S. Javadi, F. Maiwald, and I. Mehdi, "An All-Solid-State Broad-Band Frequency Multiplier Chain at 1500 GHz," *IEEE Trans. Microwave Theory Tech.*, vol. 52, no. 5, pp. 1538–1546, 2004.
- [130] A. Maestrini, J. Bruston, D. Pukala, S. Martin, and I. Mehdi, "Performance of a 1.2 THz frequency tripler using a GaAs frameless membrane monolithic circuit," *IEEE MTT-S Int. Microwave Symp. Dig.*, vol. 3, pp. 1657–1660, 2001.

- [131] P. H. Siegel, “Terahertz Technology,” *IEEE Trans. Microwave Theory Tech.*, vol. 50, no. 3, pp. 910–928, 2002.
- [132] J. Ward, E. Schlecht, G. Chattopadhyay, A. Maestrini, J. Gill, F. Maiwald, H. Javadi, and I. Mehdi, “Capability of THz sources based on Schottky diode frequency multiplier chains,” in *IEEE MTT-S Int. Microwave Symp. Dig.*, vol. 3, 2004, pp. 1587–1590.
- [133] V. Krozer, G. Loata, J. Grajal de la Fuente, and P. Sanz, “Limitations in THz power generation with Schottky diode varactor frequency multipliers,” in *Proceedings of IEEE Tenth International Conference on Terahertz Electronics*, Sept. 2002, pp. 109–112.
- [134] J. N. Hovenier, M. C. Diez, T. O. Klaassen, W. T. Wenckebach, A. V. Muravjov, S. G. Pavlov, and V. N. Shastin, “The p-Ge Terahertz Laser Properties Under Pulsed and Mode-Locked Operation,” *IEEE Trans. Microwave Theory Tech.*, vol. 48, no. 4, pp. 670–676, 2000.
- [135] R. Kazarionov and R. A. Suris, “Possibility of the amplification of electromagnetic waves in a semiconductor with a superlattice,” *Sov Phys Semicond.*, vol. 5, no. 4, pp. 707–709, 1971.
- [136] J. Faist, F. Capasso, D. L. Sivco, C. Sirtori, A. L. Hutchinson, and A. Y. Cho, “Quantum cascade laser,” *Science*, vol. 264, no. 5158, pp. 553–556, 1994.
- [137] F. Capasso, J. Faist, C. Sirtori, D. L. Sivco, J. N. Baillargeon, A. L. Hutchinson, and A. Y. Cho, “Quantum cascade lasers: new resonant tunnelling light sources for the mid-infrared,” *Phil. Trans. R. Soc. Lond. A*, vol. 354, pp. 2463–2467, 1996.

- [138] F. Capasso *et. al.*, “Quantum Cascade Lasers: Ultrahigh-Speed Operation, Optical Wireless Communication, Narrow Linewidth, and Far-Infrared Emission,” *IEEE J. Quantum Elec.*, vol. 38, no. 6, pp. 511–532, 2002.
- [139] J. Faist, D. Hofstetter, M. Beck, T. Aellen, M. Rochat, and S. Blaser, “Quantum Cascade Lasers: Ultrahigh-Speed Operation, Optical Wireless Communication, Narrow Linewidth, and Far-Infrared Emission,” *IEEE J. Quantum Elec.*, vol. 38, no. 6, pp. 533–546, 2002.
- [140] R. Kohler, A. Tredicucci, F. Beltram, H. E. Beere, E. H. Linfield, A. G. Davies, D. A. Ritchie, R. C. Iotti, and F. Rossi, “Terahertz semiconductor-heterostructure laser,” *Nature*, vol. 417, no. 6885, pp. 156–159, May 2002.
- [141] S. Slivken, Z. Huang, A. Evans, and M. Razeghi, “High-power ($\lambda = 9 \mu\text{m}$) quantum cascade lasers,” *Appl. Phys. Lett.*, vol. 80, no. 22, pp. 4091–4093, 2002.
- [142] S. Barbieri, J. Alton, S. S. Dhillon, H. E. Beere, M. Evans, E. H. Linfield, A. G. Davies, D. A. Ritchie, R. Kohler, A. Tredicucci, and F. Beltram, “Continuous-Wave Operation of Terahertz Quantum-Cascade Lasers,” *IEEE J. Quantum Elec.*, vol. 39, no. 4, pp. 586–591, 2003.
- [143] J. S. Yu, A. Evans, S. Slivken, S. R. Darvish, and M. Razeghi, “Short Wavelength ($\lambda = 4.3 \mu\text{m}$) High-Performance Continuous-Wave Quantum-Cascade Lasers,” *IEEE Photonics Technol. Lett.*, vol. 17, no. 6, pp. 1154–1156, 2005.
- [144] W. W. Bewley, J. R. Lindle, C. Soo Kim, I. Vurgaftman, J. R. Meyer, A. J. Evans, J. Su Yu, S. Slivken, and M. Razeghi, “Beam Steering in High-Power CW Quantum-Cascade Lasers,” *IEEE J. Quantum Elec.*, vol. 41, no. 6, pp. 833–841, 2005.

- [145] A. Evans, J. S. Yu, J. David, L. Doris, K. Mi, S. Slivken, and M. Razeghi, “High-temperature, high-power, continuous-wave operation of buried heterostructure quantum-cascade lasers,” *Appl. Phys. Lett.*, vol. 84, no. 3, pp. 314–316, 2004.
- [146] M. Beck, D. Hofstetter, T. Aellen, J. Faist, U. Oesterle, M. Ilegems, E. Gini, and H. Melchior, “Continuous Wave Operation of a Mid-Infrared Semiconductor Laser at Room Temperature,” *Science*, vol. 1295, no. 5553, pp. 301–305, 2002.
- [147] R. Kohler, A. Tredicucci, F. Beltram, H. E. Beere, E. H. Linfield, A. G. Davies, D. A. Ritchie, S. S. Dhillon, and C. Sirtori, “High-performance continuous-wave operation of superlattice terahertz quantum-cascade lasers,” *Appl. Phys. Lett.*, vol. 82, no. 10, pp. 1518–1520, 2003.
- [148] S. Kumar, B. S. Williams, S. Kohen, Q. Hu, and J. L. Reno, “Continuous-wave operation of terahertz quantum-cascade lasers above liquid-nitrogen temperature,” *Appl. Phys. Lett.*, vol. 84, no. 14, pp. 2494–2496, 2004.
- [149] J. Nishizawa, *Denshi Kagaku*, vol. 13, p. 17, 1963, in Japanese.
- [150] J. Nishizawa and K. Suto, “Semiconductor Raman Laser,” *J. Appl. Phys.*, vol. 51, no. 5, pp. 2429–2431, 1980.
- [151] K. Kawase, J. Shikata, and H. Ito, “Terahertz wave parametric source,” *J. Phys. D: Appl. Phys.*, vol. 34, no. 6, pp. R1–R14, 2002.
- [152] J. Shikata, K. Kawase, K. Karino, T. Taniuchi, and H. Ito, “Tunable Terahertz-Wave Parametric Oscillators Using LiNbO_3 and $\text{MgO} : \text{LiNbO}_3$ Crystals,” *IEEE Trans. Microwave Theory Tech.*, vol. 48, no. 4, pp. 653–661, 2000.

- [153] Y. J. Ding and W. Shi, “Widely-Tunable, Monochromatic, and High-Power Terahertz Sources and Their Applications,” *J. Nonlinear Opt. Phys. Mater.*, vol. 12, no. 4, pp. 557–585, 2003.
- [154] T. Tanabe, K. Suto, J. Nishizawa, and T. Sasaki, “Characteristics of terahertz-wave generation from GaSe crystals,” *J. Phys. D: Appl. Phys.*, vol. 37, no. 2, pp. 155–158, 2004.
- [155] T. Tanabe, K. Suto, J. Nishizawa, T. Kimura, and K. Saito, “Frequency-tunable high-power terahertz wave generation from GaP,” *J. Appl. Phys.*, vol. 93, no. 8, pp. 4610–4615, 2003.
- [156] T. Taniuchi and H. Nakanishi, “Collinear phase-matched terahertz-wave generation in GaP crystal using a dual-wavelength optical parametric oscillator,” *J. Appl. Phys.*, vol. 95, no. 12, pp. 7588–7591, 2004.
- [157] K. Kawase, T. Hatanaka, H. Takahashi, K. Nakamura, and T. Taniuchi, “Tunable terahertz-wave generation from DAST crystal by dual signal-wave parametric oscillation of periodically poled lithium niobate,” *Opt. Lett.*, vol. 25, no. 23, pp. 1714–1716, 2000.
- [158] H. Adachi, T. Taniuchi, M. Yoshimura, S. Brahadeeswaran, T. Higo, M. Takagi, Y. Mori, T. Sasaki, and H. Nakanishi, “High-Quality Organic 4-Dimethylamino-N-methyl-4-stilbazolium Tosylate (DAST) Crystals for THz Wave Generation,” *Jpn. J. Appl. Phys.*, vol. 43, no. 8B, pp. L1121–L1123, 2004.
- [159] T. Taniuchi, S. Okada, and H. Nakanishi, “Widely tunable terahertz-wave generation in an organic crystal and its spectroscopic application,” *J. Appl. Phys.*, vol. 95, no. 11, pp. 5984–5988, 2004.

- [160] S. Wu, V. A. Kapinus, and G. A. Blake, “A nanosecond optical parametric generator/amplifier seeded by an external cavity diode laser,” *Opt. Commun.*, vol. 159, no. 1-3, pp. 74–79, 1999.
- [161] W. Shi and Y. J. Ding, “A monochromatic and high-power terahertz source tunable in the ranges of 2.738.4 and 58.23540 μm for variety of potential applications,” *Appl. Phys. Lett.*, vol. 84, no. 10, pp. 1635–1637, 2004.
- [162] —, “Tunable terahertz waves generated by mixing two copropagating infrared beams in GaP,” *Opt. Lett.*, vol. 30, no. 9, pp. 1030–1032, 2005.
- [163] T. Tanabe, K. Suto, J. Nishizawa, K. Saito, and T. Kimura, “Tunable terahertz wave generation in the 3- to 7-THz region from GaP,” *Appl. Phys. Lett.*, vol. 83, no. 2, pp. 237–239, 2003.
- [164] M. Suzuki and M. Tonouchi, “Fe-implanted InGaAs terahertz emitters for 1.56 μm wavelength excitation,” *Appl. Phys. Lett.*, vol. 86, no. 5, pp. 051 104–3, 2005.
- [165] M. P. Hanson, D. C. Driscoll, J. D. Zimmerman, A. C. Gossard, and E. R. Brown, “Subpicosecond photocarrier lifetimes in GaSb/ErSb nanoparticle superlattices 1t 1.55 μm ,” *Appl. Phys. Lett.*, vol. 85, no. 15, pp. 3110–3112, 2004.
- [166] M. Griebel, J. H. Smet, D. C. Driscoll, J. Kuhl, C. Alvarez Diez, N. Freytag, C. Kadow, A. C. Gossard, and K. Von Klitzing, “Tunable subpicosecond optoelectronic transduction in superlattices of selfassembled ErAs nanoislands,” *Nat. Mater.*, vol. 2, no. 2, pp. 122–126, 2003.

- [167] M. Sukhotin, E. R. Brown, D. Driscoll, M. Hanson, and A. C. Gossard, “Picosecond photocarrier-lifetime in ErAs:InGaAs at 1.55 μm ,” *Appl. Phys. Lett.*, vol. 83, no. 19, pp. 3921–3923, 2003.
- [168] C. Carmody, H. H. Tan, C. Jagadish, A. Gaarder, and S. Marcinkevicius, “Ion-implanted $\text{In}_{0.53}\text{Ga}_{0.47}\text{As}$ for ultrafast optoelectronic applications,” *Appl. Phys. Lett.*, vol. 82, no. 22, pp. 3913–3915, 2003.
- [169] S. Gupta, J. F. Whitaker, and G. A. Mourou, “Ultrafast Carrier Dynamics in 111-V Semiconductors Grown by Molecular-Beam Epitaxy at Very Low Substrate Temperatures,” *IEEE J. Quantum Elec.*, vol. 28, no. 10, pp. 2464–2472, 1992.
- [170] N. Perrin and C. Vanneste, “Response of superconducting films to a periodic optical irradiation,” *Phys. Rev. B*, vol. 28, no. 9, pp. 5150–5159, 1983.
- [171] A. Frenkel, “Mechanisms of nonequilibrium optical response of high temperature superconductors,” *Phys. Rev. B*, vol. 48, no. 13, pp. 9717–9725, 1993.
- [172] A. D. Semenov, R. S. Nebosis, Y. P. Gousev, M. A. Heusinger, and K. F. Renk, “Analysis of the nonequilibrium photoresponse of superconducting films to pulsed radiation by use of a two-temperature model,” *Phys. Rev. B*, vol. 52, no. 1, pp. 581–590, 1995.
- [173] A. H. Majedi, D. Saeedkia, S. K. Chaudhuri, and S. Safavi-Naeini, “Physical Modeling and Frequency Response Analysis of a High-Temperature Superconducting THz Photomixer,” *IEEE Trans. Microwave Theory Tech.*, vol. 52, no. 10, pp. 2430–2437, October 2004.

- [174] F. Gao, J. W. Kruse, C. E. Platt, M. Feng, and M. V. Klein, “Microwave surface impedance at 10 GHz and quasiparticle scattering in $YBa_2Cu_3O_7$ films,” *Appl. Phys. Lett.*, vol. 63, pp. 2274–2276, October 1993.
- [175] O. G. Vendik, I. B. Vendik, and D. I. Kaparkov, “Empirical Model of the Microwave Properties of High-Temperature Superconductors,” *IEEE Trans. Microwave Theory Tech.*, vol. 46, no. 5, pp. 469–478, 1998.
- [176] T. P. Orlando and K. A. Delin, *Foundation of Applied Superconductivity*. Addison-Wesley Publishing Company, 1990.
- [177] F. A. Hegmann and J. S. Preston, “Origin of the fast photoresponse of epitaxial $YBa_2Cu_3O_{7-\delta}$ thin films,” *Appl. Phys. Lett.*, vol. 48, no. 21, pp. 16 023–16 039, 1993.
- [178] H. Yasuoka, H. Mazaki, T. Terashima, and Y. Bando, “Optical absorption spectra of single-crystal $YBa_2Cu_3O_y$ films,” *Physica C*, vol. 175, no. 1-2, pp. 192–196, 1991.
- [179] C. D. Marshall, I. M. Fishman, R. C. Dorfman, C. B. Eom, and M. D. Fayer, “Thermal diffusion, interfacial thermal barrier, and ultrasonic propagation in $YBa_2Cu_3O_{7-x}$ thin films Surface-selective transient-grating experiments,” *Phys. Rev. B*, vol. 45, no. 17, pp. 10 009–10 021, 1992.
- [180] N. Gedik, J. Orenstein, R. Liang, D. A. Bonn, and W. N. Hardy, “Diffusion of Nonequilibrium Quasi-Particles in a Cuprate Superconductor,” *Science*, vol. 300, no. 5624, pp. 1410–1412, 30 May 2003.
- [181] F. A. Hegmann, *Picosecond Photoresponse of High-Temperature Superconductor Thin Films*. McMaster University, 1994, ph.D. Thesis.

- [182] S. Gupta, M. Y. Frankel, J. A. Valdmanis, J. F. Whitaker, G. A. Mourou, F. W. Smith, and A. R. Calawa, “Subpicosecond carrier lifetime in GaAs grown by molecular beam epitaxy at low temperatures,” *Appl. Phys. Lett.*, vol. 59, no. 25, pp. 3276–3278, 1991.
- [183] E. S. Harmon, M. R. Melloch, J. M. Woodall, D. D. Nolte, N. Otsuka, and C. L. Chang, “Carrier lifetime versus anneal in low temperature growth GaAs,” *Appl. Phys. Lett.*, vol. 63, no. 16, pp. 2248–2250, 1993.
- [184] D. H. Auston, “Picosecond optoelectronic switching and gating in silicon,” *Appl. Phys. Lett.*, vol. 26, no. 3, pp. 101–103, 1975.
- [185] R. Yano, Y. Hirayama, S. Miyashita, N. Uesugi, and S. Uehara, “Arsenic pressure dependence of carrier lifetime and annealing dynamics for low-temperature grown GaAs studied by pump-probe spectroscopy,” *J. Appl. Phys.*, vol. 94, no. 6, pp. 3966–3971, 2003.
- [186] M. Stellmacher, J. Nagle, J. F. Lampin, P. Santoro, J. Vaneeckloo, and A. Alexandrou, “Dependence of the carrier lifetime on acceptor concentration in GaAs grown at low-temperature under different growth and annealing conditions,” *J. Appl. Phys.*, vol. 88, no. 10, pp. 6026–6031, 2000.
- [187] K. A. McIntosh, K. B. Nichols, S. Verghese, and E. R. Brown, “Investigation of ultrashort photocarrier relaxation times in low-temperature-grown GaAs,” *Appl. Phys. Lett.*, vol. 70, no. 3, pp. 354–356, 1997.
- [188] I. S. Gregory, C. Baker, W. R. Tribe, M. J. Evans, H. E. Beere, E. H. Linfield, A. G. Davies, and M. Missous, “High resistivity annealed low-temperature GaAs with 100 fs lifetimes,” *Appl. Phys. Lett.*, vol. 83, no. 20, pp. 4199–4201, 2003.

- [189] P. A. Loukakos, C. Kalpouzos, I. E. Perakis, Z. Hatzopoulos, M. Logaki, and C. Fotakis, “Ultrafast electron trapping times in low-temperature-grown gallium arsenide: The effect of the arsenic precipitate spacing and size,” *Appl. Phys. Lett.*, vol. 79, no. 18, pp. 2883–2885, 2001.
- [190] S. M. Sze, *Physics of Semiconductor Devices*. John Wiley and Sons, 1981, pp. 50-51.
- [191] M. S. Demokan, “The interaction of mode-locked laser pulses with intrinsic silicon,” *Int. J. Electronics*, vol. 51, no. 2, pp. 93–143, 1981.
- [192] R. A. Smith, *Semiconductors*, 2nd ed. Cambridge University Press, 1978.
- [193] J. G. Ruch and G. S. Kino, “Transport properties of GaAs,” *Physical Review*, vol. 174, no. 3, pp. 921–931, 1968.
- [194] C. Jacoboni, C. Canali, G. Ottaviani, and A. Alberigi Quaranta, “A review of some charge transport properties of silicon,” *Solid-State Electronics*, vol. 20, no. 2, pp. 77–89, 1977.
- [195] E. E. Godik, Y. A. Kuritsyn, and V. P. Sinis, “Effect of an electric field on carrier capture by attractive centers,” *Fizika i Tekhnika Poluprovodnikov*, vol. 12, no. 2, pp. 351–357, 1978.
- [196] T. H. Ning, “High-field capture of electrons by columb-attractive centers in silicon dioxide,” *J. Appl. Phys.*, vol. 47, no. 7, pp. 3203–3208, 1976.
- [197] V. Y. Prints and B. A. Bobylev, “Influence of a strong electric field on the electron capture by nonradiative GaAs centers,” *Fizika i Tekhnika Poluprovodnikov*, vol. 14, no. 9, pp. 1839–1841, 1980.

- [198] H. W. Thim, “Computer study of bulk GaAs Devices with random one-dimensional doping fluctuations,” *J. Appl. Phys.*, vol. 39, no. 8, pp. 3897–3904, 1968.
- [199] C.-K. Sun, Y.-H. Chen, J.-W. Shi, Y.-J. Chiu, K.-G. Gan, and J. E. Bowers, “Electron relaxation and transport dynamics in low-temperature-grown GaAs under 1 eV optical excitation,” *Appl. Phys. Lett.*, vol. 83, no. 5, pp. 911–913, 2003.
- [200] N. Zamdmer, Q. Hu, K. A. McIntosh, and S. Verghese, “Increase in response time of low-temperature-grown GaAs photoconductive switches at high voltage bias,” *Appl. Phys. Lett.*, vol. 75, no. 15, pp. 2313–2315, 1999.
- [201] Y. M. Li, “Phototransport under the presence of a small steady-state photocarrier grating,” *Phys. Rev. B*, vol. 42, no. 14, pp. 9025–9032, 1990.
- [202] D. E. Aspnes, “Recombination at semiconductor surfaces and interfaces,” *Surface Science*, vol. 132, no. 1-3, pp. 406–421, 1983.
- [203] D. R. Jackson and N. G. Alexopoulos, “Gain Enhancement Methods for Printed Circuit Antennas,” *IEEE Trans. Antennas Propagat.*, vol. AP-33, no. 9, pp. 976–987, 1985.
- [204] D. R. Jackson and J. T. Williams, “A Comparison of CAD Models for Radiation from Rectangular Microstrip Patches,” *Int. J. Microwave Millimeter-Wave Comp. Aided Eng.*, vol. 1, no. 2, pp. 236–248, 1991.
- [205] C. A. Balanis, *Antenna theory: analysis and design*. John Wiley and Sons, 1997.

- [206] ———, *Advanced Engineering Electromagnetics*. John Wiley and Sons, 1989, chapter 8.
- [207] D. P. Norton, “Epitaxial Growth of Superconducting Cuprate Thin Films,” *in Handbook of High-Temperature Superconductor Electronics*, Ed. by N. Khare (Marcel Dekker Inc., 2003), Chapter 2.
- [208] T. Tamir, Ed., *Guided-Wave Optoelectronics*, 2nd ed. Springer-Verlag, 1990, page 321.
- [209] K. Okamoto, *Fundamentals of Optical Waveguides*. Academic Press, 2000.